1.0 Cover Page

ALPHA FOUNDATION FOR THE IMPROVEMENT OF MINE SAFETY AND HEALTH

Final Technical Report

Recipient Organization: Pennsylvania State University

DUNS Number: 00-340-3953

Recipient Address: 224 Hosler, University Park, PA 16802

Contract Number: Grant #: AFC719-27

Project Title: Control of Hazardous Gas Emissions to Longwall Face and Bleeder System: Laboratory Experiments, Modeling and Field Monitoring

Principal Investigator(s): Shimin Liu, Assistant Professor (PI, PSU)
szl3@psu.edu
+1.814.863.4491

Derek Elsworth (Co-PI, PSU)
elsworth@psu.edu
+1.814.865.2225

Satya Harpalani (Co-PI, SIUC)
satya@engr.siu.edu
+1.618.453.7918

Contact Information: Phone: 814-863-4491
Fax : 814-865-3248
E-mail : szl3@psu.edu

Period of Performance: July 1, 2018 to December 31, 2020

Contents

List of Figures

List of Tables

2.0 Executive Summary

A total of forty-three US underground coal mining operations use the longwall method for coal extraction, contributing approximately half of total underground coal production. Although the longwall method offers distinct advantages of higher productivity and improved safety, it results in methane emissions that are typically higher than room-and-pillar recovery on a per-ton-of-coal-mined basis. Thus, longwall mining presents a unique hazard in mining in providing both a low-impedance network for methane transport around the active mine workings and supplying this from a substantial, albeit high-impedance, methane reservoir of the evolving gob – a doubly hazardous outcome. Characterization of gas emission from the gob is one of the most challenging tasks due to its dynamic evolution, intrinsic heterogeneity and resulting complexity of gas flow behavior.

Fatal lessons learned from UBB demonstrate the need for an improved understanding of gas transmission from the gob to the shield canopy, together with knowledge of how the methane accumulates within this confined space. The ongoing challenges of characterizing gob gas emission are significant, and underscore the need for a systematic strategy for quantifying and modeling gob gas storage, emission and transport behaviors. The overarching goal of this project is to develop appropriate strategies to characterize and model methane emission and transmission from the gob to the mine ventilation system and to effectively mitigate impacts of elevated methane concentrations for longwall mines.

This work synthesizes laboratory experiments, analysis, CFD modeling and in-mine measurements to quantify gas emission behavior in longwall mines and to address four specific issues. The first explores rock compaction in the gob and quantifies gas generation and transport response; the second quantifies dynamic permeability evolution around the gob perimeter, modulated by rock compaction and evolving *in situ* stress; the third develops a CFD model to define the airflow dynamics in the gob and its interaction with the ventilation system; and the fourth constrains these prior models using field measurements recovered from a longwall mine to quantity gas emission directly from the gob to the mine ventilation system.

The main outcomes of this study are summarized in Section 7 and include: (1) development of an analytical pressure gradient model to evaluate gob gas emissions and their interaction with the ventilation system; (2) recognition and quantification of heterogeneous compaction around the longwall gob perimeter through observation, experiment and modeling; (3) projection of the impacts of heterogeneous compaction on elevated gas emission and transport towards the face; and (4) validation against field monitoring data identifying that steady-state methane concentrations increase monotonically and almost linearly from headgate to tailgate.

Key remaining uncertainties and knowledge gaps are noted in Section 8 and relate to (i) defining the heterogeneity of the gob collapse and direct scaled-measurement of permeability

and desorption characteristics of the rate-limiting methane supply from the gob; (ii) constraining the geometry, particle size distribution (PSD), and permeability characteristics of the gob-skirting high-permeability perimeter through imaging and reconstruction, and in (iii) defining the impacts of these features ((i) and (ii)) on system performance and face gas loading through informed CFD-modeling including the (iv) impact of various gob-drainage and other mitigation methods. These combined studies are most feasibly delivered through an in-mine demonstration project and would provide comprehensive tools to improve the safety and effectiveness of longwall mining in the US.

This project focuses on underground longwall coal mines with the resulting outcomes primarily intended for underground longwall operators. Nevertheless, the principal results are also applicable to retreat mining for room and pillar mines and gassy trona longwalls.

3.0 Problem Statement and Objectives

Focus area: Health and Safety Interventions

Topic Areas: Monitoring Systems and Integrated Control Technologies

Specific Topic: Innovative Methods of Methane Detection Near the Face and De-energizing the Longwall Equipment

3.1 Problem Statement

Longwall mining is a high-production coal mining technology with several advantages. These include high recovery, a safe working environment, operator-friendly roof management, straightforward mine management and highly developed mechanization. In typical longwall operations, a working panel is usually more than 200 m in width and 2000 m in length[1]. The number of US underground coal mining operations using the longwall method for coal extraction is currently forty-three (2017) contributing approximately half of total underground coal production [2]. Although the longwall method offers distinct advantages of higher productivity and improved safety, it results in methane emissions that are typically higher than in room-and-pillar recovery on a per-ton-of-coal-mined basis. During the operation, the longwall panel progressively advances as the coal is continuously extracted and the immediate roof instantly caves behind the hydraulic shields. However, the overlying rock strata may hang-up with this cantilever loading the supports until it fractures [3]. The rock beam will break into large blocks and collapse when the span reaches a certain limiting value, depending upon the rock beam strength and integrity. The broken rocks, comprising the immediate roof and overlying strata, fill the mined void as gob. Longwall mining presents a unique hazard in mining by both liberating a large methane gas flux and also providing a large high-impedance methane

reservoir in the gob for its retention – a doubly hazardous outcome. Only a small fraction of the methane emitted into the mine ventilation system sources directly from the working face/freshly mined coal. The primary source of emission is from the gob, formed when the overlying strata collapse into the void created by longwall mining as shown in Fig 3-1. Thus, the characterization of gob gas emission is one of the most challenging tasks due to the complexity of the gas flow behavior [4,5]. Recent studies indicated that the flow behavior in and above the gob area is a multimechanistic process, including sorption, diffusion, advection and non-Darcian flows.

The vertical thickness of a gob can reach 4-11 times the mining height [6] with a highly irregular shape and comprising a broad distribution of granular block sizes. The broken rock mass is gradually compressed by the overburden load resulting from mining disturbance, as shown in Fig 3-1. The caved zone has generally high porosity and permeability resulting in a mass of gas storage, which is primarily derived from weak and fractured formations adjacent to the coal beds [7,8]. The rock-filled gob also supports the deforming upper rock strata; thus, the differential compaction of the heterogeneous gob directly determines the movement of the upper strata and indirectly controls the evolution of porosity and permeability both of the overlying rock strata and the gob itself. This feedback between overlying strata and gob significantly influences the gob gas-outing and the potential for spontaneous combustion - two major safety issues for longwall coal mines. Although compaction of the gob is a well-known issue, our understanding and characterization of differential loading, its impact on gob compaction, the resulting evolution of porosity/permeability and their impact on methane storage and discharge remains incomplete. Clearly, the behavior of the compacting gob and its interaction with the ventilation system (*e.g.* shield, face and bleeders) are very important for gas drainage, gas control and the suppression of spontaneous combustion.
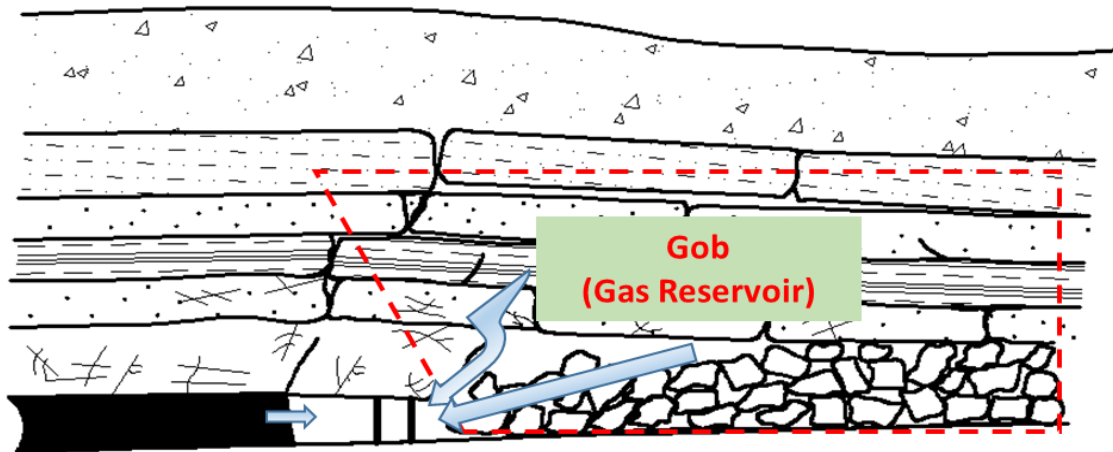
Figure 3-1: Overburden structure and gob distribution near the longwall working face. The red dash line is the longwall gob gas reservoir contributing the majority of gas emission towards the face as shown in light blue arrows.

The broken rock comprising the gob can be treated as a porous medium consisting of residual coal and broken rock sourced from the underburden and overburden. Due to the non-uniform stress distribution in the gob, the degree of compaction varies with location and time, resulting in a variable loading compaction and permeability evolution. Therefore, the mechanical properties of the broken rocks and their variable loading profile control the rock mass porosity, as well as the gas flow behavior in the gob. It is well known that the mining-induced gob stress profile near the working face region is asymmetric relative to the mining direction, as shown in Fig 3-2. The gob adjacent to the working face is at reduced stress due to the support of the hydraulic shields and the action of the overburden hinge structure. In this zone the broken rocks are loosely packed with a high macro-porosity and may experience turbulent gas flow. The load carried by the broken rocks in the gob gradually increases with distance from the face, resulting in progressive compaction and a decrease in porosity and permeability. Thus, the gas flow regime in this zone is expected to be a combination of turbulent and laminar flows. The stress level in the caved zone furthest from the working face almost recovers to the original *in situ* value and the gob will fully compact to a minimum porosity and permeability and will be dominated by laminar gas flow. In order to predict methane influx to the working face and bleeders from the gob, a comprehensive understanding of flow dynamics in the compacted rock is both necessary and essential. However, the gas flow behavior in these zones and their interactions has not been investigated in detail; nor is it well understood. We developed a systematic strategy to allow the quantitative characterization of emission and flow behavior in the gob zone and to build a physics-based model to quantify methane emission.
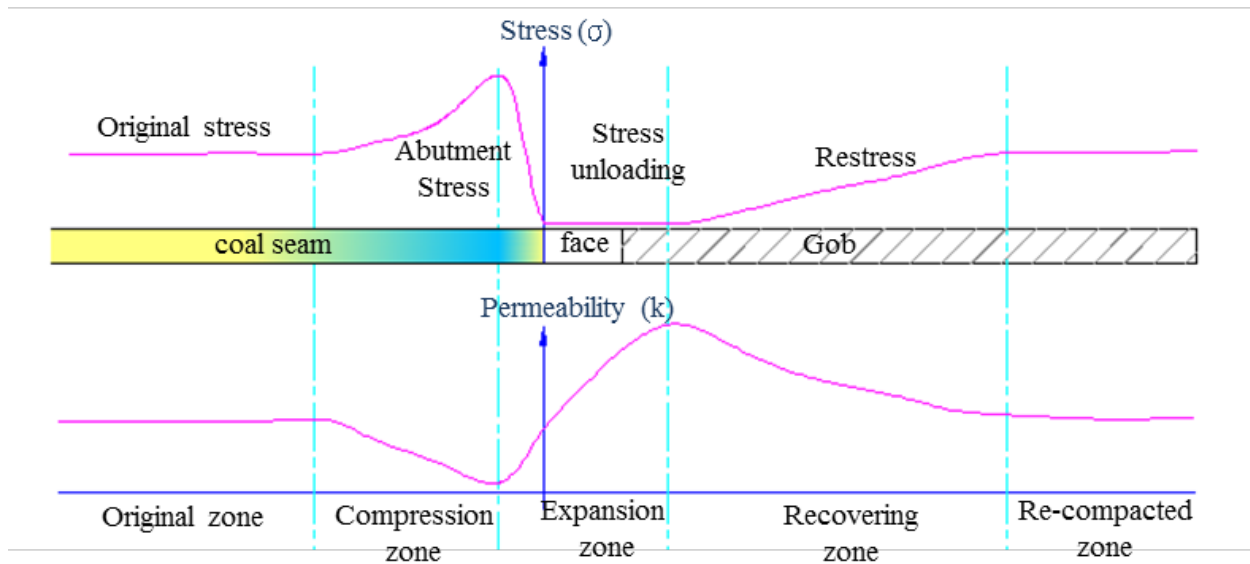
Figure 3-2: Stress distribution and permeability profiles around the longwall face.

The permeability of the compacted gob dramatically affects the ventilation systematics of the longwall face, including rates of fresh air leaked into the gob, rates of gas-outing towards the working face and control of spontaneous combustion. Although permeability of the gob

materials exerts a key influence on ventilation and gas control, the *in situ* measurement of porosity and permeability remains difficult [9,10] - with permeability characterization and prediction conducted only in sparing previous studies [9,11,12]. These previous studies, using either empirical or statistically-based models, laid the foundation for permeability characterization in gob-compacted rocks. However, they all lack a mechanistic quantification of permeability evolution under dynamic loading conditions through the full compaction cycle. Gob permeability is controlled by rock compaction, therefore, it is essential to build a mechanistic model to accommodate the principal components of this response. Gas transport properties, defined by gob permeability and storage, will ultimately determine the timing and intensity of gas emission to the face, tailgate corner and bleeder systems.
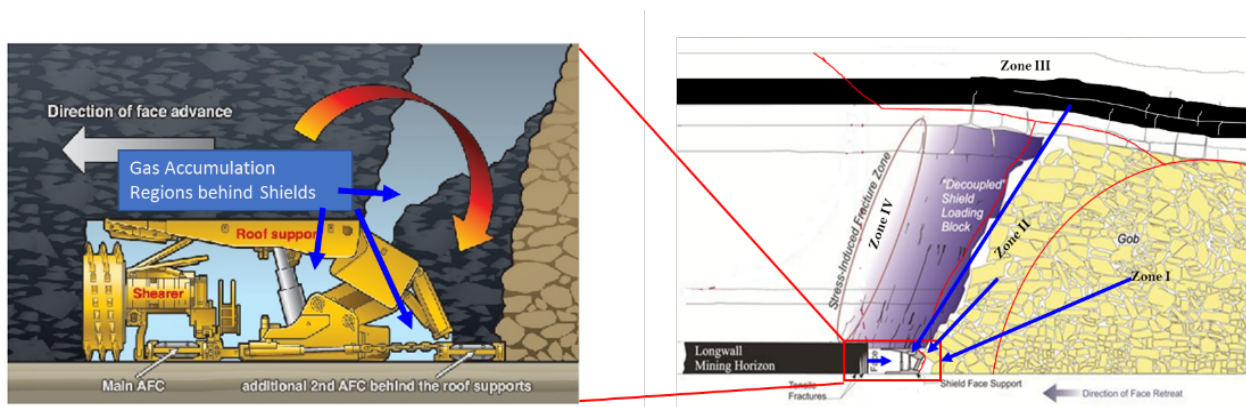
Figure 3-3: Conceptual gas accumulation around the shields: left – gas can be accumulated near the shields where turbulent eddies exit as shown in blue arrow; right- possible gas transport zones at the longwall face and gas can be emitted from fully compacted zone-I, loosely compacted zone – II, adjacent upper coal seam through void zone – III and from the face shown as blue arrows.

The detection and control of methane emissions from longwall gobs is an ongoing problem despite efforts to prevent threshold-exceeding gas-outing. The longwall face, the area directly behind the shield, is of great interest because it was believed the root cause of the gas explosion in the Upper Big Branch (UBB) disaster [13]. As previously mentioned, the overlying strata above the immediate roof may not immediately collapse or cave, and the hanging strata can create a large open void space behind the shields as shown in Fig 3-3. This open void space provides a much larger volume for gas to accumulate; as opposed to the crevices in the compacting gob. In addition, there are no specific requirements to monitor this area directly around the shields (CFR30 Part 75.342). This is especially troubling as gas can become trapped in turbulent eddies and could accumulate to hazardous levels. This is an area that has already been implicated with explosions in the past. An accumulation of methane around the shields near the tailgate is what investigators believed to be the source of the explosion in the Upper Big Branch [13]. It is also evident that the methane sensors at the face failed to record/report the methane accumulation behind the shield. In the Report to the Governor of West Virginia on the UBB explosion, it is

clearly stated that "it is possible that methane could have migrated to the canopies of the shields and reached the explosive range, and that the ventilation plan didn't sufficiently dilute this methane accumulation"[13]. Similarly, the MSHA report on the UBB explosion concluded that "a fire behind the shields burned for in excess of 2 minutes before it migrated to the tailgate where it met pockets of methane gas" [14]. Fatal lessons learned from UBB demonstrate that an improved understanding of gas transmission from the gob to the shield void is needed, together with knowledge of how the methane accumulates within this confined void space.

In order to better understand and model the gob gas emission behavior, knowledge of gob compaction, gas transport in gob and its interactions with ventilation system is required. In this study, we aimed at answering the following specific questions, including: (1) what is the influence of the variation of atmospheric barometric pressure on gob gas emission; (2) what is the difference between the exhausting and forcing ventilation system on gob gas emissions; (3) how does tailgate entry failure/convergence influence gob gas emissions to the face; and finally (4) what are the optimal bleeder fan operating conditions to achieve the best gob gas control.

3.2 Project Objectives

The overarching goal of this project was to develop appropriate strategies to characterize and model methane emission and transmission from the gob to the mine ventilation system and to effectively mitigate impacts of elevated methane concentrations for longwall mines.
The flow behavior in the compacted gob zone was characterized and modeled using both experimental and analytical investigations. This mechanistic model was then be applied to quantify and predict gas emission rates into the working face and ventilation system. A numerical study of gas emission from gob to the face was conducted. Mine site measurement and monitoring data were used to validate the models. The knowledge gained through this research workflow was transformative as it provides a needed, new and mechanism-based understanding of fluid dynamics in the gob as well as airflow dynamics at the working face. This study provides a systematic strategy to evaluate gas emissions at the working face and to control methane concentrations in longwall underground coal mines.

3.3 Project Specific Aims

This objective was pursued by achieving four specific aims.

Aim 1: determine rock compaction behaviors and quantify flow behavior for longwall gob;

Aim 2: Develop the analytical dynamic permeability evolution models for gob rocks based on rock compaction and *in situ* stress;

Aim 3: develop CFD model to define the airflow dynamics in the gob and its interaction with ventilation system;

Aim 4: conduct the field measurements in the longwall partner mine to quantity the gas emission from gob to the mine ventilation system.

4.0 Research Approach

To achieve the objective of the project, we used an integrated program of experiment, modeling and in-mine field measurement and validation to develop a systematic strategy to assess and predict the gas emission behavior from gob to the mine ventilation system. The research approach can be summarized as follows:

4.1 Gob material collection and laboratory compaction under dynamic loading

We collected coal and gob rock samples to characterize coal/rock properties in the laboratory. The experimental data were used as input parameters for the analytical permeability model (section 5.1.2) as well as the numerical model of gas emission (section 5.2.3). We conducted gob compaction experiments using in-mine-collected fragmented rocks to simulate the *in situ* compaction and the mechanical properties were reported in section 5 of this report. Observed compaction is linked to a capillary model representing porosity reduction and permeability evolution, as detailed in sections 5.1.2 and 5.1.4.

4.2 Analytical modeling of dynamic permeability evolution for gob rocks with continuous compaction

Based on the mechanical behavior of the broken rock mass with uniaxial loading, we proposed the mechanism-based porosity and permeability models. For the permeability and porosity models, an improved stress-strain evolution model was adapted and the model was then scaled through the evolving compactive strains and particle size distribution of the fragmented rock. This enables results to be up-scaled to mine-scale, as detailed in sections 5.1.3 and 5.1.4.

4.3 In mine-wide ventilation survey and methane concentration monitoring

We partnered with one deep longwall coal mine for our field tests. We documented a mine-wide ventilation pressure and flow rate survey (p-Q survey) to establish a ventilation network model – including methane gas concentrations recorded at selected face locations, as detailed in section 5.2.2. During the survey, air velocity, pressure and gas concentration data were survived and collected. The data was used to build the mine ventilation network model using the

Ohioautomation ICAMPS-MineVent software package (section 5.2.5.2). The ventilation network model was calibrated and validated using the measured ventilation survey results. In addition to the routine mine ventilation survey, special effort was made to measure methane liberation and flow around the longwall shields. This included the measurement of methane liberation from the area immediately behind the shields and into the longwall face and tailgate corner. The detailed field work was presented in section 5.2.2. Then the validated ventilation model was used to analyze the effects of gas emissions from gob-to-face on the ventilation system, as detailed in section 5.2.4.

4.4 Numerical modeling for quantifying gob gas flow behavior in scaled model and predicting gob gas emission from gob to face in mine-scale

We developed CFD model to define the airflow dynamics in the gob and its interaction with ventilation system using the Penn State scaled mine ventilation model (section 5.3). We also proposed an analytical pressure gradient model to evaluate gob gas emission and its interaction with the ventilation system. This model combines viscous energy losses along a tortuous gas flow path within the gob materials with kinetic energy losses at irregular cross-sections, as proposed in section 5.2.3. A numerical gas emission model was also established to predict gas emission rates at the longwall face and to dynamically determine the gas emission rate from the compacted gob. The numerical network model of the mine was validated then calibrated against the field methane monitoring results at our partner mine, as discussed in section 5.2.4.

5.0 Summary of Accomplishments

5.1 Continuous compaction and permeability evolution in longwall gob materials
5.1.1 Introduction and Background

Longwall mining is an efficient and economically favorable method for the recovery of coal [15,16]. In a typical longwall mining system, the longwall panel advances incrementally as the coal is continuously extracted[1]. Ideally, the unsupported immediate roof and the overlying strata will fracture and collapse to form the gob – avoiding excessive cantilevered loading by the intact roof to the face supports. This caved zone will compact as the face advances and arching support diminishes. This jumble of irregular caved blocks of rock and residual-coal fill the caved zone and form the dynamic gob region. Depending on the degree of compaction of the caved gob materials, the height of the caved zone may reach ~4-to-11 times the thickness of the coal seam[17,18]. Within the mine gob region, the compacted rock/coal mass provides viable, complex and dynamic pathways for airflow and the concurrent migration of methane [19]. Although the gas flow pathways may constrict with compaction, the high permeability pathways will endure and will affect the leakage of ventilation airflow from working face to the gob, the flow of

15

methane from surrounding sources towards the gob and into the mine face, and the performance of methane extraction gob gas ventholes [17,18,20]. Thus, understanding and predicting the compaction behavior of the caved zone can provide a mechanism-based approach to define the evolution of gas flow behavior and in proposing effective gas mitigation strategies. The goal of this is to minimize gas-outing and its related mine safety hazard.

The overburden stress in the caved zone evolves dynamically as a result of repetitive loading then unloading[21]. This quasi-static loading modulates porosity and permeability as a function of both stress-induced deformation and stress-induced damage[22,23]. Where evolving tensile or shear stresses exceed the truncated-Mohr-Coulomb failure criterion, the broken rock blocks comprising the gob will fail and compact towards a final equilibrium state. Thus, the overburden stress profile and its evolution uniquely determine the deformation in the caved zone, the dimensions and shapes of the broken rock together with the associated evolution of porosity and permeability.
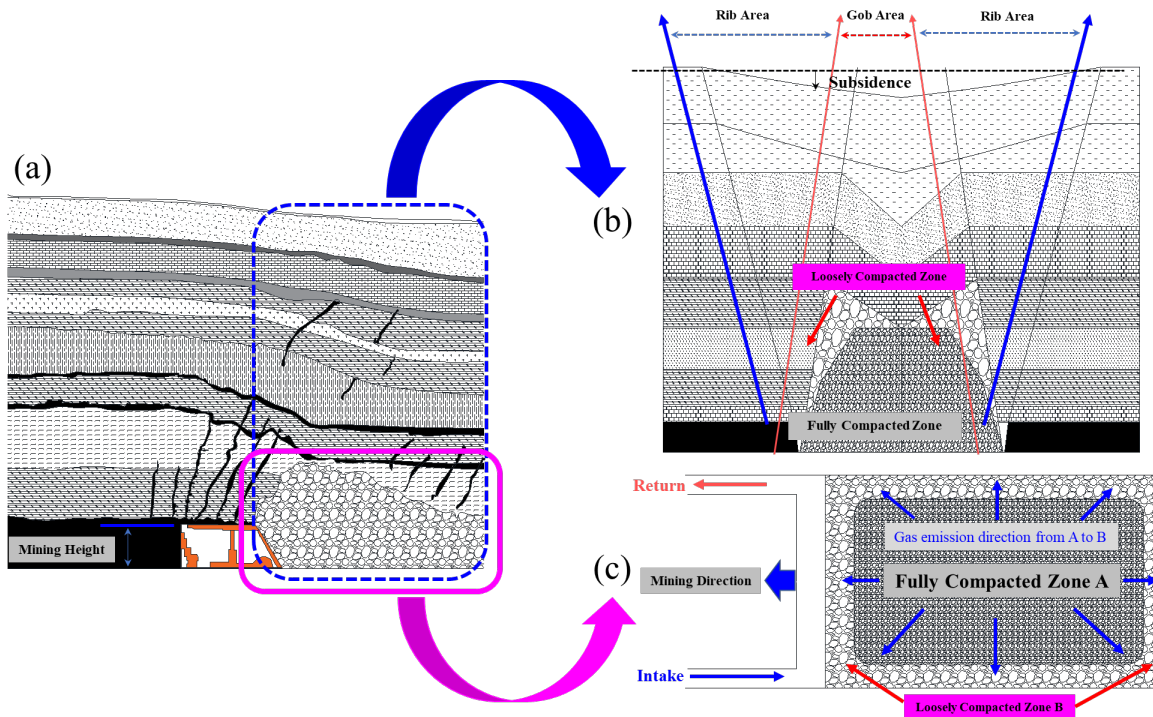
Figure 5-1: Schematic of longwall mining and the distribution of rock/coal mass in the gob region: (a) Schematic representation of longwall mining with a shearer (modified from Karacan (2009) [18]). (b) Gas-flow model proposed for the gob area and rib area (modified from Forster and Enever (1992)[24]). (c) Plan-view of the interior compacted gob zone skirted by a lighly-compacted O-shaped ring.

The gob compaction process can be idealized as one-dimensional quasi-static consolidation [19]. Figure 5-1 shows a schematic representation of longwall mining with a shearer as well as the distribution of rock/coal mass in the caved gob. Field observations [12,24,25] suggest a gas drainage model illustrated in Figure 5-1(b). Indeed, the caved rock mass comprising the gob is

heterogeneous but structured as a permeable ring ("O-shaped") skirting the more-fully compacted gob to the interior (Figure 5-1(c)). This structure results from the action of the rib supports, is commonly ignored, but significantly influences the stress and permeability distribution (Figure 5-1(c)) through this loosely compacted zone (B). Vertical compaction within this zone mobilizes friction from the local rib confinement along the boundary between the rock mass and the rib. This frictional force rotates the principal stresses within the loosely compacted Zone B. Thus, the compactive behavior within this skirting "O-shaped" ring will be linked to the local rib confinement (Figure 5-1(b) and (c)), concomitantly impacting the porosity and permeability evolution.

We present experimental observations of scaled-gob compaction and dynamic permeability evolution using mine roof-rock materials. We develop an analytical model to evaluate the re-distribution of stresses within the loosely compacted Zone B adjacent to the rib. This defines the impact of the local shear stress on the volumetric response of the gob rock mass and its impact on permeability. The analytical models are validated against available observations with probability density functions of the particle size distribution providing the link between laboratory and field scale behaviors. The validated models are then used as mechanism-based model to predict porosity and permeability evolutions in the longwall gob region.

As the longwall mining panel progressively advances, the gob rock mass, including the immediate roof rock, overlying strata, and residual coal gradually compacts. The resulting compactive state is highly related to the dimensions, gradation, shapes and distribution of the broken rock blocks [26–30]. The grain size distribution also influences the mechanics of fluid transport in the fragmented medium [19]. The grain size distribution of the fragmented rock blocks is one key property that links laboratory scale response to field scale – mobilizing the power of digital imaging [31]. Mechanical deformation may be digital imaged to establish a three-dimensional (3D) model then allowing the simulation of stress-seepage coupling effects [32]. The disordered nature of the broken rock blocks is amenable to fractal description for the fragment size distributions enabling fractal porosity and permeability models to be developed. Specifically, the permeability and porosity expressions can be shown as [19]:

$$k = \frac{\pi}{16A_T} \frac{L_0^{(1-D_T)}}{\alpha} \frac{D_P}{2.531+D_T-D_P} r_{max}^{2.531+D_T} \left[1 - \left(\frac{r_{min}}{r_{max}}\right)^{2.531+D_T-D_P}\right] \quad (1)$$

where k is the permeability, m²; A_T is the total area to flow, m²; L_0 is the representative length, m; α is the shape factor in the Hagen-Poiseuille equation, dimensionless; D_T is the tortuosity fractal dimension, fractal dimension; D_P is the pore-area fractal dimension, fractal dimension; r_{min} and r_{max} are the minimum and maximum pore sizes respectively, m, and:

$$\phi_{i+1} - \phi_i = -\Lambda \left[\frac{\sigma_{i+1}^{\frac{m(D_F-1)}{2}-1}}{\frac{m(D_F-1)}{2}-1} - \frac{\sigma_i^{\frac{m(D_F-1)}{2}-1}}{\frac{m(D_F-1)}{2}-1}\right] \quad (2)$$

where ϕ_{i+1} and ϕ_i are successive porosities under compaction, dimensionless; Λ is plastic compressibility index, 1/MPa; D_F is the fragmentation fractal dimension, fractal dimension; m is the Weibull modulus, dimensionless; σ_{i+1} and σ_i are the applied macroscopic stresses, MPa.

The above fractal theory-based models are essential in understanding the effects of particle size/spatial distribution on the evolution of porosity and permeability. Incorporating the evolution of average stress enables dynamic compaction effects to be explicitly incorporated into the permeability model. In addition to porosity and permeability models accommodating fractal theory, the Carman-Kozeny equation may be applied to estimate gob permeability as [33]:

$$\frac{k}{k_0} = 0.241 \left[\frac{\phi^3}{(1-\phi)^2} \right] \tag{3}$$

where k_0 is the initial permeability of the broken rock at the maximum porosity, m2; and ϕ is the porosity, dimensionless. One concern related to Eq. (3) is the determination of the initial permeability, which is challenging due to the inaccessibility of the gob environment. Experimental friction factors for fluid flow through the crushed stone [34,35], define this initial permeability as ~106 md, as used elsewhere in the reservoir modelling of longwalls [36].

Gob permeability is highly dependent on the in situ overburden stresses [37]. Semi-empirical formulae quantify fractured rock permeability, defining an exponential relationship between permeability and the volumetric strain as [38]:

$$k = -4 \times 10^{-16} \varepsilon_v^3 - 6 \times 10^{-15} \varepsilon_v^2 - 7 \times 10^{-14} \varepsilon_v + 10^{-11} \tag{4}$$

where ε_z is the volumetric strain, dimensionless. In addition, exponential relations link fracture permeability to stress as [39]:

$$k_v = k_{v0} \exp\left[-0.25(\sigma_{zz} - \sigma_{zz0}) \right] \tag{5}$$

$$k_h = k_{h0} \exp\left[-0.25(\sigma_{xx} - \sigma_{xx0}) \right] \tag{6}$$

where k_v and k_h are the independent permeabilities in the vertical and horizontal directions, m2; k_{v0} and k_{h0} are the initial permeabilities, m2; σ_{zz} and σ_{xx} are the prevailing stresses and σ_{zz0} and σ_{xx0} are the initial vertical and horizontal stresses, respectively, MPa.

Such models of porosity and permeability are stress-dependent. Stress-induced rock mass deformation and damage can significantly impact porosity and permeability ass. Specifically, the stress-dependent permeability can be linked to porosity evolution (Eqs. (1) and (3)) or directly developed from the impact of stress level on volumetric strain (Eqs. (4-6)). These models implicitly show that the stress level, as well as the stress-dependent rock mass properties drive the dynamic changes in porosity/permeability. Significant effort has been devoted to characterizing the stress-strain relationship for gob rock masses. The classical quantitative stress-strain relationship for compacting gob can be defined as:

$$\sigma_v = \frac{E \varepsilon_v}{1 - \varepsilon_v / \varepsilon_m} \tag{7}$$

where σ_v is the vertical stress, MPa; E is the initial tangent modulus of the broken rock, MPa; ε_v is the vertical strain, dimensionless; ε_m is the limiting maximum vertical strain, dimensionless. Among these parameters, E and ε_m can be quantified as [40]:

$$E = \frac{10.39\sigma_c^{1.042}}{b^{7.7}}, b = 1 + \frac{c_1 h + c_2}{100}, \qquad \varepsilon_m = \frac{b-1}{b} \tag{8}$$

where b is the bulking coefficient, dimensionless; σ_v is the maximum uniaxial compressive strength, MPa; c_1 and c_2 are the coefficients related to the strength of the immediate roof; h is the height of the caved zone, m. Based on the assumption of elastic response, a conceptual model for the stress-strain constitutive law may be developed by assuming that the contact connection between two adjacent rock particles is similar to that in a cubic mass [1]:

$$\sigma_v = \frac{E_b}{\alpha} \varepsilon_v \tag{9}$$

where E_b is the elastic modulus of rock particles, MPa; α is the uniaxial elastic modulus coefficient, dimensionless. In addition to the evolving stress level in the caved zone, the stress-dependent material properties are also sensitive to the stress level. Based on deformation experiments, the stress-dependent secant modulus exhibits a linear relationship with the stress level as [41]:

$$E = a\sigma_v + b \tag{10}$$

where E is the secant modulus of the rock particles, MPa; a and b are the experimental fitting parameters, dimensionless. Also, the elastic modulus and Poisson ratio of the caved rock mass evolve with the one-dimensional consolidation [40]. Typically, the bulk modulus of the broken rock blocks evolves with the accumulation of vertical strain and the maximum vertical strain, as:

$$K = \frac{4G}{3} = \frac{E_0}{2(1-\varepsilon_v/\varepsilon_m)} \tag{11}$$

where G is the shear modulus, MPa; and E_0 is the initial tangent modulus of the broken rock blocks.

Previous studies mainly concentrated on empirical and regression-fit experimental observations. Some analytical models attempted to link stress-induced deformation and damage with the evolution of porosity and permeability[42,43]. Accommodating stress-dependent rock mass properties improved predictions of volumetric response and gas flow behavior in the caved zone. However, the majority of these studies assume that the overburden stress is the only compactive force impacting porosity and permeability evolution, neglecting the important role of rib confinement, as illustrated in Figure 5-1(c). This project explores this important control on permeability evolution. An improved stress-strain evolution model is used as a mechanism-based model to predict porosity and permeability evolutions in longwall gob. This improved permeability evolution model is then used for the prediction of methane emissions from the gob to the face - providing a rational basis for longwall ventilation design and planning.

5.1.2 Gob material collection and laboratory compaction under dynamic overburden loading

Caved broken rock mass was collected from a deep longwall mining operation in China at the Tangkou coal mine. The Tangkou coal mine is located in Jining city, Shandong Province, China. The actively-mined seams are of Permian (Shanxi formation) and Carboniferous (Taiyuan formation) (Figure 5-2 (a)) ages. These comprise six coal seams numbered as #3, #6, #10, #15, #16 and #17 (Figure 5-2 (a)) with the #3, #16 and #17 as the primary targeted seams for longwall mining. Annual production is planned at ~5 million tons/yr [44]. The #3 coal seam is mined by the LTTC mining method and is the object of this study. A field in-mine ventilation survey was conducted at the 6304 working face within the #3 coal seam, subject to the panel layout illustrated in Figure 5-2 (b). The average thickness of the coal seam at the 6304 working face is ~ 9.76 m, with a detailed mine layout presented in section 5.2.2 [44]. An initial width of 182 m transitions to a final narrow panel width of 60 m with a working face length of ~1565 m (Figure 5-2 (b)).
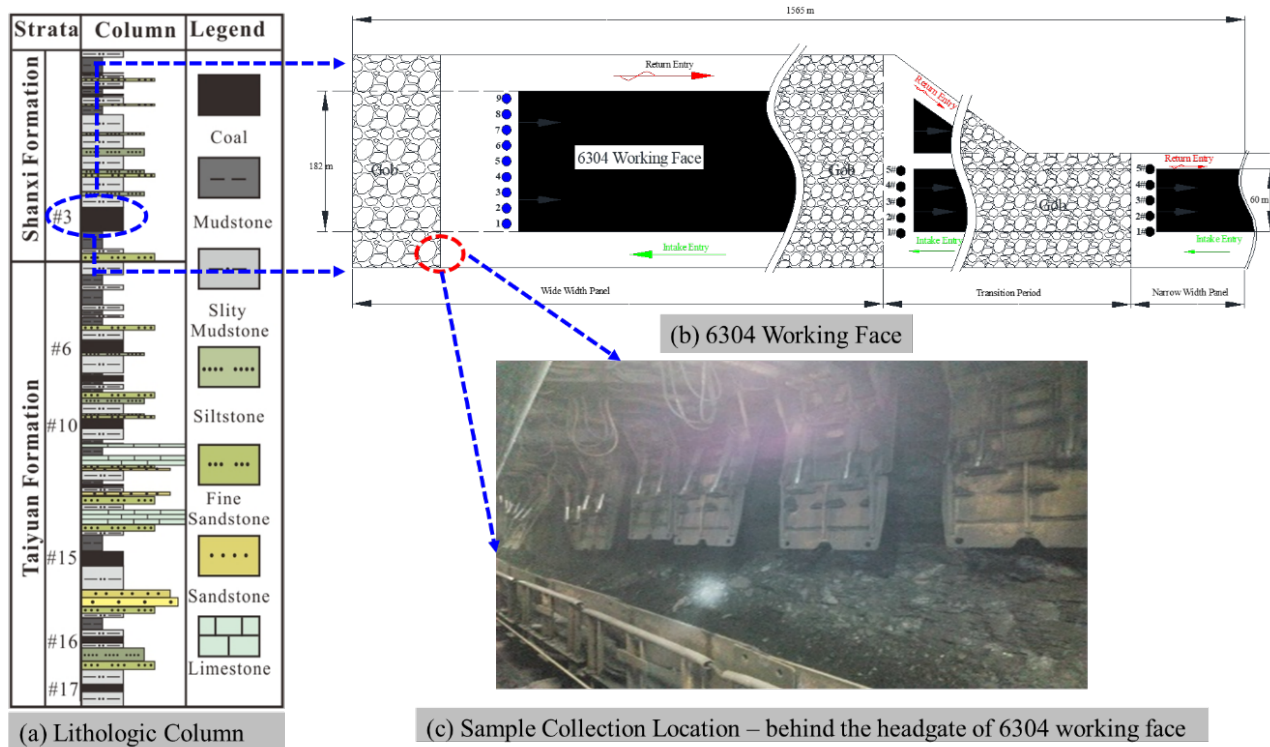
Figure 5-2: Schematic of the 6304 working face and sampling location: (a) Lithologic column. (b) 6304 working face. (c) Sample collection location behind the shields.

Compaction experiments used caved rock from multiple locations immediately behind the shield following caving, as shown in Figure 5-2(c). The density of the collected mudstone sample was measured as ~ 2.1 g/cm³. The collected caved rock blocks were manually selected

with diameters less than 25 cm. The broken rock samples were classified into fractions with edge dimensions $\leq 5cm$, $5cm - 10cm$, $10cm - 15$ cm, and $15cm - 25cm$ (Figure 5-4). These blocks were used in compaction and flow experiments in the laboratory.

The experiments simultaneously measure both displacement and flow in the simulated gob samples. The experimental system (Figure 5-3) comprises a high-stress uniaxial (zero lateral strain)) rock compaction chamber to contain the caved rock mass (Figure 5-3(a)). The cylindrical chamber is 40 cm in diameter and 60 cm in height, as shown in Figure 5-3(a). The chamber was placed in a loading frame with a maximum loading capacity is 600 kN with both axial load and vertical displacement continuously monitored.
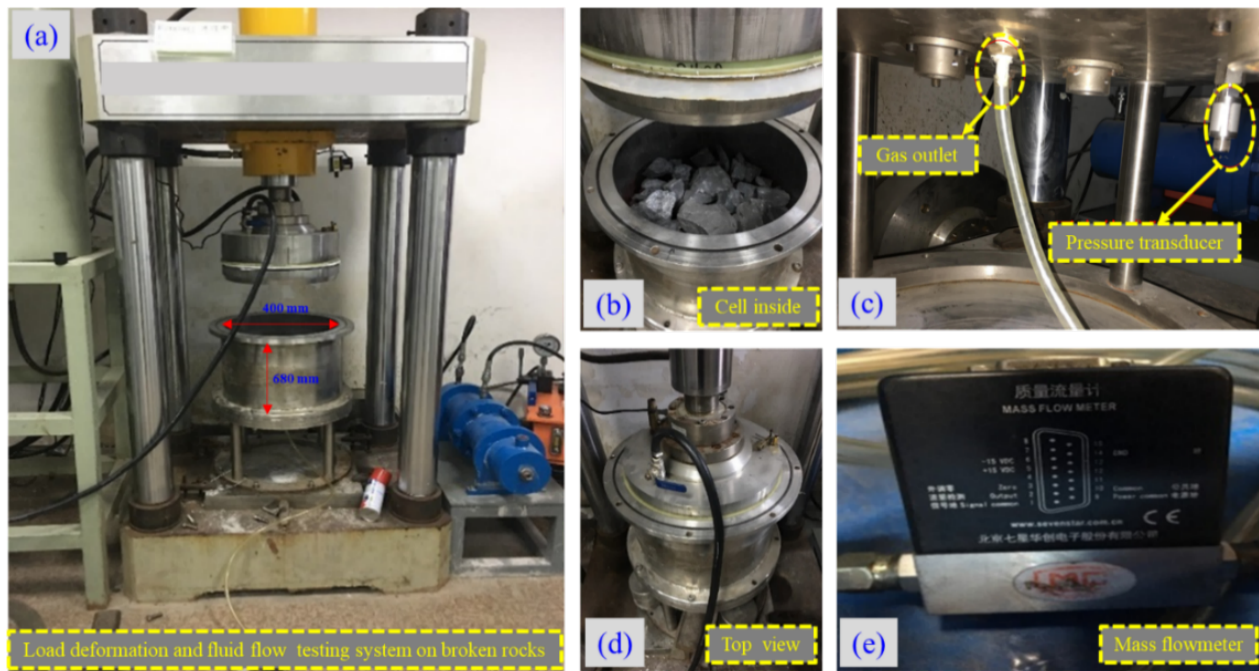
Figure 5-3: Schematic of the experimental setup. (a) Schematic of the displacement and flow measurement system. (b) Top view of the sample chamber. (c) Gas outlet and pressure transducer. (d) Exterior view of the sample chamber. (e) Mass flowmeter.

Field observations (Figure 5-1(a)) identify distinct layering in the caved rock mass – with component rock block sizes increasing in size from floor to roof. To replicate this observed structure, experiments were conducted in two modes (Figure 5-4): Test A with layers gradually coarsening-upwards and Test B with similar coarsening-upwards layers capped with single coarse top layer. In Test A, the rock samples (dimensions of ≤ 5 cm and 5 cm -10 cm) were packed in the first layer with the mass ratio of 1:4. That is, 20% by weight of ≤ 5 cm and 80% by weight of 5 -10 cm, packed as the first layer as shown to the bottom left of Figure 5-4. For the second layer, the mass ratio remains as the same at 1:4 but with incremented gradations of 5 - 10 cm and 10 - 15 cm, respectively. The third layer is finally packed with further incremented

gradation dimensions of 10 - 15 cm and 15 − 25 cm again at a 1:4 mass ratio. All three layers in Test A have the same packing height of approximately 8 cm and the same rock mass weight of ~7.5 kg, as shown in Figure 5-4. Similarity, the new four layers of the second test B were packed as shown in Figure 5-4. The four layers in Test B again have a uniform packing height now of approximately 5 cm and the same rock mass weight of ∼ 4.5 kg in each layer – but the uppermost capping layer comprises the coarsest fraction, only – representing the in situ observation of a coarse-graded top-gob. For both Tests A and B, the loading rates were set as 0.1kN/s and 0.05 kN/s, respectively, with the maximum applied loads for the two tests as 300 kN and 200 kN, respectively.
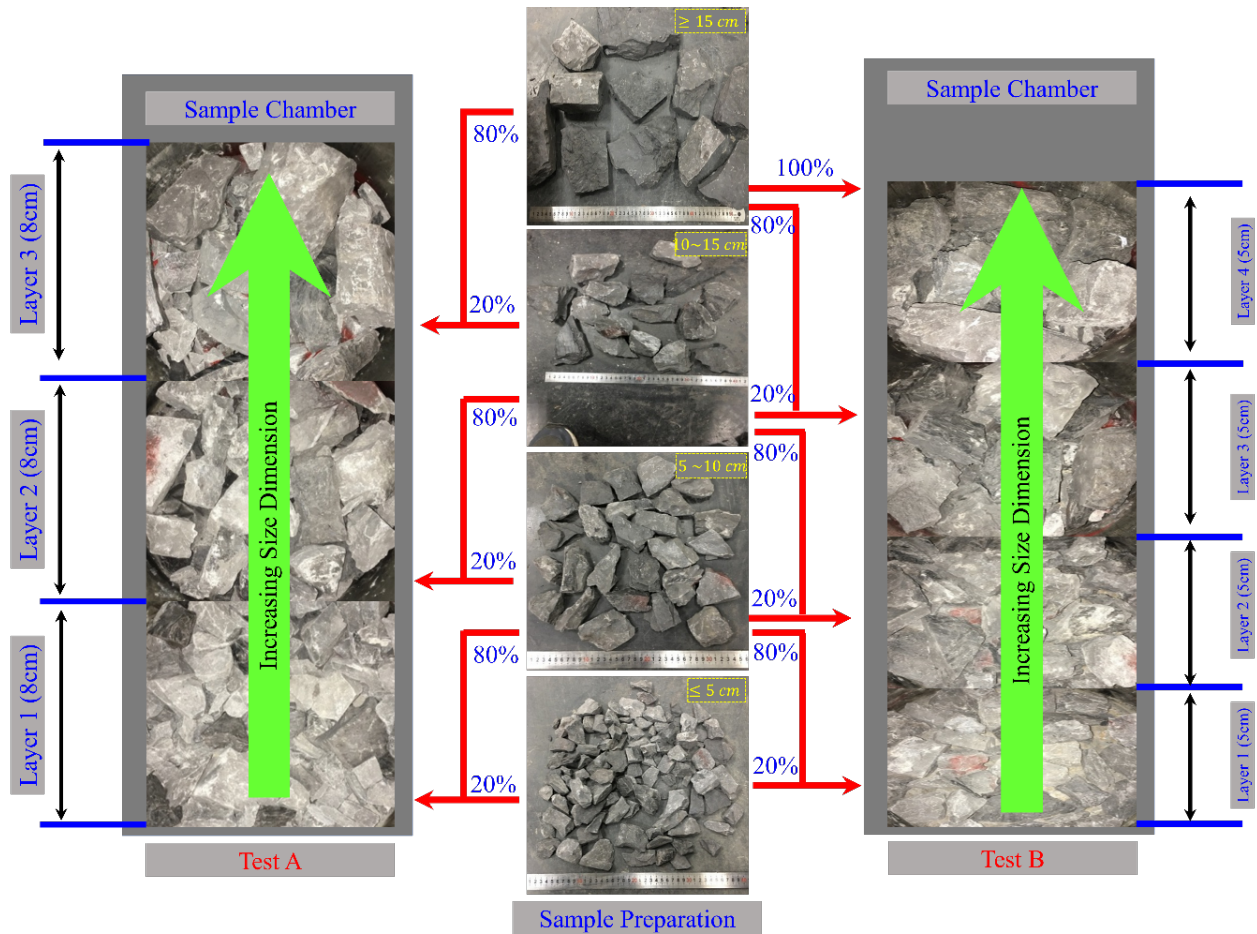
Figure 5-4: Schematic of experimental design for Tests A and B.

(a) Test A

(b) Test B
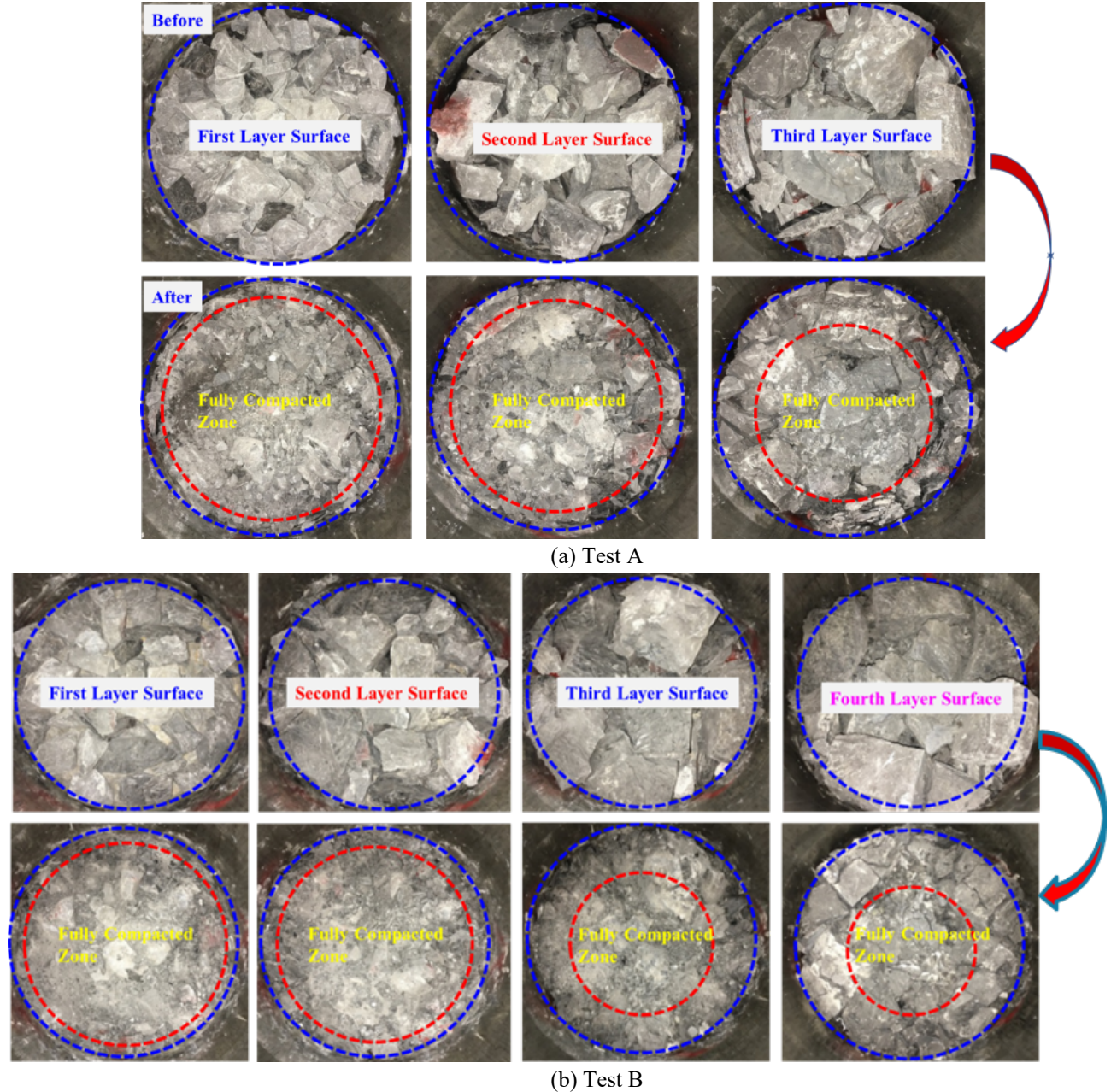
Figure 5-5: Mine-roof rock mass both before (top) and after (bottom) compaction experiments of Tests A and B.

Figure 5-5 shows images of the fragmented rock mass both before then after the compaction experiments for the contrasting gradations of Tests A and B. Apparent is that the rock blocks in all layers compact, crush and fail into smaller-sized fragments. In both Tests A and B, the fragments in the center of the sample were fully compacted with those on the periphery relatively loosely compacted and less damaged - a direct miniature analog of behavior at gob scale – although this is not the focus of the experiments. For both Tests A and B, the lower layer (i.e. basal layer) was severely compacted and crushed compared to the upper layers (i.e. layer 3 in test A or layer 4 in test B). This is attributed to the smaller sized fragments present in the basal layer are subject to higher stress concentration than the upper layers. The experimental

results indirectly represent the "O-shaped" type compaction behavior for the gob at lab-scale, analogous to Figure 5-1(c) as a result of rib support and friction induced forces.

Figure 5-6(a) shows the mechanical response of the fragmented rock under uniaxial loading. The stress-strain curves show distinct differences between the gradations of Tests A and B. The response may be separated into two segments - initial high-compaction followed by elastic compaction (Figure 5-6(a)). During initial compaction, the stress-strain response remains flat with the initial small applied seating stress. After the initial compaction, the response switches to linearly elastic. For the continuously coarsening-upwards gradation of Test A, a strain of ~0.25 is the threshold to elastic response at an average stress of ~ 0.38 MPa (48.33 kN). The average stress is computed from the force applied over the average cross-sectional area of the experimental chamber. The maximum strain for Test A is ~0.39 corresponding to a maximum stress of ~1.95 MPa (245.26 kN) during the second load cycle. For Test B, ~ 0.17 is the threshold strain for elastic response representing an average stress of 0.41 MPa (51.38 kN). The maximum strain is ~ 0.30 at a stress of ~1.59 MPa (200 kN). Although similar two-stage trends are observed for both Tests A and B, comprising the same materials, the differing thresholds result from the different stacking and packing configurations – both are coarsening-upwards but Test B has a larger gradation and is capped with a single course layer. This indirectly suggests that the overburden strata control gob compaction as illustrated in Figure 5-1(b). Based on the experimental data, we infer that the gob material can be treated as a linear and elastic medium after an initial seating-in compaction. However, the elastic assumption may not be appropriate for the initial compaction period with excessive deformation under low stress conditions.

For both Tests A and B, the porosity of the fragmented rock mass in the sample chamber was calculated from $\phi = \frac{V_r}{V_c}$, where V_r is the total volume of the broken rock blocks - total volume of the sample is assumed constant as $V_r = \frac{m}{\rho}$ (where m is the total mass of the sample, ρ is the density of the rock sample). V_c is the time-dependent volume of the sample chamber in use, which includes the constant sample volume and the stress-dependent void volume. The time-dependent volume V_c is calculated from $V_c = A(H_0 - S)$, where A is the cross-sectional area of the testing chamber, H_0 is the initial packing height of the sample and S is the compactive deformation of the load point. Thus, the stress-dependent porosity is recovered from $\phi = \frac{A(H_0 - S) - \frac{m}{\rho}}{A(H_0 - S)}$. As shown in Figure 5-6(b), the porosities in both tests decrease nonlinearly with increasing stress at relatively low stresses. In Test A, the porosity decreases from 0.64 to 0.41 (~ 36%) as stress increases from 0 to ~ 1953 kPa, while for test B the porosity decreases ~23% from 0.66 to 0.51 at the maximum stress of ~ 1592 kPa.

Finally, we note that only materials from the immediate roof were collected and used – as the upper caving zone materials are inaccessible. As such, these experimental results provide at least a preliminary evaluation of the stress-strain behavior for the gob materials. Future studies might incorporate the upper overlying strata, representing the detachment zones, potentially at higher stresses and on larger grades samples.
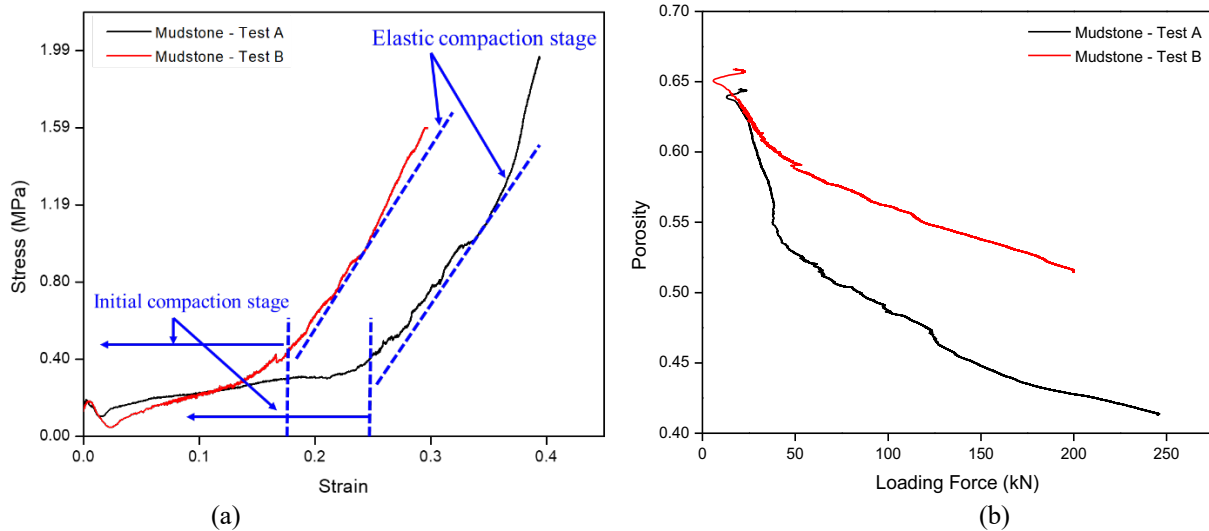
Figure 5-6: Mechanical behavior and porosity evolution of the broken roof-rock masses under uniaxial loading. (a) Stress-strain response. (b) Porosity evolution.

5.1.3 Modelling of porosity and permeability of fragmented rock medium

With continuous advancement of the longwall panel, the overlying roof strata behind the support shield may "hang-up" as a rock cantilever before breaking into rock blocks with irregular shapes and sizes within the gob [1].The caved gob will gradually consolidate due under the overburden load and porosity and the permeability evolve with time. Prediction of porosity and permeability is important in defining mitigation strategies to minimize gas (mainly the fugitive methane) concentrations and related hazard. From the compaction experiments in the lab (Figure 5-6 (a)), the gob materials show elastic properties as they fully compact, suggesting this as an appropriate model for uniaxial consolidation.

5.1.3.1 Stress distribution within the caved gob

In longwall mining, the caved zone can reach 4 – 11 times the thickness of the mining height where overburden rocks are weak and porous [19]. In the caved zone, the broken rock mass stacks layer by layer with continuous caving, as shown in Figure 5-7(a). Failure begins with the immediate roof strata with the overlying strata sequentially stacking on the gob and loaded by the overburden. Mohr's circle may be used to describe the state of stress in the gob –

representing the Mohr – Coulomb failure envelope as shown in Figure 5-7(b). In Figure 5-7(b), the vertical stress (the maximum principal stress) can be estimated from the overburden load – overburden average density×gravitational acceleration×height ($\rho g h$). This ignores friction along the boundary between the fragmented rock medium and the rib resulting from movement in vertical direction. As illustrated in Figure 5-7(b), if the frictional force is ignored, the overburden stress and the horizontal component due to the Poisson effect, should be the maximum and minimum principal normal stresses. The maximum principal normal stress in the vertical direction increases with an increase in overburden depth with the induced horizontal stress (the minimum principal stress) proportionally increasing (Figure 5-7(b)). For example, as the maximum principal normal stress increases from V_1 to V_2, the corresponding horizontal stress induced by the Poisson effect increases from H_1 to H_2. Theoretically, the overburden stress and the horizontal stress are location-dependent, as identified in Figure 5-7(b), while in practice quantifying them is challenging (this will be discussed in Section 6.1). Simplifying, we assumed that the local overburden stress (σ_v) and the horizontal stress (σ_h) in the following derivations are the average values (Figure 5-7 (a)). It should be noted that the shear stress (Figure 5-7(a)) is the combined effects of the horizontal stress and the movement of the rock mass in the vertical direction, based on Amonton's law ($\tau_N = f\sigma_h$, where τ_N is the shear stress and f is the friction coefficient).

(a) (b)
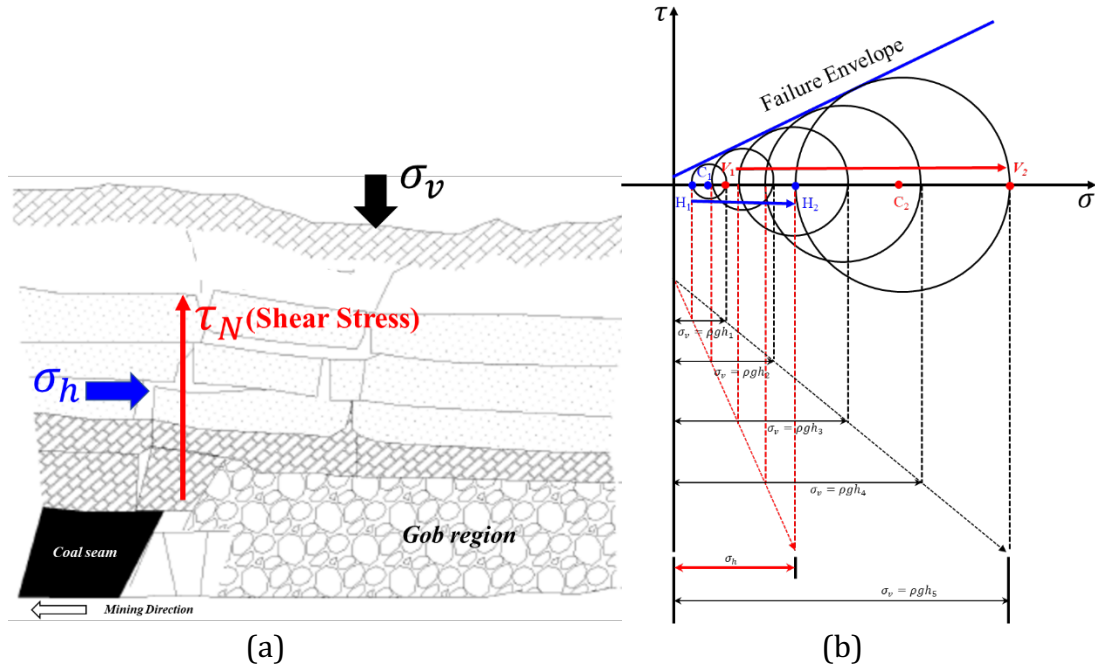
Figure 5-7: Schematic of (a) gob compaction and (b) Mohr's circle stress diagram for different cave heights.

As shown in Figure 5-1(b), the fragmented rock mass deforms with the overburden load. Due to the Poisson effect, a horizontal stress is applied to the fragmented rock mass by the rib. Due to continuous compaction, the friction force is generated at the rib to resist the vertical displacement of the compacted rock mass in the loosely compacted Zone B, illustrated in Figure 5-1. This induced shear resistance along at the rib changes the state of stress in the loosely

compacted Zone B. As illustrated in Figure 5-8, the principal stress coordinates at the immediate gob rock mass in Zone B are rotated with the rotation angle depending on the intensity of the shear resistance between the rib and Zone B.
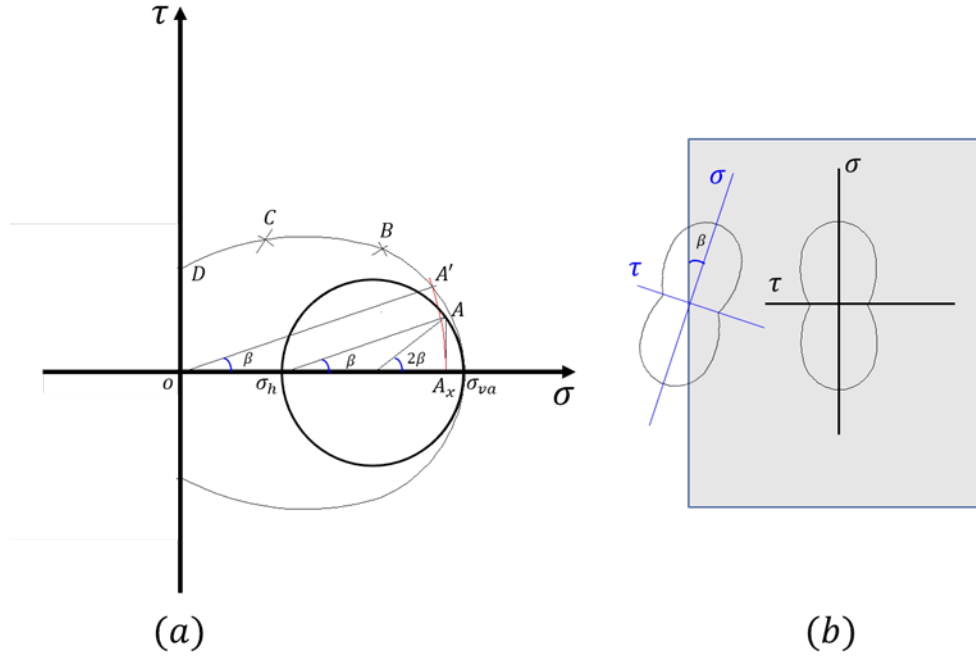
Figure 5-8: Mohr's circle stress diagram in (a) Cartesian and polar coordinates, and (b) rotated to the principal coordinates of the system.

Description as a Mohr's circle is not intuitive in understanding the stress rotation. Rather, Figure 5-5 (a) shows the advantages of using a polar coordinate system. For example, if we quantify the normal and shear stresses of plane "A" in the Mohr's circle plot, this represents the plane at an angle β to the maximum principal normal stress direction. In the Mohr's diagram, the deflection angle of this plane is 2β in the Cartesian coordinate system as shown in the Figure 5-8. But in the polar coordinate system, the angle between plane "A" and the plane of the maximum principal normal stress is shown directly as the angle β. In the polar coordinate system, the deflection angle of the maximum principal normal stress at the boundary of the loosely compacted Zone B, relative to the vertical direction, is as shown in Figure 5-8 (b). In Figure 5-8 (b), the fragmented rock medium is assumed a porous continuum and the maximum principal normal stress in the center of the caved zone (fully compacted Zone A) is vertical. At the boundary of the caved zone (loosely compacted Zone B), the maximum principal normal stress rotates towards the vertical direction by an angle β. The rib-induced shear resistance requires that the state of the stress for the immediate gob near the rib (Zone B) should be re-analyzed. As quantified in Figure 5-8(b), the maximum principal normal stress in the center of the caved gob remains vertical with its direction unaffected by the shear stress in the vertical direction. In this study, a representative element volume (REV) is represented by the gob region near the rib (Zone B) and the rotated maximum/minimum principal stresses are regarded as uniform normal stresses applied over the full REV. If the friction force is ignored and the vertical

and horizontal stresses are uniformly distributed, the Mohr's circle for the representative element volume (REV) is as shown by the dashed Mohr's diagram (Figure 5-9). Here, the Mohr-Coulomb failure criterion is adopted to evaluate the failure state of the rock mass, which can be expressed as:

$$\tau = \mu\sigma + C_0 \tag{12}$$

where τ is the shear stress, MPa; σ is the normal stress, MPa; C_0 is the cohesion, MPa; μ is the friction coefficient, where $\mu = \tan\varphi$, dimensionless; and φ is the angle of internal friction, degrees.

Since the fragmented rock mass is stacked layer by layer, the rock blocks in the roof fail as the overburden stress increase to its maximum value. We analyze this failure limit - the principal stresses approach this limit as the shear stress reaches the failure envelope. In Figure 5-9 (a), the vertical stress, absent the effect of friction, is shown as σ_v. This is the maximum principal normal stress with the horizontal stress - that is also the minimum principal stress - is shown as σ_h (Figure 5-9 (c)). If the friction force is considered - as shown in Figure 5-7 - the plane with the horizontal stress (σ_h) has a shear stress (τ_N) that is perpendicular to the horizontal stress due to the confinement. The rotated Mohr's circle, including the friction force, will pass through location M with coordinates ($\sigma_h, f\sigma_h$), while the shear stress τ_N can be calculated from $f\sigma_h$ based on Amonton's law (Figure 5-9 (b)). The new Mohr's circle will have a revised radius determined by recalling the relationship between the new Mohr's circle and the Mohr-Coulomb failure criterion. Since the fragmented rock blocks are at failure, the radius of the new Mohr's circle may be determined from:

$$\begin{cases} \tau_N = \mu\sigma_N + C_0 \\ \dfrac{\tau_N}{\sigma_N - a} = -\dfrac{1}{\mu} \\ (\sigma_h - a)^2 + (f\sigma_h)^2 = (\sigma_N - a)^2 + \tau_N{}^2 \end{cases} \tag{13}$$

where the location with coordinates (σ_N, τ_N) is the tangent between the new Mohr's circle and the Mohr-Coulomb failure envelope (point N in Figure 5-9). Point o' has coordinates ($a,0$) and the second equation of Eq. (13) describes the relationship between the tangent (failure envelope) to the Mohr's circle and its radius ($o' - N$).

Based on Eq. (13), the unknow parameter a can be determined as:

$$a = \sigma_h + \mu^2\sigma_h + C_0\mu + \sqrt{\mu^2\sigma_h{}^2 + \mu^4\sigma_h{}^2 + C_0{}^2\mu^2 + 2C_0\mu\sigma_h + 2C_0\mu^3\sigma_h - f^2\sigma_h{}^2 - f^2\mu^2\sigma_h{}^2 + C_0{}^2} \,. \tag{14}$$

Based on the geometry, the radius of the new Mohr's circle (r') can be expressed as:

$$\frac{r'}{\sin\varphi} = a + C_0\cot\varphi. \tag{15}$$

From Eq. (14), the geometric relationship, the maximum principal normal stress in the new Mohr's circle can be expressed as:

$$\sigma_v' = (1 + \sin\varphi)\left(\sigma_h + \mu^2\sigma_h + C_0\mu + \sqrt{\mu^2\sigma_h{}^2 + \mu^4\sigma_h{}^2 + C_0{}^2\mu^2 + 2C_0\mu\sigma_h + 2C_0\mu^3\sigma_h - f^2\sigma_h{}^2 - f^2\mu^2\sigma_h{}^2 + C_0{}^2}\right) + C_0\cos\varphi. \tag{16}$$

Eq. (16) defines the maximum principal normal stress in loosely compacted Zone B by considering the rib resistance. From the new Mohr's circle, the minimum principal normal stress (σ_h') can be calculated as:

$$\sigma_h' = (1 - sin\varphi)\left(\sigma_h + \mu^2\sigma_h + C_0\mu + \sqrt{\mu^2\sigma_h^2 + \mu^4\sigma_h^2 + C_0^2\mu^2 + 2C_0\mu\sigma_h + 2C_0\mu^3\sigma_h - f^2\sigma_h^2 - f^2\mu^2\sigma_h^2 + C_0^2}\right) - C_0cos\varphi. \quad (17)$$

In addition, the plane "M" in the newly formed Mohr's circle defines the redistributed horizontal stress and the associated shear stress along the rib. The horizontal and vertical principal normal stresses must be orthogonal and are therefore defined as in Figure 5-8(a). The redistributed vertical stress along the boundary can be calculated from point "M'" in the new Mohr's circle (Figure 5-9).

Figure 5-9: Rotated Mohr's circle stress diagrams in Cartesian coordinates.

5.1.3.2 Porosity and permeability evolution in the gob

The porosity of the porous medium forming the gob is important in controlling permeability. However, direct measurement of the porosity is difficult, due to its inaccessibility. The porosity

of the stacked rock mass will vary with the shapes and size distribution of the fragmented rock blocks. In light of the disordered nature of the fragmented blocks/particles, several successful attempts have been made to characterize soil particle-and aggregate-size distributions by invoking the concept of fractal dimension [45,46]. The fractal dimension links the number-size of fragmented particles, as [47]:

$$N(\omega > \eta) = B_F \eta^{-D_F} \tag{18}$$

where, N is the cumulative number of particles of size ω greater than a characteristic size η, dimensionless; the exponent D_F is the fragmentation fractal dimension; and B_F is a coefficient related to the number of particles of unit diameter, dimensionless.

Fractal theory has also been adopted to characterize the characteristics of the fragmented rock medium in the gob. Typically, the fractal porosity in terms of particle size is given as [19]:

$$\phi = 1 - (\frac{\eta_{min}}{\eta_{max}})^{3-D_F} \tag{19}$$

where, ϕ is the porosity, dimensionless; η_{min} and η_{max} are the minimum and maximum rock block sizes, respectively, m. Based on Eq (19). the initial porosity of the porous medium can be estimated by characterizing the rock sizes and their distribution.

For the fragmented rock mass in the caved gob, the compaction process is uniaxial and thus the associated porosity evolves as a unique function of the variable loading stress in vertical direction. Normally, the porosity of the porous medium can be defined as [48–50]:

$$\phi = \frac{V_p}{V_b} \tag{20}$$

where, V_p is the void volume, m³; and V_b is the total volume of the porous medium, m³.

Based on Eq. (20), the evolution of porosity with uniaxial compaction can be expressed as:

$$\phi = \frac{V_b - V_s}{V_b} = 1 - \frac{V_s}{V_{b0}(1-\varepsilon_v)} = 1 - \frac{V_{s0}}{V_{b0}(1-\varepsilon_v)} = 1 - (1-\phi_0)\frac{1}{(1-\varepsilon_v)} \tag{21}$$

where, V_{b0} is the total volume of the porous medium at an initial time, m³. Implicit in Eq. (21) is that there is no variation in the solid volume based on an assumed constant rock-medium density. In the caved zone, the initial high void ratio created by the fragmented rocks evolves with time due to the successive compaction of the overburden. With vertical compaction, the broken gob stiffens due to particle rearrangement, slip and crushing of the fragmented components in the limited caved zone. A reduction in the effective void ratio restricts the fluid pathways to airflow and limits the concurrent migration of methane.

A model quantifying the volumetric strain of the fragmented rock medium is [1]:

$$\varepsilon_v = \frac{2\lambda+1}{E_z} \sigma_v \tag{22}$$

where, λ is the confining coefficient representing the intensity of the induced horizontal stress due to overburden compaction, $\lambda = \frac{\sigma_h}{\sigma_v}$, dimensionless; E_z is the uniaxial elastic modulus, MPa.

In the rotated principal coordinate system, the confining coefficient (λ) may be expressed as $\lambda' = \frac{\sigma_h'}{\sigma_v}$, which can be further developed from Eqs. (16) and (17) as:

$$\lambda' = \frac{(1-sin\varphi)\left(\sigma_h + \mu^2\sigma_h + C_0\mu + \sqrt{\mu^2\sigma_h^2 + \mu^4\sigma_h^2 + C_0^2\mu^2 + 2C_0\mu\sigma_h + 2C_0\mu^3\sigma_h - f^2\sigma_h^2 - f^2\mu^2\sigma_h^2 + C_0^2}\right) - C_0 cos\varphi}{(1+sin\varphi)\left(\sigma_h + \mu^2\sigma_h + C_0\mu + \sqrt{\mu^2\sigma_h^2 + \mu^4\sigma_h^2 + C_0^2\mu^2 + 2C_0\mu\sigma_h + 2C_0\mu^3\sigma_h - f^2\sigma_h^2\left(\frac{x}{b}\right)^2 - f^2\mu^2\sigma_h^2\left(\frac{x}{b}\right)^2 + C_0^2}\right) + C_0 cos\varphi}. \tag{23}$$

In addition, the uniaxial elastic modulus E_z is described as [1]:

$$E_z = E(1 + 2\lambda') \tag{24}$$

where E is the secant modulus, MPa.

By introducing Eqs. (23), (24) into Eq. (22), and then substituting into Eq. (21), the evolving porosity with the increasing vertical stress can be expressed as:

$$\phi = 1 - \frac{1-\phi_0}{1 - \frac{(3-sin\varphi)\left(\sigma_h + \mu^2\sigma_h + C_0\mu + \sqrt{\mu^2\sigma_h^2 + \mu^4\sigma_h^2 + C_0^2\mu^2 + 2C_0\mu\sigma_h + 2C_0\mu^3\sigma_h - f^2\sigma_h^2 - f^2\mu^2\sigma_h^2 + C_0^2}\right) - C_0 cos\varphi}{E(1+2\lambda')}} \tag{25}$$

The fragmented roof blocks collapse into the caved zone and create viable pathways for airflow and the concurrent migration of methane. The permeability of the zone is related to the size distribution of the fragmented roof blocks - the porosity and the associated permeability are typically used to define the permeability of the gob region. Permeability may be defined through the Carman-Kozeny equation for fluid flow in aggregates that:

$$k = \frac{D^2}{180}\frac{\phi^3}{(1-\phi)^2} \tag{26}$$

where, k is the permeability of the packed bed at a specified state, m²; D is the characteristic size of the aggregate particles, m; and ϕ is the porosity of the porous medium, dimensionless. An equivalent diameter, D, may be defined for a series of particles with irregular shapes – commonly by taking the average of the maximum and minimum particle sizes. However, this may significantly overestimate permeability [19].

Based on Eq. (18), the total number of the particles in the size range η_{min} to η_{max} in the packed bed can be estimated as:

$$N_{total}(\omega > \eta_{min}) = B_F\eta_{min}^{-D_F} \tag{27}$$

where, η_{min} and η_{max} are the sizes of the smallest and largest particles, respectively, m. Differentiating Eq. (18) and then dividing by Eq. (27), defines the probability density function of the particle size distribution as:

$$\frac{dN}{N_t} = -\frac{D_F\eta^{-D_F-1}}{\eta_{min}^{-D_F}}d\eta \tag{28}$$

Enabling a characteristic particle size to be defined, based on the probability density function as:

$$\widetilde{D} = -\int_{\eta_{min}}^{\eta_{max}}\frac{-D_F\eta^{-D_F-1}}{\eta_{min}^{-D_F}}\eta d\eta = -\frac{D_F\eta_{max}}{(D_F-1)}\left(\frac{\eta_{max}}{\eta_{min}}\right)^{-D_F} + \frac{D_F\eta_{min}}{(D_F-1)} \tag{29}$$

By replacing the characteristic size of the aggregate particles and porosity in Eq. (26) by Eqs. (29) and Eq. (25), gives:

$$k = \frac{\left[-\frac{D_F \eta_{max}}{(D_F-1)}\left(\frac{\eta_{max}}{\eta_{min}}\right)^{-D_F} + \frac{D_F \eta_{min}}{(D_F-1)}\right]^2}{180} \cdot \frac{\left[1-\dfrac{1-\phi_0}{1-\dfrac{(3-sin\varphi)\left(\sigma_h+\mu^2\sigma_h+C_0\mu+\sqrt{\mu^2\sigma_h^2+\mu^4\sigma_h^2+C_0^2\mu^2+2C_0\mu\sigma_h+2C_0\mu^3\sigma_h-f^2\sigma_h^2-f^2\mu^2\sigma_h^2+C_0^2}\right)-C_0cos\varphi}{E(1+2\lambda')}}\right]^3}{\left[1-\dfrac{1-\phi_0}{1-\dfrac{(3-sin\varphi)\left(\sigma_h+\mu^2\sigma_h+C_0\mu+\sqrt{\mu^2\sigma_h^2+\mu^4\sigma_h^2+C_0^2\mu^2+2C_0\mu\sigma_h+2C_0\mu^3\sigma_h-f^2\sigma_h^2-f^2\mu^2\sigma_h^2+C_0^2}\right)-C_0cos\varphi}{E(1+2\lambda')}}\right]^2} \quad (30)$$

Eq. (30) gives the permeability of the fragmented rock medium as a result of successive compaction. It is apparent that Eq. (30) can be used to define the permeability evolution of the loosely packed gob region (Figure 5-1 (c)) incorporating the effect of stress rotation due to the rib resistance. Also, Eq. (30) can be simplified to describe the permeability evolution in the fully compacted Zone A (Figure 5-1(c)) by neglecting the effects of shear resistance. This model provides an essential link between permeabilities measured at lab-scale and application to field scale response.

5.1.4 Results and analyses for gob rock compaction and permeability evolutions

Uniaxial compaction experiments are conducted in this study to augment previous studies [41]. Porosity and permeability evolve with compaction, as quantified in Eqs. (25) and (30). The uniaxial elastic modulus E is a measure of the secant modulus of the fragmented rock medium. Uniaxial compression data are already available for shale, weak sandstone and strong sandstone [41]. These results show that the secant modulus of the fragmented rock medium is linear with the uniaxial loading stress, which can be expressed as:

$$E = (\alpha_{\sigma_z} + b) \quad (31)$$

where, a and b are linear fitting parameters.

The secant moduli ($E = \frac{\sigma_z}{\varepsilon_z}$) of the fragmented rock medium are calculated from the nonlinear stress-strain curve of Figure 5-10. The nonlinear stress-strain curve shows an initial highly-compactive stage, attributed to the highly void ratio of the packed zone. With further compaction, the fragment pack stiffens and deformation becomes linear in stress. The fitted values of a and b are then used to calculate the uniaxial elastic modulus based on Eqs. (24) and (60).

Figure 5-11 shows comparisons between the modeled and experimental results for porosity evolution. Porosity evolves non-linearly with an increase in stress with good agreement

between experimental and modeled data. The modelled porosities show an obvious deviation from the experimental results only at low stresses – due to the assumption of a linear response in stress-strain (Figure 5-6(a)). The fragmented rock blocks in the sample chamber are loosely packed as illustrated in Figure 5-5. The loosely packed rock blocks fully compact and transition to elastic response under elevated stresses, as shown in Figure 5-11. An approximately eleven-fold increase in stress (~1.70 MPa to ~18.68 MPa) results in a nonlinear decrease in porosity of ~63% (from 0.533 to 0.198) for Shale Test A, ~73% (from 0.369 to 0.099) for Shale Test B, ~ 62% (from 0.509 to 0.195) for Sandstone Test C, and ~56% (from 0.439 to 0.194) for Sandstone Test D.
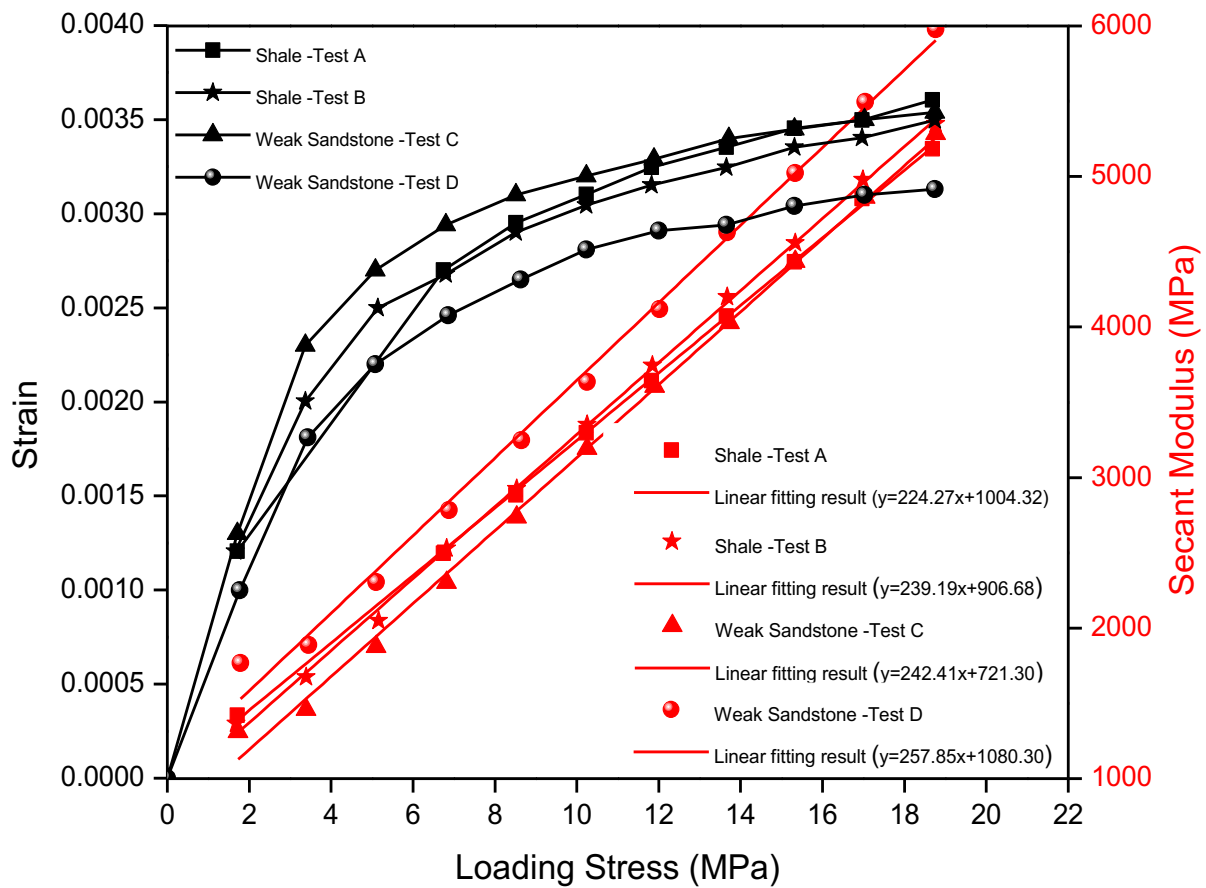
Figure 5-10: Stress-strain response and secant modulus for broken rock blocks under successive compaction. (data adapted from Pappas and Mark (1993) [28]).
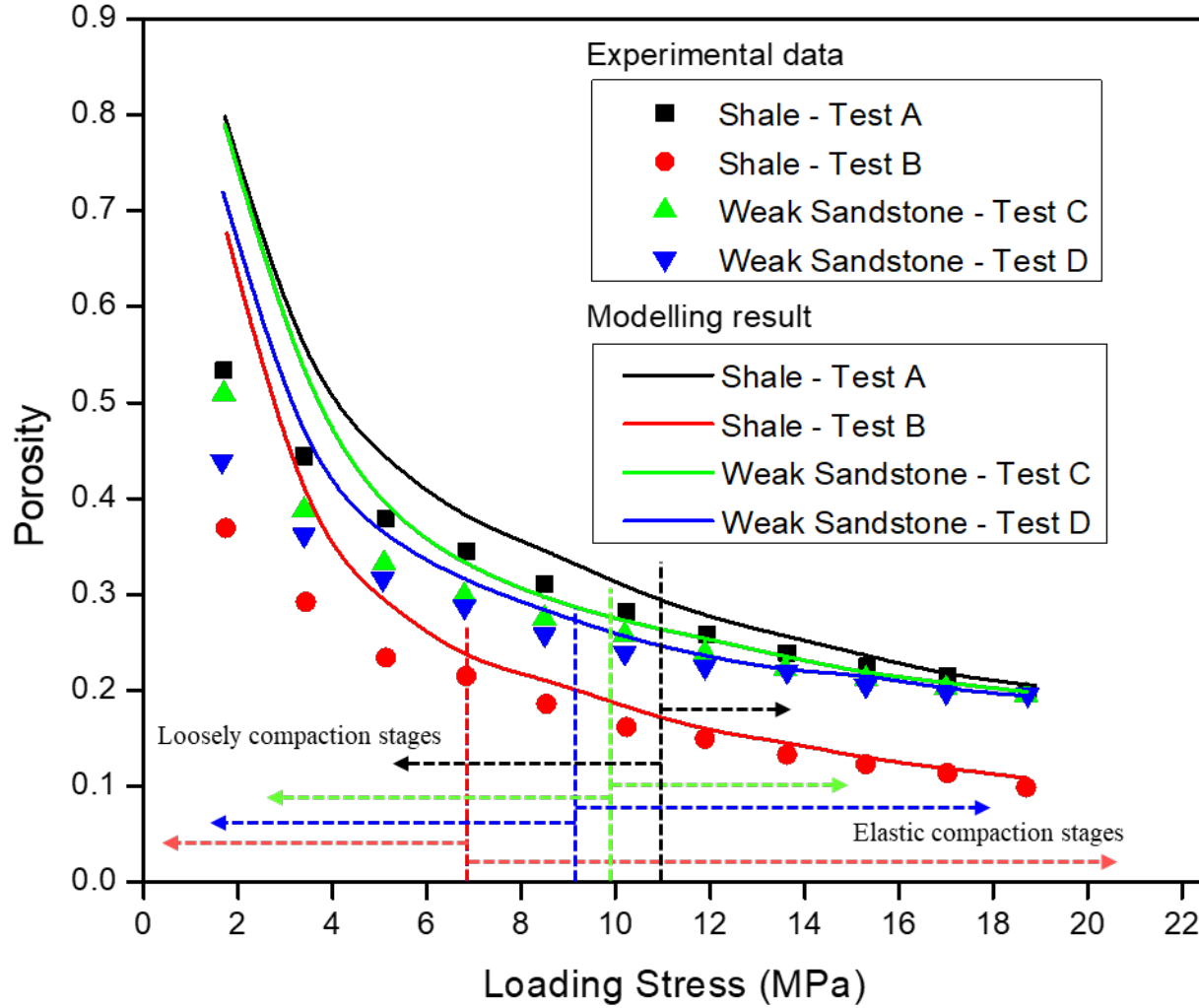
Figure 5-11: Comparisons of experimental and modelled porosities. (data adapted from Pappas and Mark (1993) [41]).

Predictions of permeability evolution have been largely from changes in porosity with magnitudes evolving from 0.026 cm² to 0.074 cm² for a gob initially composed of larger rocks and from 0.009 cm² to 0.026cm² for smaller rock blocks [19]. As proposed in Eq. (26), the permeability of the fragmented rock medium is linked to porosity through the Carman - Kozeny relation. As quantified in the Carman-Kozeny equation, the particle size distribution (characteristic size) of the fragmented rock and the porosity are the only two parameters that determine the associated permeability evolution. Previous studies have estimated the dimension of the broken rock blocks by taking the average of the maximum and minimum dimensions of the aggregates [19]. We recover the true average dimension directly from the probability density function of the particle size distribution. Figure 5-12(a) shows permeabilities of the compacted rock blocks predicted from this model and compares them with previous modeling studies [19]. The predicted permeability model is fractal and captures the irregular shapes of the different flow channels including circular, triangular and elliptical

34

sections. Figure 5-12(a) shows the predicted permeabilities of previous studies [19], assuming that flow channels are elliptical in section. The permeability-stress curves divide naturally into two segments – representing the nonlinear initial stage and the linear later (high stress) stage (Figure 5-12(a)). For elliptical flow channels, as the loading stress increases from 0 to 18.68 MPa the predicted absolute permeabilities for the of shale Test A and the weak sandstone of Test C decrease from 0.0017 cm² to 7.4×10⁻⁴ cm² – an eleven-fold decrease. Similarly, the predicted permeabilities for the shale of Test B and the weak sandstone of Test D decrease from 0.0037 cm² and 0.0017 cm² respectively [19]. Based on the proposed permeability model, the predicted permeabilities for Tests A-D decrease, respectively, from 0.0031 cm² to 4.18×10⁻⁵ cm² (Test A), from 0.0215 cm² to 4.98×10⁻⁴ cm² (B), from 0.0066 cm² to 2.87×10⁻⁴ cm² (C), and from 0.011 cm² to 4.58×10⁻⁴ cm² (D) as the loading stress increases from 3.40 to 18.68 MPa. At low stresses and under loose compaction, the predicted results in our study are distinctly higher than those of previous modeling studies [19]. After initial compaction, the newly-compacted rock mass behaves elastically and both models predict permeabilities to the same order of magnitude. As illustrated in Figure 5-6, the excessive compaction at low stress suggests that initial permeabilities should indeed be high – as implicitly defined for this proposed model in this study. This nonlinear early response is not incorporated in previous permeability models [19], resulting in this mismatch. Prior models mainly consider the size distribution of the broken rock mass, which explains the negligible differences between the predicted permeabilities between the test groups (i.e. tests A and C, tests B and D) even though these groups were packed with different types of fragmented rock. Typically, the dimensions of the maximum and minimum particles in tests A and C are the same but the rock aggregates in tests A and C exhibit different elastic properties – thus, the apparent volumetric responses exhibit clear differences (Figure 5-10). The proposed model in this study accurately predicted the differences of the permeabilities among the test groups for the four rock mass types based on Eq. (30).

The effects of the average dimensions of the particles on permeability predictions are compared in Figure 5-12(b). The average particle dimensions were taken from the mean value of the maximum and minimum particle sizes ($\bar{D} = \frac{\eta_{max}+\eta_{min}}{2}$) as well as estimated from the probability density function (PDF) of the fractal particle size distribution ($\widetilde{D}$ in Eq. (29)). As shown in Figure 5-12(b), if the average dimensions of the particles are calculated from the maximum and minimum particle sizes, alone, the predicted permeabilities are distinctly higher than those recovered using the PDF. The results illustrate that the form of the size distribution of the particles, and the associated flow architecture, significantly influences the permeability evolution, as confirmed in the experimental observations of Figure 5-5.
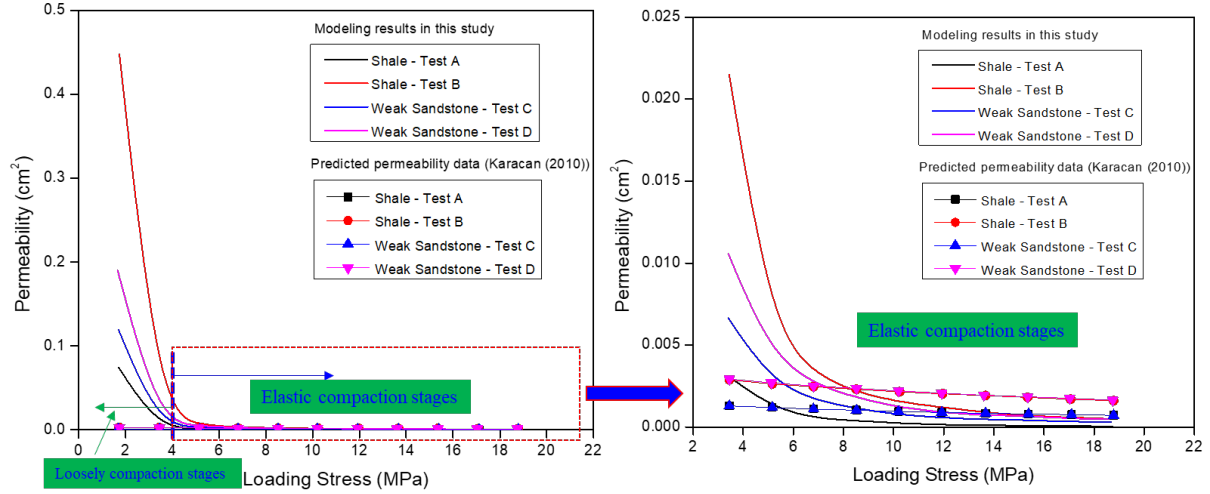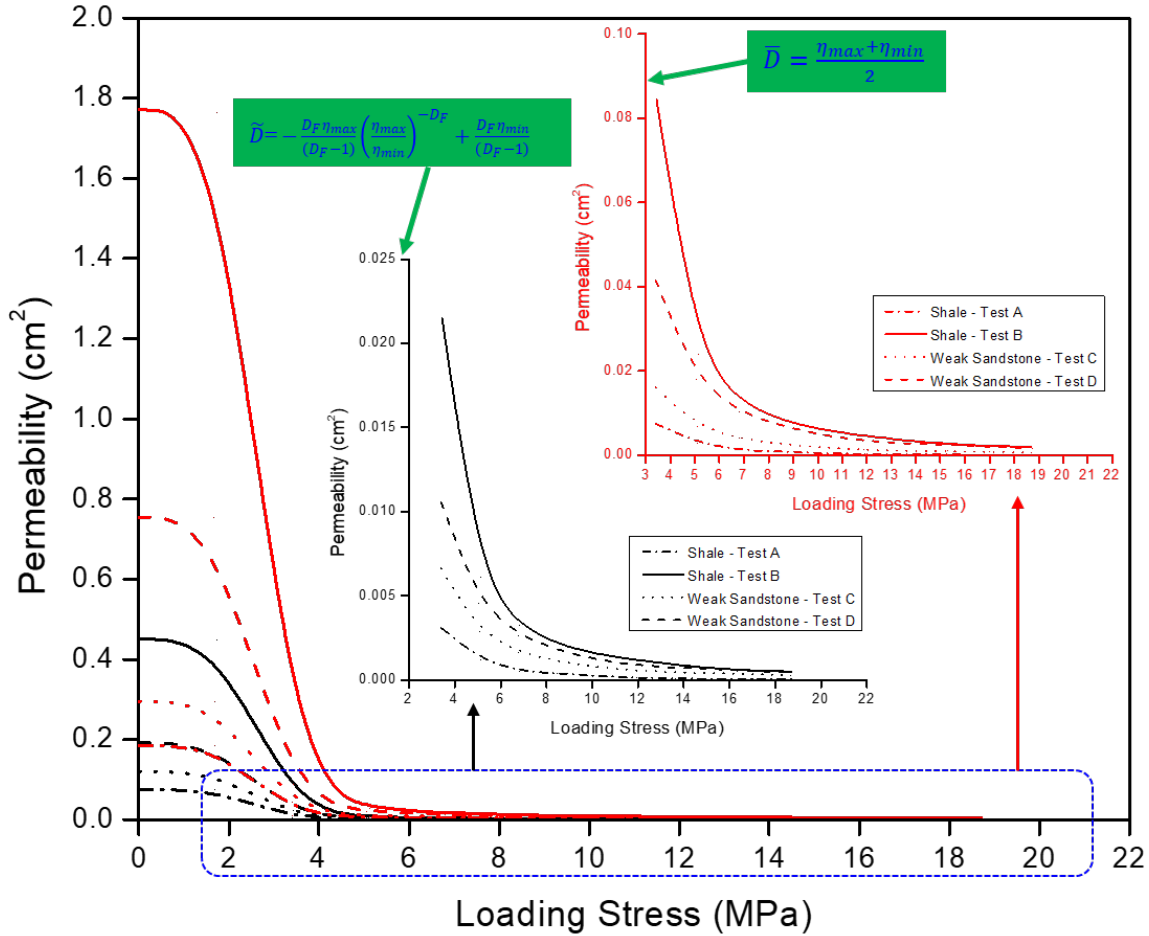
Figure 5-12: Comparisons of experimental observations with modelled permeabilities. (raw data adapted from Pappas and Mark (1993)[41]).

5.1.5 Discussion and improved understanding of the gob compaction

The longwall panel is typically very wide for its productivity, the rib resistance and support effects at the boundary near the rib area will not influence the stress distribution in the middle of the gob region based on the classical Saint-Venant's principle, as illustrated in Figure 5-13 (a). In Figure 5-13, the vertical stress in the middle region of the gob flats out after a certain distance. For our study, we assume the location of gob at three times of the caved zone thickness (h) will reach its maximum based on the Saint -Venant's principle. However, the stress in the loosely compacted area near the fully compacted gob zone will be influenced by the shear stress. The modified vertical stress model demonstrates that the vertical stress in the caved zone varies with locations, as shown in Figure 5-13(b). Specifically, the average vertical stress in the center of the caved zone is maximum and the minimum vertical stress is expected near the rib area.
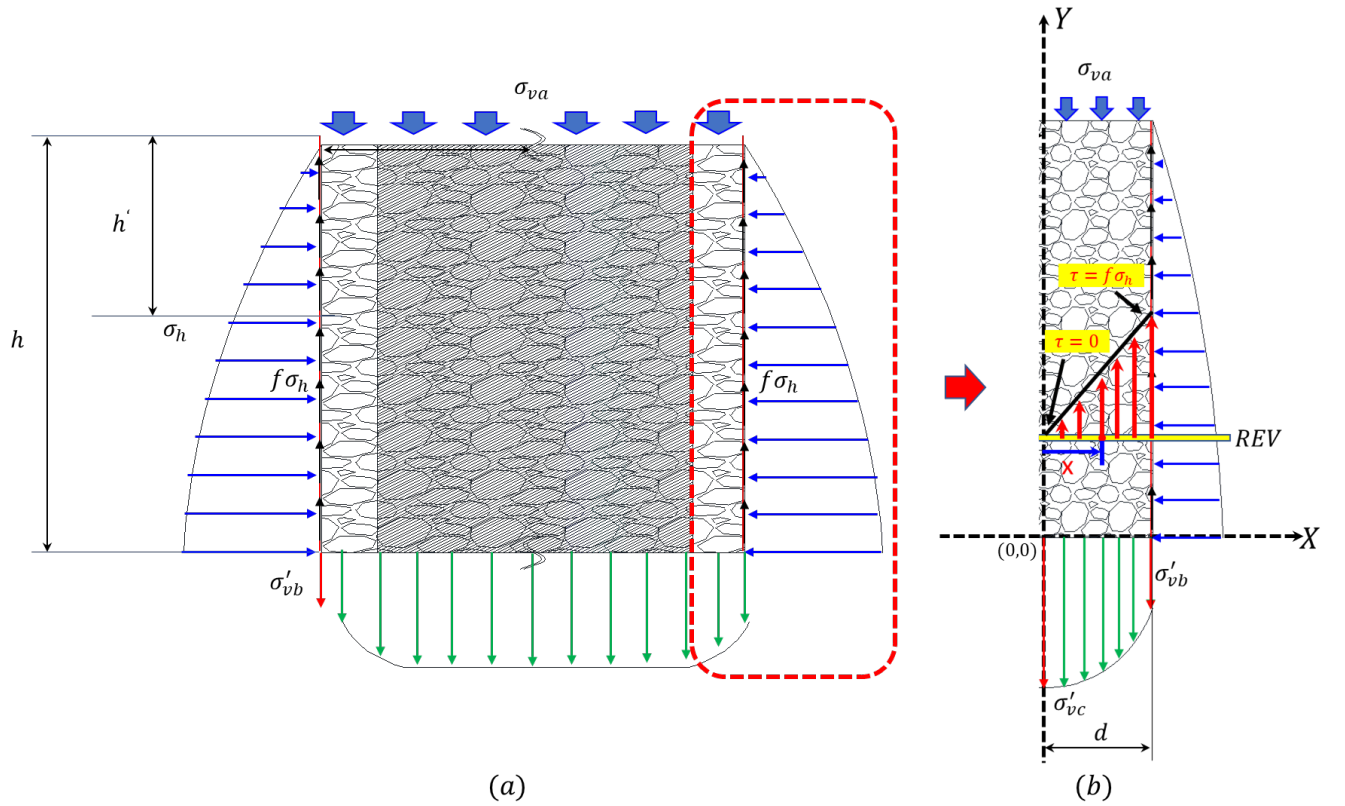
Figure 5-13: Schematic of nonuniform distributions of vertical stress in the caved zone.

In Section 4.1, the rotation of the coordinate system representing the principal stresses, as induced by rib resistance, was modeled as shown in Figure 5-9. However, it should be noted that the derivations assume that the gob material is subject to uniform stresses – represented as average vertical and horizontal stresses. From the rotated Mohr's circle (Figure 5-9(a)), the modified vertical stress can be calculated from Figure 5-9 as:

$$\sigma_v = 2*a - \sigma_h = 2\left(\sigma_h + \mu^2\sigma_h + C_0\mu + \sqrt{\mu^2\sigma_h{}^2 + \mu^4\sigma_h{}^2 + C_0{}^2\mu^2 + 2C_0\mu\sigma_h + 2C_0\mu^3\sigma_h - f^2\sigma_h{}^2 - f^2\mu^2\sigma_h{}^2 + C_0{}^2}\right) - \sigma_h \quad (32)$$

Eq. (63) defines the vertical stress acting on the loosely compacted gob adjacent to the rib. Thus, the vertical stress in the near-rib region will be less than in the center, as a consequence of rib resistance and support. To capture the nonuniform distribution of the vertical stress in the caved zone (Figure 5-13(b)), we first assume no vertical displacement in the compacted gob at the center line of the caved zone - illustrated as the Y-axis. Due to this symmetry, no shear stress will be induced on the vertical plane of the gob centerline. If there is no shear stress on the centerline, the shear stress at any given vertical plane from the center line to the gob boundary can be defined as:

$$\tau = \frac{f\sigma_h}{d}x \tag{33}$$

where τ is the shear stress on a given vertical plane at a distance x from the centerline; x is the distance between the centerline and the given plane; and d is the half width of the caved zone.

From Eq. (64), we can define the friction coefficient at given vertical plane as:

$$f' = \frac{\tau}{\sigma_h} = f\frac{x}{d} \tag{34}$$

where f' is the friction coefficient on a given plane at a distance x away from the centerline of the gob.

By replacing the boundary friction coefficient f in Eq. (63) as f', the vertical stress at different locations can be expressed as:

$$\sigma_v = 2\left(\sigma_h + \mu^2\sigma_h + C_0\mu + \sqrt{\mu^2\sigma_h^2 + \mu^4\sigma_h^2 + C_0^2\mu^2 + 2C_0\mu\sigma_h + 2C_0\mu^3\sigma_h - f^2\sigma_h^2\left(\frac{x}{d}\right)^2 - f^2\mu^2\sigma_h^2\left(\frac{x}{d}\right)^2 + C_0^2}\right) - \sigma_h \tag{34}$$

where Eq. (66) defines the vertical stress at different locations in the caved zone. The modified vertical stress model demonstrates that the vertical stress in the caved zone varies with location, as shown in Figure 5-13. From this model for vertical stress, an increase of friction coefficient results in a corresponding decrease in vertical stress.

5.2 Predicting gob gas emissions from gob-to-face in longwall coal mines: coupled analytical and numerical modeling
5.2.1 Introduction and Background

Longwall top-coal caving (LTCC) is a highly efficient and economically favorable mining method for thick and ultra-thick coal seams [51-53]. This highly productive technique is believed to be rooted from the original method of soutirage mining developed in France during the 1960s [54]. Following the success of the first LTCC mining panel at the Puhe coal mine in Shenyang in 1984 [55], the LTCC mining method has been broadly deployed for the recovery of thick coal seams. With continuous improvement and modifications, LTCC mining is currently the preferred method for the mining of deep and thick coal seams in China [53]. As shown in Figure 5-14, the current LTCC method exerts its unique advantages by dividing the thick or ultra-thick coal seam

into two seam-parallel slices, comprising lower and upper sub-layers [56–58]. The lower sub-layer is mechanically cut by the longwall shearer liberating the upper sub-layer to collapse under the combined impact of gravity and overburden pressure. Two conveyors simultaneous collect the broken coal as shown in Figure 5-14. In a typical longwall system, the conveyor beneath the shields is used to collect the coal cut by the longwall shearer. Unique to LTCC, is the provision of a behind-shield rear conveyor that continuously transports coal from the top-caving layer [53,59,60]. The LTCC panel advances incrementally as the coal is continuously extracted [1]. The unsupported coal roof behind the hydraulic shields may hang for some time before caving and breaking into caved coal blocks. The large blocks fall into the caved zone and create viable pathways for airflow and the concurrent migration of methane. The caved zone (or "gob") may reach ~4-to-11 times the thickness of the coal seam height where overburden rocks are weak and porous [1,19].
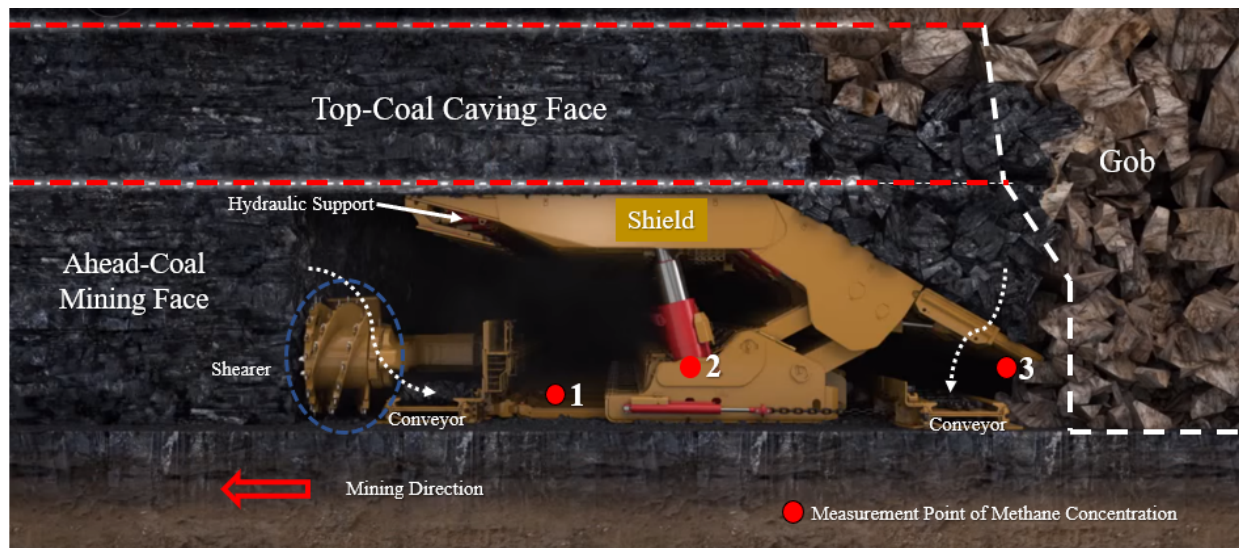
Figure 5-14: Schematic of the LTCC mining method (adapted from Caterpillar Global Mining – CAT publication)

Despite its efficiency and economic favorability, LTCC mining also presents the potential to increase the accumulation of methane at or near the active working face as a consequence of high methane emissions from the gob. The interface between the longwall face and the gob is particularly vulnerable to such accumulations of methane [6,10,61]. Unfortunately, a series of methane-related incidents have originated from accumulations at or near this interface where accidental ignition has occurred. For example, the occurrences of methane ignitions at the Upper Big Branch South Mine in 1997 and 2010 led to disastrous results, the latter resulting in a massive mine-wide explosion [62].

The provision of an effective ventilation system is necessary to mitigate the gas hazard at the longwall face. A key component is in providing fresh air to miners as well as diluting methane to a safe threshold value below the ignition/explosive limit [63,64]. Previous studies have

demonstrated that multiple factors affect the effectiveness of the ventilation system, including the geometry of the ventilation network, airway resistance, airway temperature, operating characteristic of fans together with other features [65–67]. More importantly, excess and unpredicted methane emissions may disturb the ventilation system and present an unexpected hazard to the face with impact on other related ventilation branches [19,68]. LTCC mining is particularly vulnerable in this regard as the methane emissions can be excessive – the method intrinsically creates a huge and irregular caved void behind the shied which is directly connected to the face. Thus, the monitoring and prediction of gas emission patterns and their dilution at face and in the gob region are crucial to allow safe mining. However, it is also technically challenging due to the complexity of the gas emission and transport behavior in the heterogeneous gob materials which provides an uncertain methane source term.

This project documents a mine-wide ventilation pressure and flow rate survey (*p-Q* survey) to establish a ventilation network model – including methane gas concentrations recorded at selected face locations. We develop a numerical gas emission model specifically to dynamically evaluate methane production and transport from the compacted gob and its impact on the longwall face. The numerical model is validated using the mine-wide field methane monitoring results. We use this model to evaluate gas emission intensity from the gob and its interaction with ventilation systems. The validated model is then used as mechanism-based model to investigate the interactions between gob gas emission and the mine ventilation system.

Gas emission rate from the gob is closely related to the caving characteristics of the caved rock mass, block size, compaction behavior and evolving porosity and permeability [19,69]. Typically, these characteristics determine the gob gas emission behavior and ultimately influence the ventilation design and effectiveness at the longwall working face [1]. Despite the importance of these characteristics, direct field measurements of porosity and permeability are rare, due to the extremely challenging environment [19]. Thus, many previous studies have attempted theoretical predictions of porosity and permeability which have then been calibrated against field measurements and laboratory data [19,69–72].

Laboratory tests on rock materials, with approximate particle size gradations of the actual gob material from headgate entries in Eastern Kentucky coal mines, have been used to determine the mechanical properties of the gob for numerical models [41]. Such models have been extended to define the porosity and permeability of the broken rock material within the gob [19]. This approach was inspired by the imaging analyses of gob materials to represent the response of a completely fragmented porous medium and constrained relative to observed vertical strains [73]. Some models have used Carman-Kozeny relations to define permeability in the vertical direction [74] with conceptual models of broken rock mass compaction based on the constitutive laws of the broken rock mass [1].

Based on the previous modelling work, a quantitative gas flow model is evidently still lacking – specifically one that can quantify the gas emission rate from the gob towards the face and its adjacent regions including the bleeder system. The pressure gradients driving gas flow in the compacted gob can be directly used to predict gas emission rates under various conditions. The widely used pressure equation for packed beds [75] accommodates both viscous and kinetic energy losses primarily in laminar and turbulent flows, respectively [76–78]. The two principal constants in Ergun's equation were actively discussed and subsequently modified by Hicks (1970) by replacing the two constants with the Reynolds number [79]. Potentially difficult to apply to heterogenous irregularly packed beds accommodations for the impacts of contracting-expanding channels [80] have ameliorated these difficulties, including the accommodation of viscous and kinetic energy losses [27].

To summarize, the aforementioned studies established a spectrum of models and methods to accommodate flow and transport in packed beds. However, compacting coal mine gobs are a particularly unique packed bed undergoing dynamic compaction and with an unusually irregular size and shape distribution of rock-coal blocks. Needed is a mechanism-based flow model with physically meaningful parameters that may be validated to predict gas emissions from gob. We introduce and validate a gas flow behavior is modelled and gob gas emission rate is defined and quantified by numerical simulation. This coupled analytical and numerical modeling framework provides a pathway to quantify the gas emission rate from the compacted gob within the mine while correctly considering the detailed component material properties of the gob.

5.2.2 Mine site description for the field monitoring

We conducted a mine-wide field monitoring program in a deep longwall mining operation. The Tangkou coal mine is located in Jining city, Shandong Province, China (Figure 5-15 (a)). The coal seams are Permian (Shanxi formation) and Carboniferous (Taiyuan formation) (Figure 5-15 (b)) comprising six mineable seams – these are seams #3, #6, #10, #15, #16 and #17 as shown in Figure 5-15 (b). Among these six minable coal seams, #3, #16 and #17 are the primary targeted seams for current mining with annual production planned at ~5 million tons/yr.

The principal coal block is largely free from large scale faulting. The #3 coal seam is being mined by the LTTC mining method. Our field survey was conducted at the 6304 working face of the #3 coal seam with the panel layout shown in Figure 5-15 (c). The average thickness of the coal seam at the 6304 working face is ~ 9.76 m and inclined at between 0~10° (average angle is ~ 4°) to the horizontal. The panel is constrained by geological to be of variable width. An initial width of 182 m transitions to a final narrow panel width of 60m with a working face length of ~1565 m. The virgin methane gas content and pressure are measured at 4.8 m³/t and 0.72 MPa,

respectively. The comprehensive mine ventilation survey and the gas concentration inventory at designated locations constrains the model development noted later in this work.
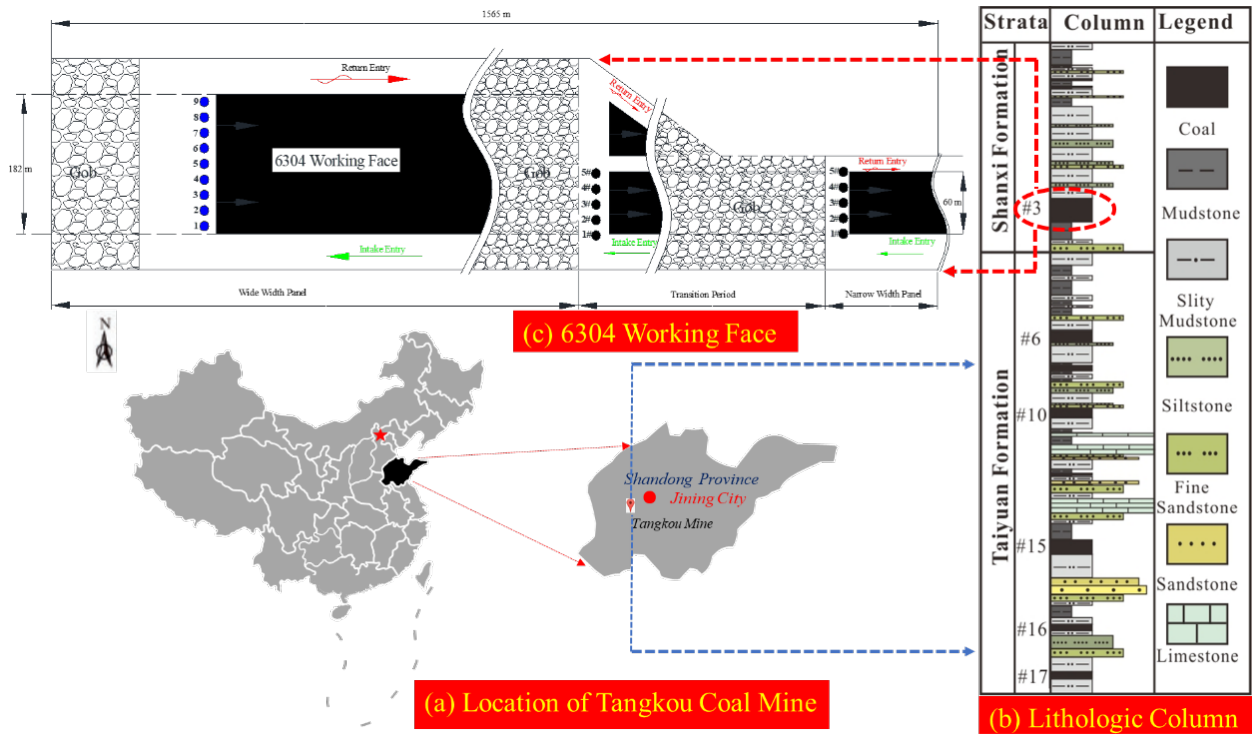
Figure 5-15: Location and schematic of the Tangkou coal mine and the 6304 working face. (a) Location of Tangkou coal mine. (b) Lithologic column. (c) 6304 working face.

5.2.3 Analytical and numerical models for determining gas flow

Compacting coal mine gobs are a unique form of packed bed undergoing dynamic compaction and with an unusually irregular size and shape distribution of rock-coal blocks. The rock-coal blocks in the caved zone create viable pathways for airflow and the concurrent migration of methane. We develop a physics-based model to accommodate gas desorption from the blocks and then transport within the voids that accommodates both viscous and inertial losses.

5.2.3.1 Conceptual physical model

In LTCC mining operations, the caved gob zone is continuously filled with the residual coal and rock blocks breaking from the roof. The gob, therefore, can be classified as a unique porous medium consisting of roof rock blocks and residual coal associated with voids. The tortuous flow channels within the voids provide channels for gas and fluid migration. The architecture and composition of the rock and coal block mixture determines the critical features of the gob, including porosity, permeability, connectivity and compactive behaviors, among others. Despite the complex characteristics of the compacted gob, a conceptual physical model must incorporate the key physical features of the assemblage – selected in 3D and 2D in Figure 5-16.

42

We assume a layered assemblage of spherical blocks (Figure 5-16 (a)), with each layer of the spheres in the x-y plane distributed center-to-center. Caved voids exist between spheres and are evenly spaced. Figure 5-16(b) shows the distribution of spheres in the y-x-z version. Similarly, each layer of the spheres in the y-x plane are distributed by point contact and different layers in z direction are interrelated. If the pressure gradient is defined from the pressure difference between the deep gob and the working face, the gas flow direction is as represented by the green arrows in Figures 5-16 (a) and (b). From Figures 5-16 (c) and (d), it is apparent that methane will pass through the irregular void channels. The radius of the spheres is represented as D with the void channel widths defined as a or b in Figures 5-16 (c). The irregular void channels also result in variable cross-sectional areas such as A1, A2 and A3 in the 3D version (A1 is equivalent to A3 in this conceptual physical model).
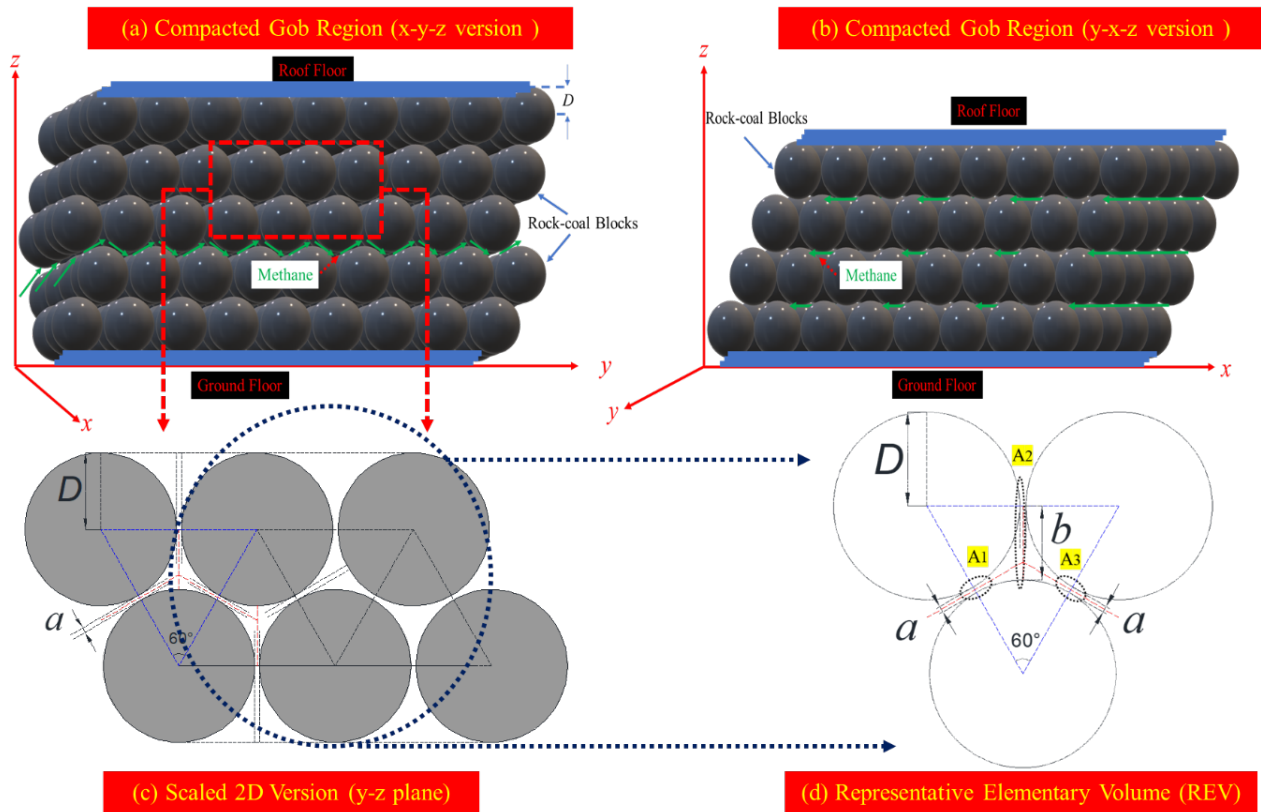
Figure 5-16: Schematic of the distribution of rock-coal blocks in the gob. (a) 3D version (x-y-z) of the compacted gob region, with x, y and z directions representing horizontal direction along the gob width, horizontal direction along with gob length and vertical direction along with gob height respectively. (b) 3D version (y-x-z) of compacted gob region. (c) Scaled 2D version in the y-z plane. (d) Representative elementary volume (REV).

Gas migrates in the direction of the pressure gradient with total energy losses comprising the sum of viscous losses and kinetic losses resulting from spatial accelerations due to changes in cross-sectional areas[50]. Other key assumptions behind the model are: 1) the dynamic process of mechanical compaction in the gob is not accommodated, that is, the caved gob region exists in its final compacted state; 2) the mixture of rock blocks and residual coal are regarded

considered as an isotropic and homogeneous porous medium – although this assumption may be relaxed; 3) methane content in the gob consists of free gas in the developed voids and adsorbed gas in the rock-coal blocks; 4) gas ad/desorption processes are isothermal; 5) effects of the deep gob region (depth over 50m) and adjacent coal seams on gob gas emissions are neglected.

5.2.3.2 Pressure gradient within the packed-bed gob

The pressure gradient in this porous packed medium can be given by the Poiseuille equation [75]:

$$\frac{dp}{dL} = \frac{32\mu\tau V_\infty}{d^2} \tag{35}$$

where, $\frac{dp}{dL}$ is the pressure gradient induced by viscous flow (Pa/m); p is the pressure (Pa); L is the length along the direction of the pressure gradient (m); d is the capillary diameter (m); μ is the dynamic viscosity (Pa·s); τ is the tortuosity (dimensionless); V_∞ is the absolute fluid velocity in the cross-section of the capillary (m/s), which scales with the apparent velocity at the cross-section of the whole cross-section, $V_\infty = \frac{V_a}{\phi}$ [81] and where ϕ is porosity (dimensionless). Therefore, Eq. (35) can be re-arranged as:

$$\frac{dp}{dL} = \frac{32\mu\tau V_a}{\phi d^2} \tag{36}$$

Based on Eq. (A-2) and Eq. (A-3) in **Appendix A**, the capillary diameter d can be represented by hydraulic diameter d_h (m), and then the pressure gradient due to the viscous energy loss becomes:

$$\frac{dp}{dL} = \frac{18\mu\tau V_a(1-\phi)^2}{\phi^3 D^2} \tag{37}$$

As illustrated in Figure 5-16, the cross-sections of gas flow channels are irregular and thereby kinetic energy loss should be taken into consideration. For uniform capillaries, the kinetic energy loss is a function of velocity with a quadratic dependancy, which can be expressed as[75]:

$$\frac{dp}{dL} = \frac{1}{2}\frac{\rho V_\infty^2}{d} \tag{38}$$

where, ρ is fluid density (kg/m³). However, the capillaries in the geometric model are irregular. Correspondingly, Zhang et al. (1999) and Wu et al., (2008) modified the kinetic energy equation as [27,82]:

$$\frac{dp}{dL} = \frac{1}{2}\xi\frac{\tau\rho V_\infty^2}{d} \tag{39}$$

where, ξ is a coefficient which may be estimated from changes in different cross-sectional areas.

ξ is a coefficient that is related to the cross-sectional areas, see Eqs. (A-9) and (A-10) in **Appendix A**. Substituting Eqs. (A-9) and (A-10) into Eq. (39) yields:

$$\frac{dp}{dL} = \frac{1}{2}\left(\xi_2 + 4{\xi_2}^2\right)\frac{\tau\rho{V_\infty}^2}{d} = \frac{3}{8}\left(\xi_2 + 4{\xi_2}^2\right)\frac{\tau\rho{V_a}^2(1-\phi)}{\phi^3 D} \tag{40}$$

Gas flow is driven by pressure gradient with the combined impact of viscous and kinetic energy losses contributing to this pressure loss. The pressure gradient may therefore be obtained by combing Eqs. (37) and (40) as:

$$\nabla p = \frac{18\mu\tau V_a(1-\phi)^2}{\phi^3 D^2} + \frac{3}{8}\left(\xi_2 + 4{\xi_2}^2\right)\frac{\tau\rho{V_a}^2(1-\phi)}{\phi^3 D} \tag{41}$$

In Eq. (41), the first term on the right represents the viscous energy loss as a linear function of apparent velocity, with the second term representing kinetic loss as quadratic function of apparent velocity.

5.2.3.3 Governing gas flow equation in a packed-bed

The mass conservation equation for each gas component is given as:

$$\frac{\partial m}{\partial t} + \nabla(\rho_g \overrightarrow{V_a}) = q_s \tag{42}$$

where, ρ_g is the methane density (kg/m³); $\overrightarrow{V_a}$ is the non-Darcian velocity vector (m/s); t is real time (d); q_s is the normalized gas source rate (kg/(kg·s)); m is the gas content (kg/m³), comprising states of free-phase gas and adsorbed gas [83,84]. The gas content is defined in Eq. (B-1) in **Appendix B**.

Eq. (41) gives the pressure gradient, which describes the viscous energy loss and kinetic energy loss in the non-Darcy flow within the gob. From Eq. (41), the equivalent non-Darcyian velocity vector of fluid flow is derived as:

$$\overrightarrow{V_a} = -\left[\frac{18\mu\tau(1-\phi)^2}{\phi^3 D^2} + \frac{3}{8}\left(\xi_2 + 4{\xi_2}^2\right)\frac{\tau\rho V_a(1-\phi)}{\phi^3 D}\right]^{-1}\nabla p \tag{43}$$

Reynolds number (R_e) is a dimensionless number relating the ratio of viscous to inertial (kinetic) losses [75], which is defined as:

$$R_e = \frac{\rho D V_a}{\mu} \tag{44}$$

Eq. (43) can be transformed using the Reynolds number as:

$$\overrightarrow{V_a} = -\left[\frac{18\mu\tau(1-\phi)^2}{\phi^3 D^2} + \frac{3}{8}\left(\xi_2 + 4\xi_2{}^2\right)\frac{\tau\mu(1-\phi)}{\phi^3 D^2}R_e\right]^{-1}\nabla p \tag{45}$$

Substituting Eqs. (B-1), (B-2) and (B- 3) and (45) into Eq. (42), the governing equation for gas flow in the gob can be defined as

$$\left(\frac{M\phi}{RT}\right)\frac{\partial p}{\partial t} - \nabla\left\{\frac{pM}{RT}\left[\frac{18\mu\tau(1-\phi)^2}{\phi^3 D^2} + \frac{3}{8}\left(\xi_2 + 4\xi_2{}^2\right)\frac{\tau\mu(1-\phi)}{\phi^3 D^2}R_e\right]^{-1}\nabla p\right\} = -(1-\phi)\rho_{ga}\rho_c\frac{\partial V_g}{\partial t} + q_s \tag{46}$$

The remaining gas content in the granular matrix can be calculated from the quasi steady-state equation for methane desorption [85,86], given by

$$\frac{\partial V_g}{\partial t} = -\frac{1}{t'}\left(V_g - V_{gd}\right) \tag{47}$$

where, t' is the gas diffusion time (s).

Eqs. (46) and (47) represent the governing equations of gas flow. Specifically, Eq. (46) defines the methane flow equation, where methane content consists of both free-phase gas and adsorbed gas components. Eq. (47) defines the methane desorption process, which will contribute the total methane flow and determine the apparent gas flow rate from the gob. The broken rock blocks in the caved zone is gradually compacted under the near constant overburden loading stress for underground longwall coal mining. The loading stress over the gob evolves with time and the gob compaction process on caved coal measure rocks can be described as a one-dimensional quasi-static consolidation. Thus, the effects of the dynamic gob compaction behaviors on fugitive gas emission process should be involved into the proposed model. As quantified by Eq. (46), two main parameters including the uniform radius of the rock-coal blocks (D) and the gob porosity (ϕ) can be used to quantify the effects of the dynamic gob compaction behaviors on fugitive gas emission process.

5.2.4 In-mine measurement and modeling results

5.2.4.1 Field survey results

(a) Three Measurement Points at Each Location

(b) Measurement Locations: L1, L2, L3…

(c) Field Measurement Point M1

(d) Field Measurement Point M2

(e) Field Measurement Point M3

Figure 5-17: Field investigation locations and measurement points at 6304 the longwall working face. (a) Three measurement points, M1, M2 and M3, are defined at each location. (b) Distributions of investigation locations at the 6304 working face. (c), (d), (e) Field investigator sampling.

Field measurements of airflow quantities and methane concentrations were conducted at the 6304 working face of the Tangkou coal mine. The measured methane concentrations and airflow quantities were used to estimate the average gas emission rates from the compacted mine gob and to validate numerical implementations of the gob emission model described in the previous. These results can ultimately provide the data for analyzing the interactions between the caved gob and the ventilation system and to define mitigation strategies to minimize gas concentrations and hazard.

As discussed in Section 5.2.2, there are three discrete geometries of the panel, defined by width. For the *in situ* methane concentration monitoring, nine evenly spaced field measuring stations (L1, L2, L3…L9) were located at the active working face for the widest panel. Five evenly spaced measuring stations were located in the transition and narrow panels, respectively, as illustrated in Figure 5-17(b). At each gas concentration measuring station, three measuring points (M1, M2, M3) were designated, as shown in Figure 5-17 (a). Average gas concentrations were determined from the mean of the group of three monitoring points at each station with each group measured three times and again averaged. Figure 5-17(c) shows field measurements being taken at the three corresponding measurement points at a given measuring station with these data listed in Table 5-1.

47

Based on the field investigation data in Figure 5-18 and Table 5-1, we can estimate the gas emission rates from the gob by using the methane concentration at the working face in conjunction with air quantities in the intake and return airways. From Figure 5-18, the average methane concentration at the active portion of the wide panel is higher than that of transition panel. Also, the methane concentrations at the narrow panel are clearly lower than those of the two previous panels, which can be attributed to the lower production capacity at the narrow panel. For each of the measuring station, the difference between three measurement points are insignificant, suggesting that the average methane concentration should be sufficient for modeling. This observation of homogenized methane concentrations suggests turbulent mixing t the face - desirable to prevent methane layering and concentration.
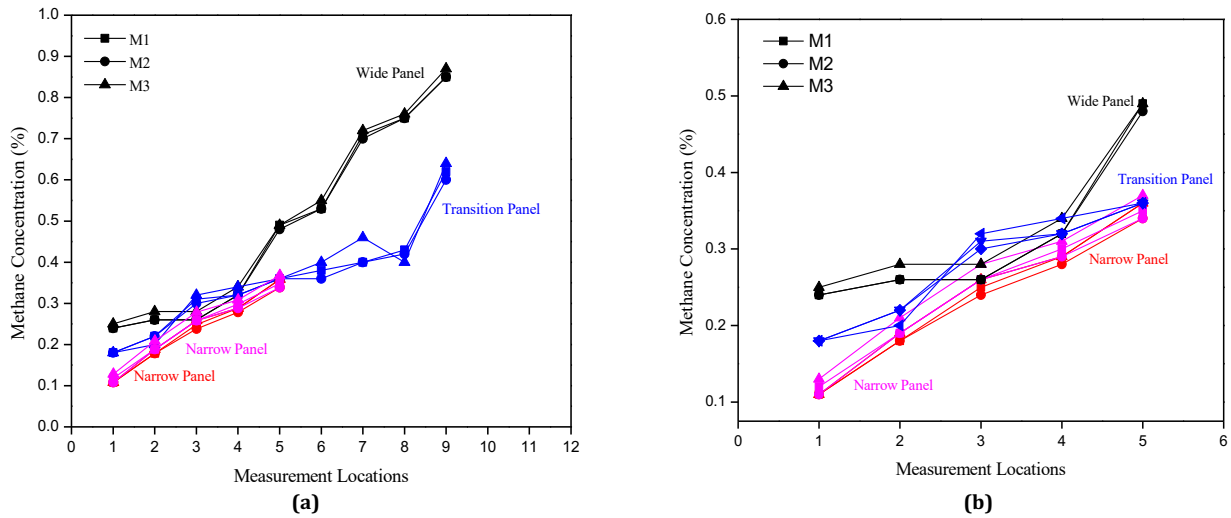
Figure 5-18: Field methane concentrations at investigation locations. (a) Nine locations at the widest portion of the panel (June 9th, 2018), transitional section (Aug 4th, 2018) and narrow panel section (Nov 10th and 12th, 2018). (b) Normalized methane concentrations at the same five locations.

Table 5-1: Field investigation recovered methane concentrations (%) in the three panel geometries.

	Field Investigation Date and Measurement Points (M1, M2 and M3)												
	06/09/2018			08/04/2018				11/10/2018			11/12/2018		
	Wide Panel			Transition Panel				Narrow Panel					
	M1	M2	M3	M1	M2	M3		M1	M2	M3	M1	M2	M3
L1	0.24	0.24	0.25	0.18	0.18	0.18	L1	0.11	0.11	0.11	0.12	0.11	0.13
L2	0.26	0.26	0.28	0.22	0.22	0.20	L2	0.18	0.18	0.19	0.19	0.19	0.21
L3	0.26	0.26	0.28	0.31	0.30	0.32	L3	0.25	0.24	0.26	0.26	0.26	0.28
L4	0.32	0.32	0.34	0.32	0.32	0.34	L4	0.29	0.28	0.29	0.30	0.29	0.31
L5	0.49	0.48	0.49	0.36	0.36	0.36	L5	0.36	0.34	0.36	0.35	0.34	0.37

48

L6	0.53	0.53	0.55	0.38	0.36	0.40
L7	0.71	0.70	0.72	0.40	0.40	0.46
L8	0.75	0.75	0.76	0.43	0.42	0.40
L9	0.85	0.85	0.87	0.62	0.60	0.64

Methane concentration monotonically increases from headgate to tailgate (Figure 5-18). This finding is also expected, as the methane incrementally accumulates from discharges along the longwall panel face, from headgate to tailgate. Empirical regression of the average methane concentration with distance from the headgate show a strong linear correlation as shown in Figure 5-19. We used the fitted linear relationship to estimate the average methane concentration for the working panel at different stages of development, including for the wide (182 m), transition (141m) and narrow (60 m) panels. For example, the fitted linear relationship between the average methane concentration at a given location and the distance from the intake entry during the excavation of the wide panel is shown as $y = 0.00367x + 0.1601$ (Black line in Figure 5-19). The average methane concentration over the entire panel is defined as $\bar{C}_1$ and calculated from $\frac{\int_0^{182}(0.00367x+0.1601)dx}{182}$, is ~ 0.494. Methane concentrations are similarly estimated during the successive recovery of the different panels with these data listed in Table 5-2. Then, we assume the relation between air quantities in the intake and return airways can be expressed as:

$$Q_r = Q_e + Q_i \tag{48}$$

where, Q_i and Q_r are air quantities in intake and return airways (m^3/s); Q_e is the gas emission quantity (m^3/s), which mainly consists of air-methane emission quantity from gob, methane emission quantity from panel and possible air leakage quantity from adjacent strata. It is apparent that the gas emission rates from gob to face can be quantified as,

$$q_e = Q_e \bar{C}_i \tag{49}$$

where $\bar{C}_i (i = 1, 2, 3, \cdots)$ is the average methane concentrations distributed along with the working face (%); and q_e is gas emission rate (m^3/s).
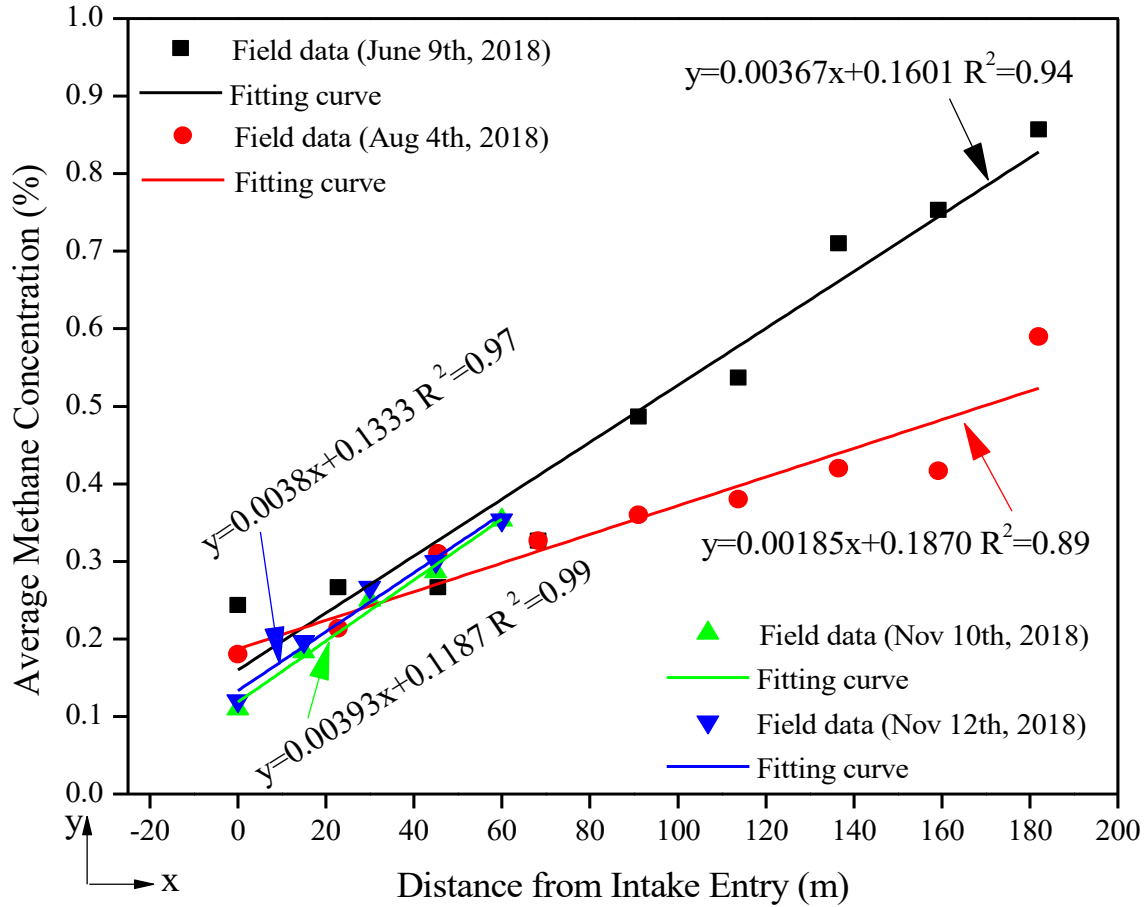
Figure 5-19: Distributions of average methane concentrations at the 6340 working face.

Gas emissions (Q_e) could emanate from several sources including air-methane emissions from the gob, methane emissions from the panel and possible air leakage from adjacent strata, but it is difficult to distinguish and accurately estimate the amount coming from each source. For this particular mine, there is no bleeder system and the burial depth of the coal seam is deep (~950m), therefore it is reasonable to assume the gas emission is only from gob and for pure methane. To calculate the reliable and real-time methane concentration, the stable mine ventilation status during the operation of 6304 working face was initially assumed. To justify this assumption, we conducted the mine-wide ventilation during the mining operation period of 6304 working face (June 9th, 2018), the ventilation survey result was shown in Figure 13. From the ventilation survey results, the air quantity at 6304 working face during the wide panel period is ~40.6 m³/s. Then we monitored the methane concentration at different times (June 9th, 2018; Aug 4th, 2018; Nov 10th, 2018; Nov 12th, 2018), and we simultaneously recorded the airflow quantity when we tried to monitor the methane concentration (as illustrated in Table 5-2). The results in Table 5-2 shown that the air quantities at June 9th, 2018 and Aug 4th, 2018 were almost same, which were 40.6 m³/s and 40.10 m³/s respectively. Similarity, the air quantities at Nov 10th, 2018 and Nov 12th, 2018 (the time during the narrow panel period) were

also almost same, which were 22.50 m³/s and 22.09 m³/s respectively. The field gas emission rates were estimated and all the results are listed in Table 5-2.

Table 5-2: Gas emission rates.

Parameters	Location	June 9th, 2018	Aug 4th, 2018	Nov 10th, 2018	Nov 12th,2018	Source
Air Quantity(m³/s)	Intake Entry	40.60	40.10	22.50	22.09	Field Monitoring
	Return Entry	41.83	41.33	23.40	22.99	Field Monitoring
Average Methane Concentration (%)	Working Face	0.494	0.355	0.247	0.237	Integration
Average gas emission rate (m³/s)	Gob	0.0061*	0.0044*	0.0022*	0.0021*	Estimated

* the actual gas emission rate is lower than this maximum theoretical value.

5.2.4.2 Numerical modeling of gas flow

COMSOL Multiphysics was employed to simulate gas flow in the compacted gob and to predict the gas emission rates. In order to validate the numerical simulation model, methane concentrations measured at the 6304 working face were used. Accurate estimation of the gas emission rates from the gob at any given time is challenging due to the complex mining environment and working conditions. Based on the mine field visit and the layout of 6304 working face (Figure 5-15(c)) developed from real mine map, the regular layout of 6304 working face can help simplify the spatial layout 6304 working face from 3D version to 2D version, and thus the cutaway of the 6304 working face can be established as the geometry model.

The caving ratio, rear support length and rear support angle define the geometric arrangement at the face, as shown in Figure 5-20. The caving ratio represents the ratio of caving thickness to the excavated height, as shown in Figure 5-20(d). The rear support length and rear support angle are the horizontal control length of the rear support of the shield and the angle between rear support shield and level ground, as illustrated in Figure 5-20(d). The caving ratio is ~1.4 for the 6304 working face. The rear support length is a fixed value at 1 m behind the rear support shield (Figure 5-20(c)) and the rear support angle is 45°. A schematic of the face is illustrated in Figure 5-20(c). Figure 5-20 (b) shows a caving thickness of ~5.6 m and therefore the excavated height is ~ 4 m (average thickness of the coal seam is ~ 9.6m). The top caving zone is represented in the vertical direction by boundary ① in Figure 5-20 (b), which is separated from the excavated panel by the top shields. Boundary ① is termed the caved-zone line. Boundaries ② and ③ represent the tilted shield and top-coal caving gate as shown in Figure 5-20 (b). Thus, it is clear that boundary ③ will be the gas emission boundary between the 6304 working face and the gob. Boundaries ④, ⑤ and ⑥ represent the ground floor, rear boundary and immediate roof as shown in Figure 5-20 (b). Whittaker and Singh (1979) assumed that the gob can recover its original stress at a distance of ~45m from the face. Using

Flac[3D], Abbasi et al. (2014) estimated the mechanical response of the gob from field measurements. The results indicate that the gob achieves pre-mining overburden stress at ~55m behind the back-end of the shields[87]. If we assume that the gas stored in the compacted gob region recovered to pre-mining overburden stress has negligible influences on the face, it is reasonable to preset the gob length as ~50m in our model, as illustrated as the length of boundary ④. In LTCC mining, the caving region over the shield will also affect gas emission rates at boundary ③. Summing gob length and shield supported distances yields a total length of boundary ⑥ as 53m.
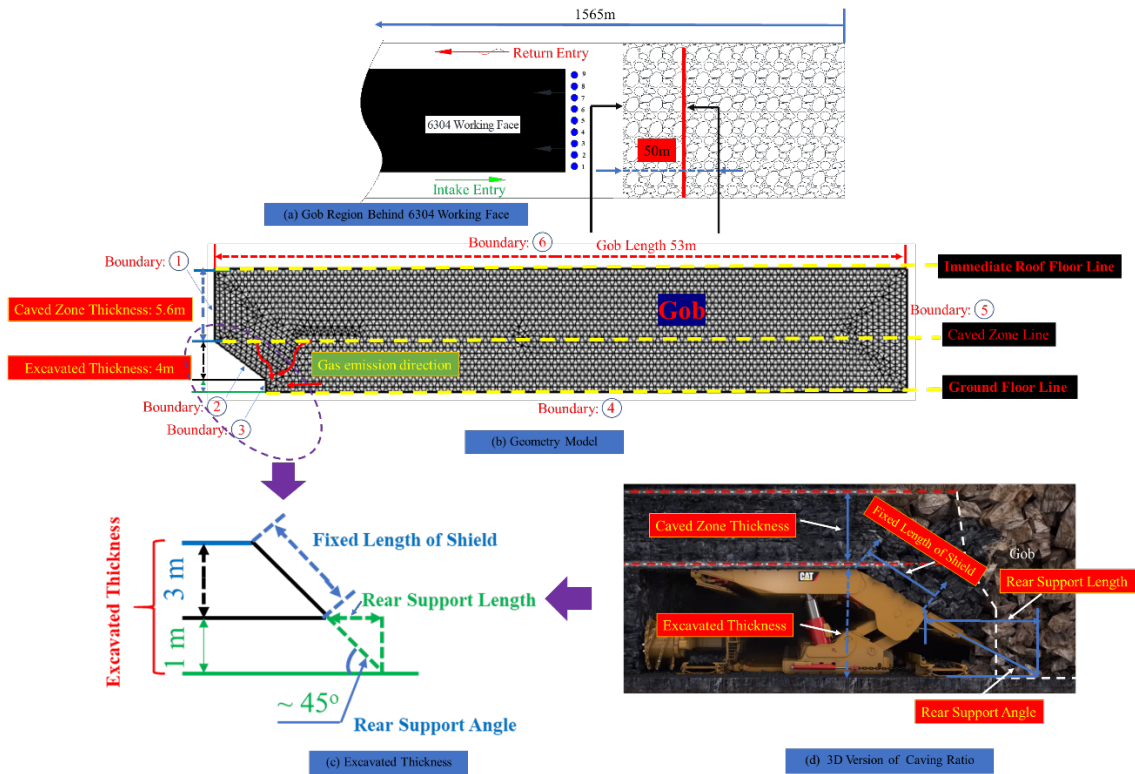

Figure 5-20: Geometric model for compacted gob and boundary locations. (a) Top view of gob region behind the 6304 working face. (b) Cutaway vies of geometric model. (c) Geometry of the excavation. (d) 3D View of the excavation.

Input parameters are key in determining the fidelity of the final results. Unfortunately, only sparing data are available. Laboratory tests on rock materials, with approximate particle size gradations of the actual gob material recovered from headgate entries in Eastern Kentucky coal mines, have been used to determine the mechanical properties of the gob for numerical models [41]. A set of physically meaningful data based on physically similar laboratory samples have been obtained [41]. The experimental data have been screened against predictive porosity and permeability models [19]. Thus, some parameters were taken from the literature. The mine specific data were either measured in the laboratory or recovered from the field. The Reynolds number can be determined by field survey of velocity and other known parameters of gas density, gas dynamic viscosity and an assigned characteristic dimension. Another parameter is

the methane diffusion time in the homogenous rock-coal porous medium constrained by the diffusion coefficient of pure methane in the coal matrix. All parameters are as listed in Table 5-3.

Table 5-3: Basic input parameters.

Parameters	Values	Source
Molar mass of gas (kg/mol)	16.0	constant
Universal gas constant (J/(mol·K))	8.314	constant
Temperature (K)	301.0	field test
Dynamic viscosity (Pa·s)	1.84e-5	constant
Tortuosity	1.26	Pappas and Mark (1993)[41]
Porosity	0.3	Pappas and Mark (1993)[41]
Langmuir pressure (MPa)	0.62	experimental test
Langmuir volume (m³/t)	4.8	experimental test
Reynolds number	2.0	assumed
Block size (cm)	51.0	Pappas and Mark (1993)[41]
Rock-coal density (g/m³)	2.0	experimental test
Gas density at standard condition (kg/m³)	0.707	constant
Initial pressure (MPa)	0.72	field test
Diffusion time (d)	5.0	assumed

Table 5-4: Boundary conditions for three cases.

Cases	Boundaries			
	1	3	6	2&4&5
1	zero flux	p_{c1}; V_{gc1}	zero flux	zero flux
2	p_{c2}; V_{gc2}	p_{c1}; V_{gc1}	zero flux	zero flux
3	p_{c2}; V_{gc2}	p_{c1}; V_{gc1}	p_{c2}; V_{gc2}	zero flux

where, p_{c1}= 0.1MPa; p_{c2}= 0.72MPa; $V_{gc1} = V_L p_{c1}/(p_{c1} + p_L)$; $V_{gc2} = V_L p_{c2}/(p_{c2} + p_L)$.

Moreover, the initial and boundary conditions are required for the numerical modeling. In all three cases, the initial conditions with initial gas pressure and content of 0.72 MPa and 2.58 m³/t respectively are identical. However, different boundary conditions were used. In Case 1, except for the gas emission boundary ③, all the other boundaries were set with zero flux. In Case 2, boundary ① representing the interface between the top-caving region and the gob (Figure 7(b)) was set as gas source term. In Case 3, gas sources were supplied from boundaries ① and ⑥. The detailed boundary conditions are listed in Table 5-4.

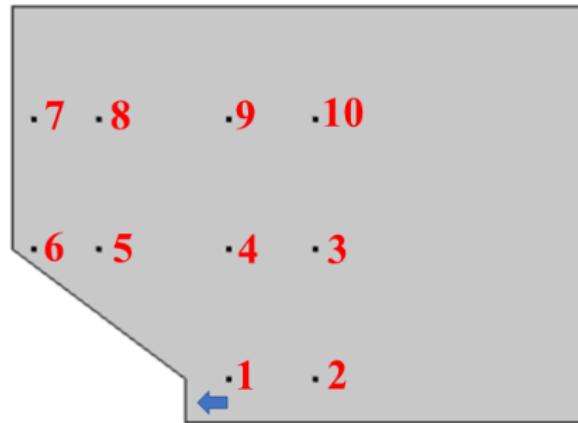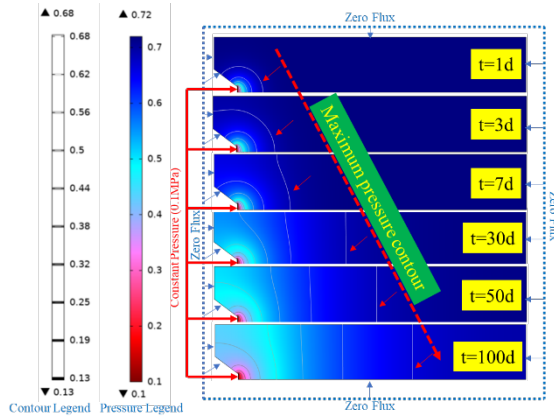### 5.2.4.3 Pressure distribution in the caved gob

Figure 5-21: Distributions of monitoring points.

In order to evaluate gas pressure distribution within the gob, ten monitoring points were set within the simulation model, as shown in Figure 5-21. Figure 5-22 depicts the distributions of gas pressure within the gob under different boundary conditions. In all three cases, gas flow profiles were simulated for one hundred days. In all simulations, we observed that the pressure gradually increases from the rear support gate towards the deep compacted gob with results illustrated by the pressure contours as well as the pressure decline curves as shown in Figure 5-22. The rear support gate retains the lowest pressure and the pressure progressively increase towards the gob. As time elapses, the low pressure region move progressively deeper into the gob.
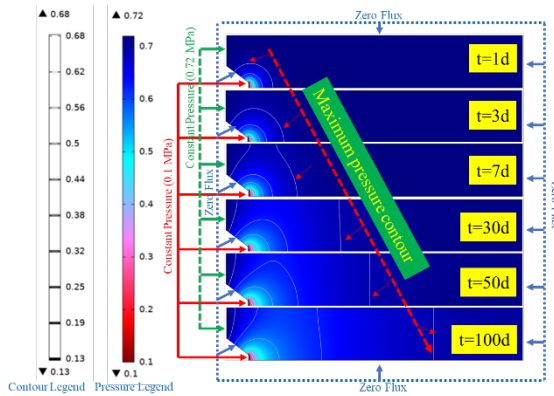
The different boundary conditions noted previously can significantly influence the dynamic pressure profile within the gob. In case 1, zero flux boundary conditions were set on all the boundaries except for the gas emission from the gob boundary ③. Therefore, Case 1 represents the case where gas emission is solely from the caved rock-coal mass. The gas pressure would decrease to zero at very long times (infinite time). In Case 2, there is an additional gas source from boundary ① due to the gas influx from the top-caving region. Thus, gas content supplemented by boundary ① and the initial gas content in the caved gob will induce continuous gas emission from the gob. Compared with Case 1, the pressure depletion is delayed in the gob due to the additional gas source from the top-caved zone. This is illustrated in Figure 5-21 where the maximum pressure contour moves towards the face. This is partially apparent from the maximum pressure distribution on the adjacent region at the top-left side, as shown in the pressure decline curve for Case 3 (Points 6 and 7).

The gas emission rate from the gob to the face can be quantified by integrating the velocity function across the gas emission boundary (area of boundary ③)-the velocity is quantified in Eq. (54). The estimated gas emission rates are given in Figure 5-22. For all three cases, the gas emission rate in Case 1 is lowest and decreases rapidly with time. In Cases 2 and 3, the gas emission rate decreases in early time but the gas emission rates in both cases finally reach

stable values. The differences between these three cases can be attributed the differing boundary conditions. In Case 1, there is no gas source from any boundary, which means the cumulative gas emission quantity in this case is absolutely determined by initial gas contents in the rock-coal blocks - based on the term $q_s = 0$ in Eq. (46). At later times, the gas emission rate will decrease to 0 due to the finite initial gas content. For Cases 2 and 3, there are constant gas sources from the boundaries and theoretically the cumulative gas emission quantities will continuously increase with time. By recalling the gas flow control equation of Eq. (46), q_s is a constant in each case. The gas emission rates in these two cases will show a slightly decreasing trend relative to that of Case 1 at initial time due to the gas content supplements from gas source boundaries. Instead of gas emission rate showing a continuously decreasing trend with a final theoretical value of 0, gas emission rates in these two cases will decrease to constant values. This is due to the gas source boundaries, which is further apparent by comparing the higher gas emission rate in Case 3 to that of Case 2 because Case 3 has an additional gas source boundary (Top roof boundary) for Case 2.
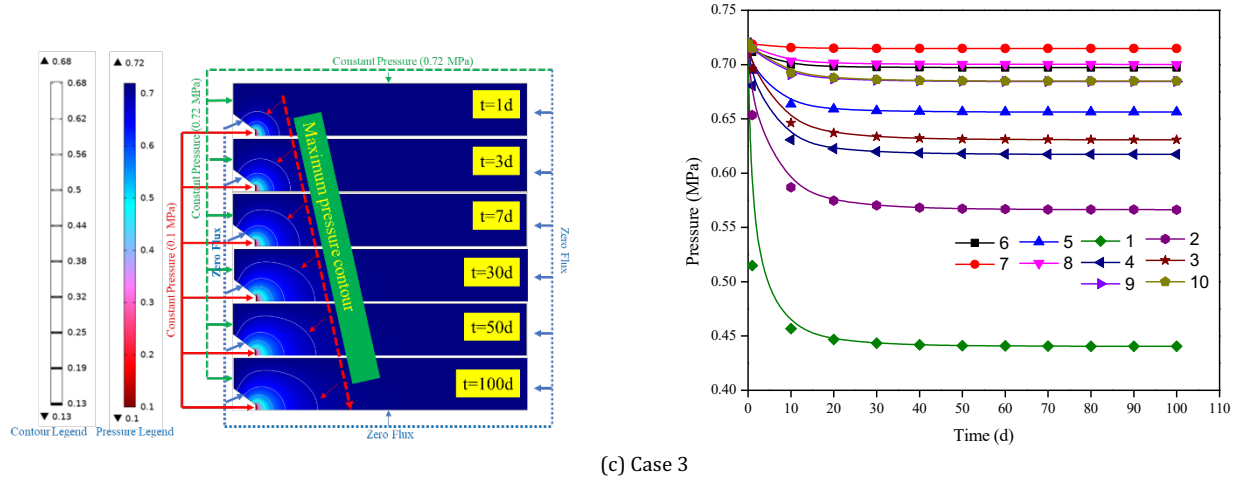

(a) Case 1

(b) Case 2

55

(c) Case 3

Figure 5-22: Pressure distributions in the gob under different boundary conditions.
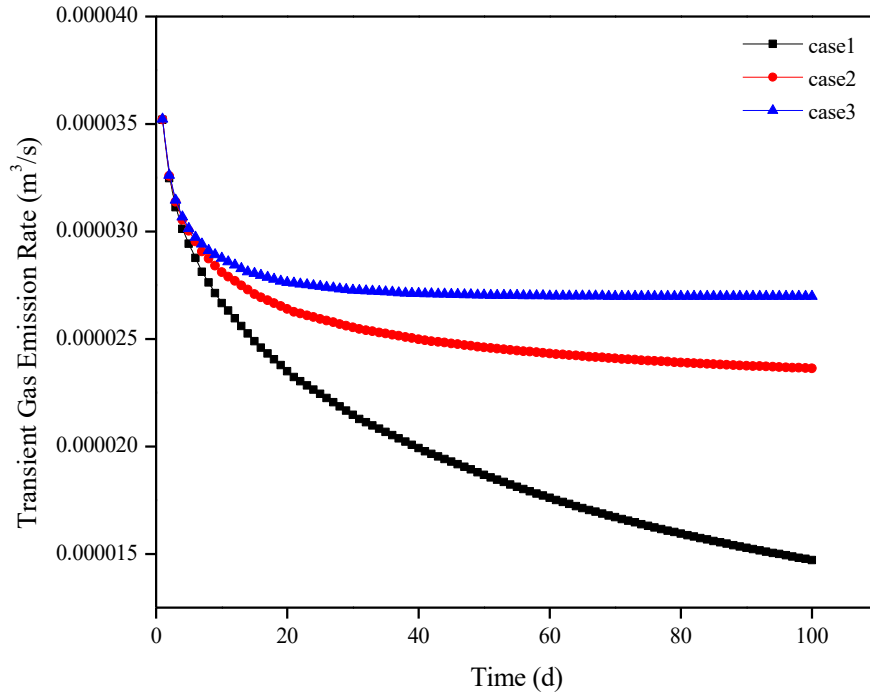
Figure 5-23: Curves of gas emission rates for the three cases. In Case 1, gas emission comes solely from the caved rock-coal mass without other gas sources. In Case 2, there is an additional gas source from boundary ① due to the gas influx from top-caved region. in Case 3, there are two additional gas sources from boundary ① and from the top roof boundary ⑥.

5.2.4.4 Numerical model calibration and validation

It is apparent that the transient gas emission rate in each case decreases with time (Figure 5-23). Since the gas emission rate from the gob to the face is quantified by integrating the velocity function across the gas emission boundary (area of boundary ③), the transient gas emission rate profile reflects the time-dependent effects of accumulated gas emissions from the gob

56

region (with a gob length of 53m) to face. In the mine operation, the longwall face continuously retreats and our field monitored data reflect gas emission rate over a particular time period because the survey was conducted along the longwall panel face from headgate to tailgate. The estimated gas emission rate at the face should be an average of the transient gas emission rate during the field investigation time period - this average gas emission rate may be used to validate the modeled results.

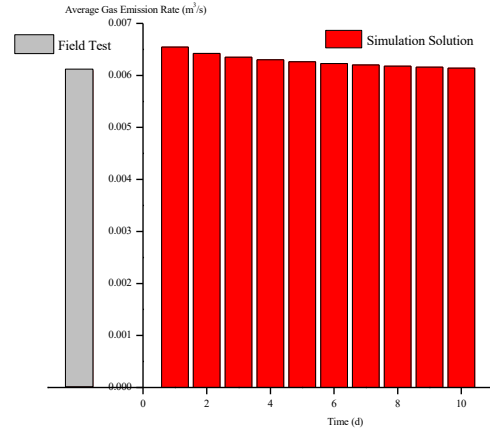The average gas emission rate is quantified by integrating the transient gas emission rate profile over a prescribed time period, mathematically expressed as:

$$q_a = \int_0^t \frac{q_t}{t} dt \tag{50}$$

where, q_a is the average gas emission rate, m³/s; q_t is the transient gas emission rate, m³/s; and t is the designated time period, d.
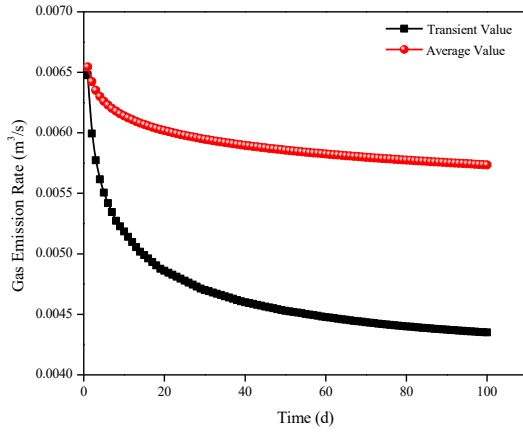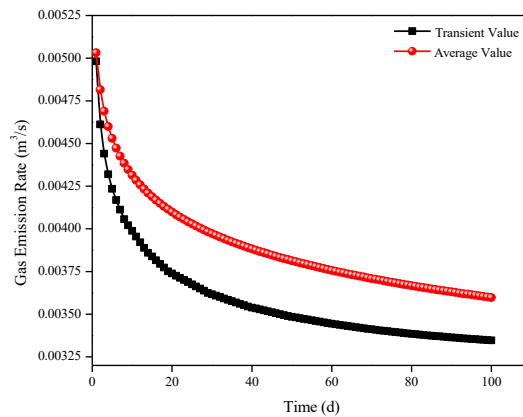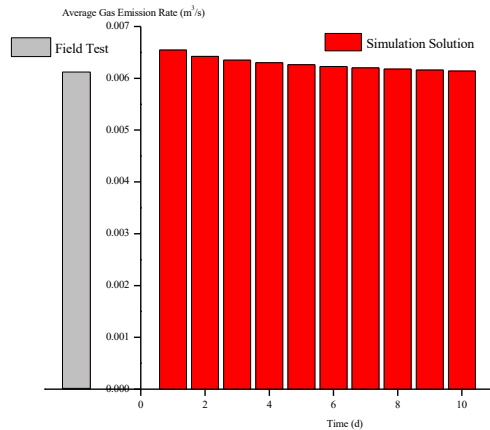

(a1)

(a2)

(a) Wide panel

(b1)

(b2)

(b) Transitional-width panel
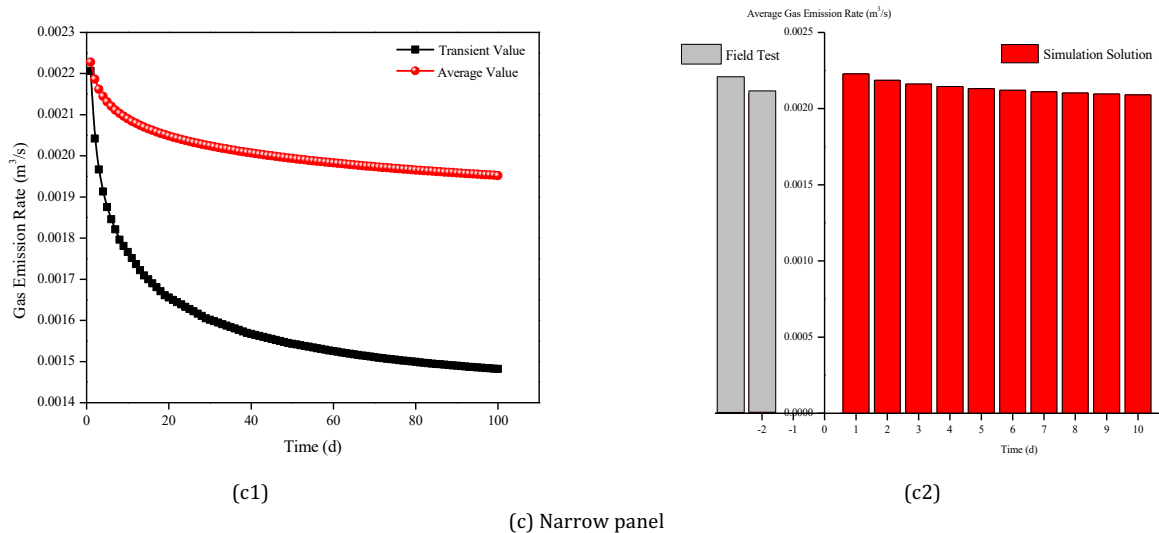
57

(c1)

(c2)

(c) Narrow panel

Figure 5-24: Comparations between simulation solutions and field data. (a) Wide panel. (b) Intermediate-width panel. (c) Narrow panel. (a1), (b1) and (c1) are comparisons between transient and average gas emission rates. (a2), (b2) and (c2) are comparisons between simulation solution and field test data.

For the 6304 working face, the only gas source is from the top-coal caving region and the following simulation solutions are obtained based on Case 2 in Section 5.2.4.3. As the 6304 working panel progressively advances at an advance rate of ~ 5m/d, the newly formed length of the gob is ~50 m in 10 days. In Figures 5-24(a1), (b1) and (c1), we estimated the average gas emission rate over 100 days and then use 10day averages of the gas emission to validate the field test data, as illustrated in Figures 5-24(a2), (b2) and (c2). This shows that the simulation results agree well with the field investigation data. The results also show that the estimated average gas emission rate over the initial short time period reflect the estimated gas emission rate much better, which implicit that the effects of gob gas emissions from a certain gob length will mainly be reflected by a relative short time period. The reason is that the formation of the gob is synchronous with the progressive advance of the panel advancing. The progressive formation of the new gob region will accumulate and emit gas in the early period when the gob is created. If panel advance is halted, gas emissions from the gob to the face need a relatively long time to develop and should be reflected in the average gas emission rate averaged over a long time period.

5.2.5 Discussions on the gas emission from gob to the ventilation system

As the mechanical shearer progressively excavates and allows the collapse of the coal, the gob gradually consolidates sufficiently to support a large proportion of the overburden weight [41]. Compacting coal mine gobs are a particularly unique packed bed undergoing dynamic compaction and with an unusually irregular size and shape distribution of rock-coal blocks. The gradually compacted rock-coal behavior results in a reduction in both porosity and the associated permeability of the gob zone. The gob compaction behavior will influence the airflow

and the concurrent migration of methane through control variables such as porosity and permeability which will also be reflected in the gob gas emission rate. To evaluate the gas emission intensity from the gob and its interaction with the ventilation systems, a mine-wide ventilation pressure and flow rate survey (p-Q survey) is necessary to establish a ventilation network model.

5.2.5.1 Effects of gob compaction behavior on gas emission rate

The challenging conditions of the gob environment make it particularly difficult to conduct direct measurements of porosity and permeability. A few previous studies have quantified these two parameters both experimentally and theoretically [19,41,69,70]. The commonly used cubic law linking permeability and porosity[48,49,88,89], allows permeability to be evaluated from the porosity. Thus, we focus on porosity evolution under the influence of size distributions of the rock-coal blocks. Also, the size distributions of the rock-coal blocks both before and after loading must be quantified to simulate gob compaction behavior.

We use a predictive approach [19] that combines fractal scaling in a porous medium with principles of fluid flow. Based on this predictive model, the porosity for a completely fragmented porous medium can be expressed as [19]:

$$\phi = 1 - (\frac{\Omega_{min}}{\Omega_{max}})^{3-D_F} \tag{51}$$

where, ϕ is the total porosity of the fragmented porous medium (dimensionless); Ω_{min} and Ω_{max} are the minimum and maximum particle dimensions (dimensionless); and D_F is the fragmentation fractal dimension (dimensionless).

With an applied stress increment under uniaxial compression, porosity evolution between two successive stress increments can be expressed as:

$$\phi_{i+1} - \phi_i = -\Lambda \left[\frac{\bar{\sigma}^{\frac{m(D_F-1)}{2}-1}}{\frac{m(D_F-1)}{2}-1} - \frac{\bar{\sigma_i}^{\frac{m(D_F-1)}{2}-1}}{\frac{m(D_F-1)}{2}-1} \right] \tag{52}$$

where, ϕ_{i+1} and ϕ_i are the porosities under successive one-dimensional applied stresses; $\bar{\sigma}$ and $\bar{\sigma}_i$ are the applied macroscopic stresses (MPa); Λ is the plastic compressibility index (dimensionless); and m is the Weibull modulus (dimensionless).

Based on Eq. (51), the initial porosity is determined by the size distribution of the rock-coal blocks in the gob and the fragmentation fractal dimension. The porosity evolves with an applied increment of one-dimensional applied stress and is quantified by Eq. (51). As shown in Figure

5-15(a), the increment in one-dimensional applied stress results in a decrease in porosity, which decrease gas emission rates as the permeability decreases, as illustrated in Figure 5-15(b). An eleven-fold increase in stress (1.70MPa to 18.68MPa) results in a nonlinear decrease in porosity of only ~75% (from 0.368 to 0.093) and a 56-fold reduction in gas emission rate (compared to the maximum transient gas emission rate). A sensitivity study was conducted in the numerical modelling to define the evolving porosity (Figure 5-25(a)). As shown in Figure 5-25 (b), high porosity yields high gas emission rates and low porosity significantly reduces the rate. The size distribution of the rock-coal blocks in the newly formed gob are mainly determined by the failure characteristics of the roof. Normally, large rock blocks fall first, followed by smaller blocks, but the large blocks control the elevated porosity, unless significantly infilled by the smaller fraction (Eq. (51)). The overburden stress builds with time and will compress the rock-coal blocks potentially fracturing the large blocks into a smaller fraction, decreasing the range of block sizes. Thus, the size distribution of rock-coal blocks will become finer in the gob, with time, further resulting to the decrease of pore sizes and potentially also of porosity (based on Eq. (52)).
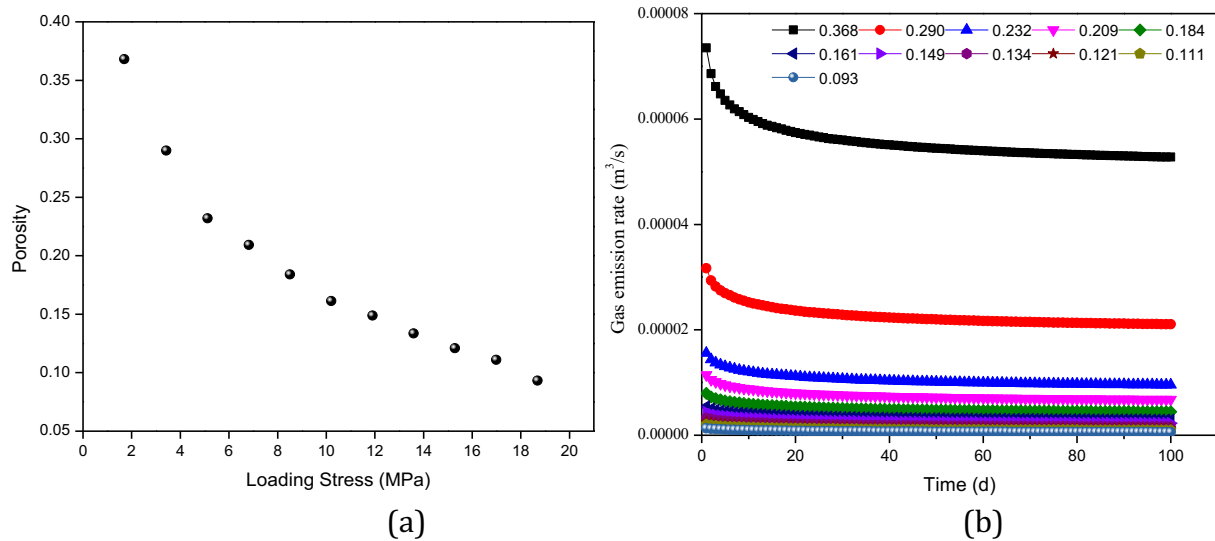
Figure 5-25: (a) Porosity evolution of the gob medium when loaded [12]. (b) Effects of porosity evolution on gas emission rates, recovered by inputting porosities from (a) into the numerical model.

5.2.5.2 Effects of gas emission rate on methane distribution throughout the mine

In order to check the influence of gas emission on the overall methane distribution throughout the mine ventilation network, we conducted mine ventilation network modeling with different gas emission intensities. The Ohioautomation ICAMPS-MineVent software package was selected for the ventilation airflow modeling. The MineVent model allows gas sources to be applied in selected branch(es). This feature was used to investigate the methane concentration distribution throughout the mine ventilation network. The ventilation network model was established to simulate the airflow (Q) distribution for the entire mine as shown in Figure 5-26.

A mine-wide ventilation pressure and quantity (p-Q) survey was conducted, as described previously. These survey data were used to build the network and the ventilation network was validated by the p-Q survey data. From Figure 5-26, it is apparent that the coal mine ventilation system has one intake shaft and one return shaft. Specifically, there were two working faces including the 6304-Face and the 53067-Face during the field investigation periods. Figure 5-26 also shows the simulated results of the air quantity (pink numbers). The field-measured and simulated results agree well - suggesting the fidelity of the network model.

This validated model was used as a base model for the gas injection analyses. In Figure 5-26, node 7 is the demarcation point between the intake and return entries. The gas emission branch between node 7 and the gas injection node was utilized to address the effects of gas emission on the ventilation network. Several gas emission injection rates into the injection branch were chosen from the simulation solutions including 0.00455 m³/s, 0.00510 m³/s, 0.00546 m³/s, 0.00601 m³/s and 0.00637 m³/s. The ventilation modelling indicates that gas emission from the gob to Face-6304 will not affect its parallel ventilation branch that involves Face-53067.
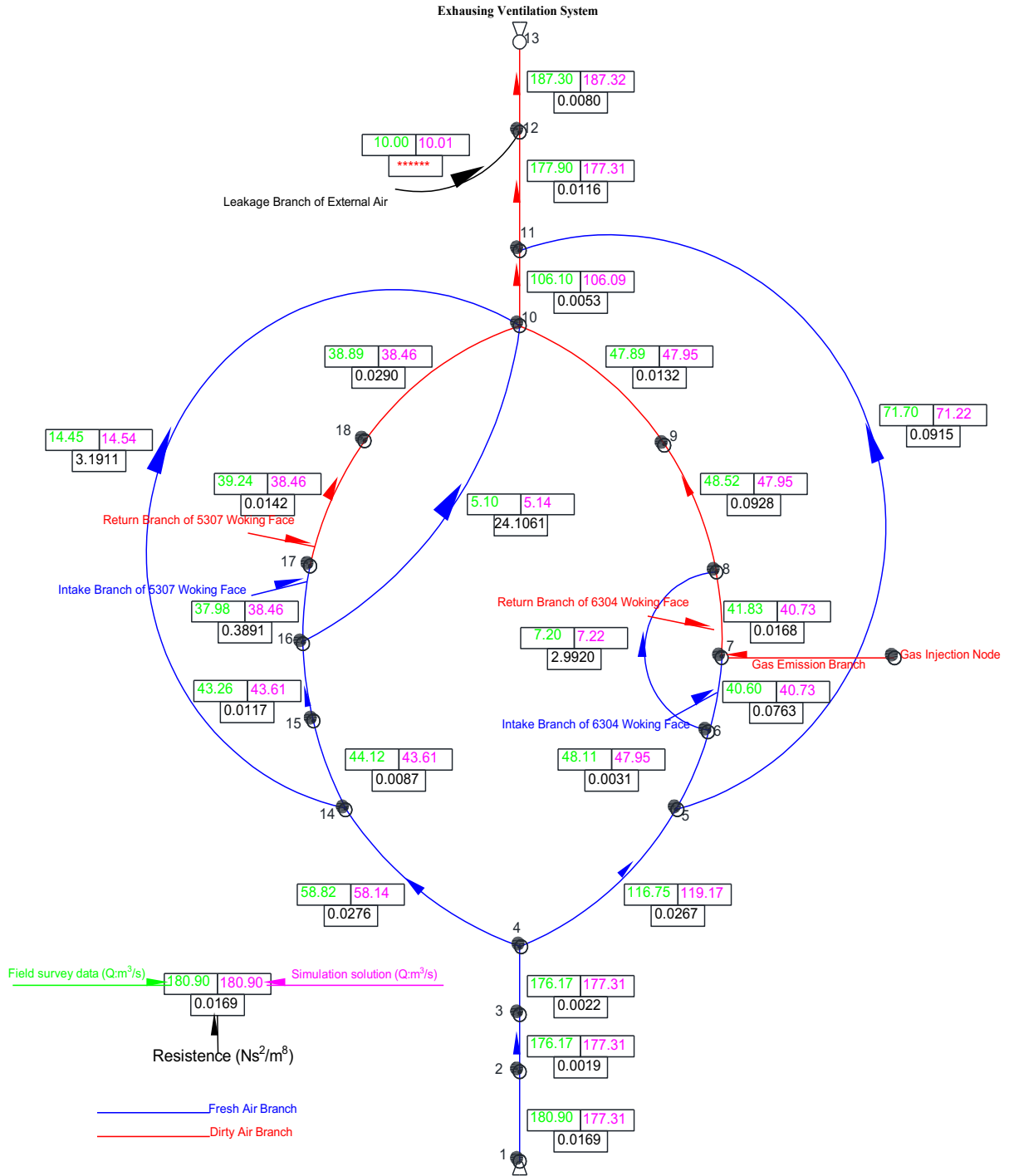
Figure 5-26: Mine ventilation network modelling and gas injection analyses.

After conducting the gas emission injections, the distributions of methane concentrations at different nodes in the branch involving Face-6304 are shown in Figure 5-27. The branch involving Face-6304 includes survey nodes 1, 2, 3, 4, 5, 6, 7, 8, 9, 10, 11, 12 and 13. Among these

nodes, nodes from 1 to 6 are located in the intake entry, and nodes from 7 to 13 are located in return entry. Gas emissions occurs at the working face - that is the branch that starts from nodes 6 to 7. As shown in Figure 5-27, gas emission has no effect on the intake entry and mainly influence the return entry. In each case, the methane concentration decreases in branch 7-8 (between nodes 7 and 8) due to the junction with the fresh air from branch 6-8 (between nodes 6 and 8) to node 8. Also, branch 9-10 shows a decreasing trend due to supplementary fresh air from branches 14-10 and 16-10. The decrease in methane concentration in branch 10-11is also attributed to this dilution by fresh air from branches 5-11. Comparing the five cases, if the gas emission quantity increases from 0.00455 m³/s to 0.00637 m³/s, a 50% increase, the peak methane concentration at ventilation node 7 increases by 39.7%, from concentrations of 2.24% to 3.13 %. Based on the mine ventilation network modelling and gas injection analyses, the mine-wide ventilation system is especially sensitive to methane emission rates and these clearly impact methane concentrations in the return branches. In consideration of the explosive limit of methane, in the concentration range of 5-16%, gob gas emission has the potential to trigger elevated methane alarms although all levels remain below the explosive limits.
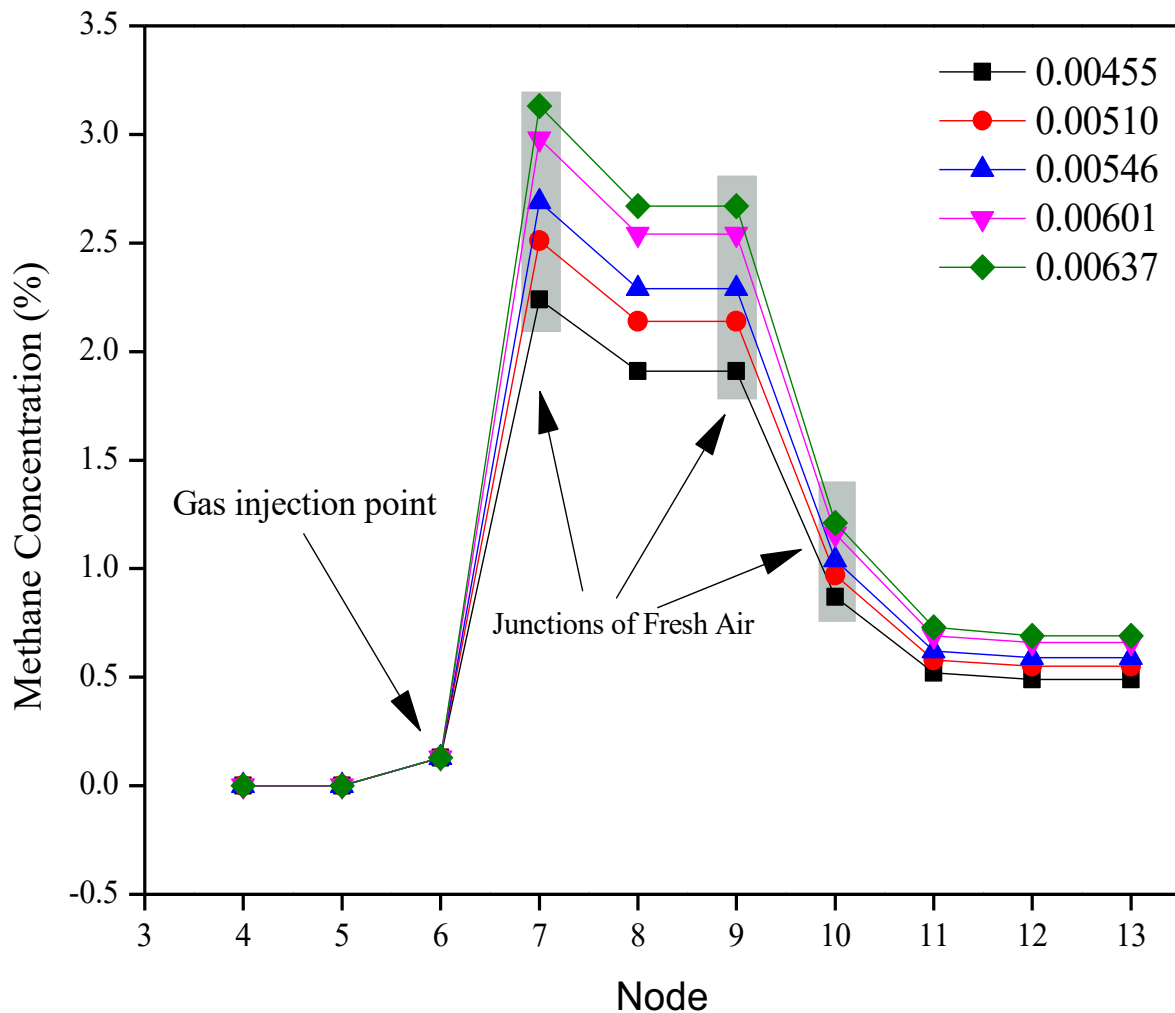

Figure 5-27: Effects of different gas emission rates on the ventilation network.

63

5.2.5.3 Discussion of the comprehensive coupled modeling framework

As discussed in the literature review, NIOSH conducted a series of studies on predicting gob permeability/porosity including semi-empirical and theoretical-based models. In this study, we conducted a systematic study of the prediction of porosity/permeability and the associated gob compaction model as illustrated in Fig. 5-28. By starting from the classical Carman-Kozeny equation ($k = \frac{D^2}{180} \frac{\phi^3}{(1-\phi)^2}$), the gob permeability is sensitive to both particle size distribution and porosity evolution. To derive the dynamic changes of permeability in gob, the two primary contributions of the mechanistic quantification of permeability evolution in this project are the quantification of the stress evolution and the associated porosity evolution (section 5.1.3.1), and the statistic estimation of the particle size distribution of coal-rock blocks (section 5.1.3.2). Most importantly, the evolving stress used for quantifying the deformation of gob materials is not ideally calculated from the overburden stress. The real stress is re-calculated considering the shear stress based on the conceptual gob model in the project specifically due to the boundary force between the fragmented rock medium and the rib resulting from movement in vertical direction. In this project, a mechanism-based flow model (section 5.2.3.2) with physically parameters that may be validated to predict gas emissions from god was incorporated into the reservoir model using COMSOL Multiphysics and calibrated against records of methane flow at an underground longwall coal mine (section 5.2.3.3).
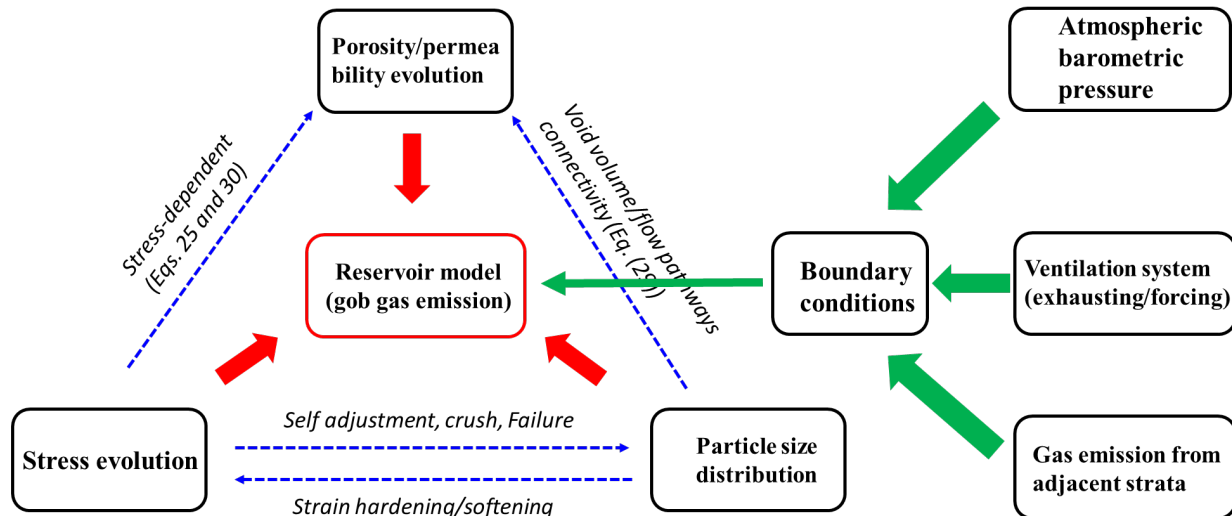
Figure 5-28: The coupled model framework to predict gas emission with coupled geomechanics process and ventilation parameters.

As illustrated in the Figure 5-28, based on some NIOSH pioneer work, we proposed a comprehensive gas emission modeling framework through coupled analytical model and numerical model to fully describe the gas emission behavior from gob to the face by implicitly considering ventilation system, dynamic gob compaction and stress distribution and dynamic permeability.

5.3 CFD modeling for gob and ventilation system interactions

Interactions between gob, bleeder and the longwall ventilation system are explored through a series of model-simulations by both physical model and CFD. A physical model representing a longwall and gob system is assembled, equipped for airflow and trace gas transport and measured for airflow velocities and gas concentrations. These observations are used to calibrate CFD models representing 3D airflows effects across entries and to explore the impacts of presumed roof-fall blockages on the resulting airflow and buildup of ignitable gases.

5.3.1 Lab-scale model description and calibration

A 1/100th physical scale-model of a typical longwall mine was designed and fabricated in the PSU ventilation lab. The model is fabricated from acrylic sheets, representing the mine roof and floor, and with hollow prismatic PVC blocks for pillars. The acrylic sheets are then sealed using double sided sealing tape with the interface between pillar and roof sealed with hot glue (from a glue gun). The model consists of a 'main' section, a continuous miner section, a longwall section, and a ventilation bleeder section. The five entry 'main' measures a total of 3.2 meters in length, augmented by a three entry headgate in the longwall sections. Three of the five entries in the main are designated as intake entries with overcast entries (same dimensions as the entries) connecting the intake and headgate. The dimensions of each entry are 5 cm in width by 4 cm in height. The overcasts, together with the main section, are shown in Figure 5-29.
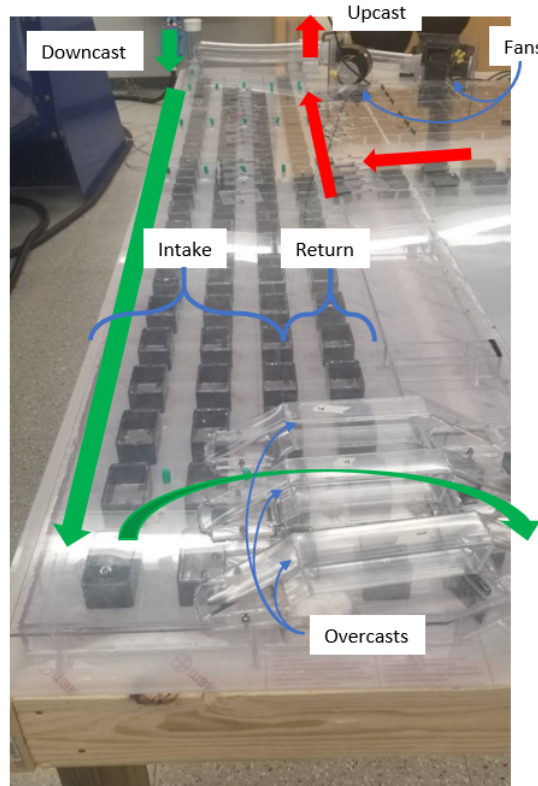

Figure 5-29: Mains and overcasts in the PSU mine model.

The longwall panel is 1 m wide with the scaled working face measuring 8 cm by 4 cm in cross section. Ventilation monitoring is at three locations across the face. The gob, immediately behind the longwall face, measures 1.2 m by ~0.8 m. Glass beads may be arranged in specific patterns to obtain designed porosities within the gob. The gob has 41 ventilation monitoring locations where gas concentration samples may be taken and analyzed. The tailgate and bleeder system also comprise three entries, with the bleeder continuing from the headgate, around the gob, to the bleeder fan. The longwall section and bleeder section are shown in Figures 5-30 & 5-31. There are multiple ventilation monitoring locations in the bleeder system as well as the headgate and tailgate, as illustrated in Figure 5-30. Both permanent and adjustable stoppings allow the ful or partial blocking of airflows, as desired. The continuous miner (CM) section may be fully isolated when it is desired to study longwall response, alone – as completed for this project. Foam plugs seal all ventilation monitoring locations when not in use for sampling and monitoring. The foam plugs are the green dots arrayed along the entry as shown in Figure 5-29.

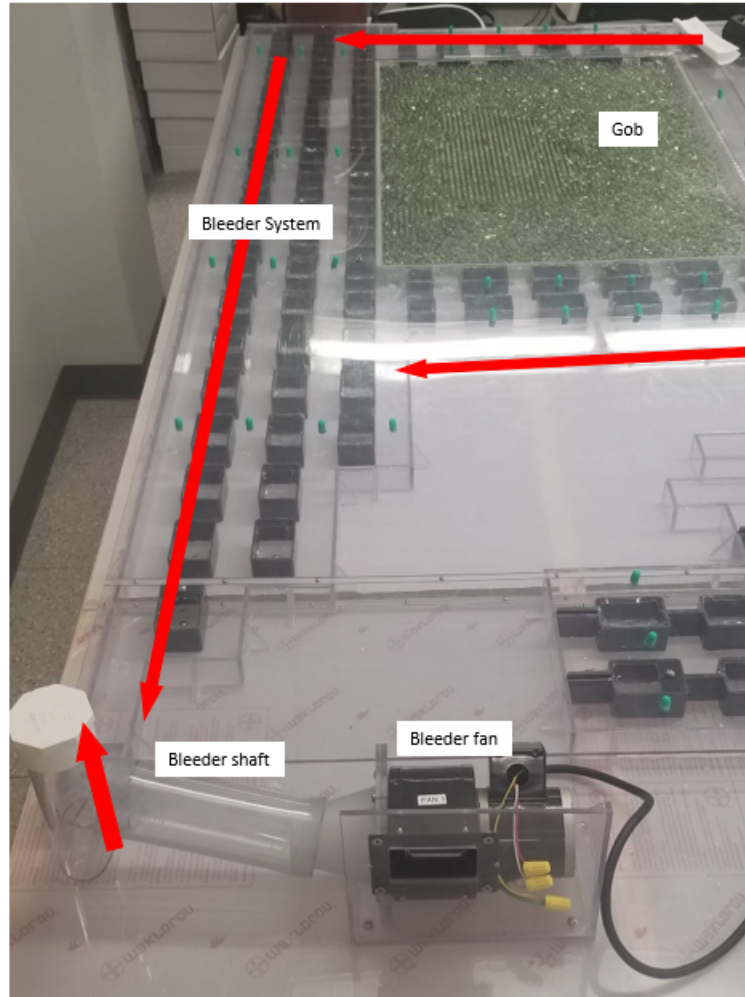*Figure 5-30:* Longwall section in the PSU mine model.

Figure 5-31: Bleeder system in the PSU mine model.

Three fans are installed with locations at: intake entry for a forcing ventilation system, at return entry for an exhausting ventilation system, and with one exhausting fan in the bleeder system. The fans are attached to a variable frequency drive (VDF) *via* a controller allowing high to low power settings. With the forcing fan on high setting, the longwall face can obtain an airflow of 1.2 m³/min.

The PSU mine ventilation model was checked for leaks. One important assumption of the CFD model is that the model geometry should be a closed system, *i.e.* that there is no air leakage. Under this assumption, all airflow entering the system should exhaust at designated ports and satisfy $\sum Flow_{in} = \sum Flow_{out}$. For the subsurface ventilation system, this is a good assumption since total gas emission to the ventilation system is significantly less than the ventilation airflow. To have a calibrated CFD model, it is extremely important to have zero leakage from the physical mine model. In addition, to ensure accurate measurements of pressure gradients, the leakage from entry to entry should be minimized (leakage across parallel pillars).

Hotwire anemometers were used for velocity measurements. Eight anemometers were simultaneously used in conjunction with computer acquisition to record air velocity at designated monitoring locations. Each anemometer measures velocity in the range 0.1 m/s to 25 m/s at a resolution of 0.01 m/s and accuracy of ± 5% of the measured value. The units are PCE America Inc. PCE – 423 models, as shown in Figure 5-32. To maximize accuracy and consistency, the anemometers are aligned parallel to the air flow. Air velocity was consistently measured at the center of each entry or face, representing a single point measurement. This method was chosen after calibration tests showed little measurable difference in velocity readings at varied heights within across the openings. Anemometer placement within the entry is shown in Figure 5-33.

Figure 5-32: Hot wire anemometer used in model validation.

To quantify leakage in the model, velocity measurements were taken at seven locations along a U-tube ventilation scheme. In this, the gob and bleeder system are completely sealed off and the forcing fan set to the highest flowrate. The goal was to determine how to best seal the scaled model. Positions 1-7 in Figure 5-33 were used as velocity measurements positions. The model was sealed with double-sided mounting tape, hot glue, and packaging tape as needed. This continued until the measured intake and return airflow were within 10%. Since each measurement has an inherent error of 5%, an overall 10% error in mass balance was considered acceptable for the measurement. The scale model was used for CFD calibration, modeling and validation once this loss threshold had been met.
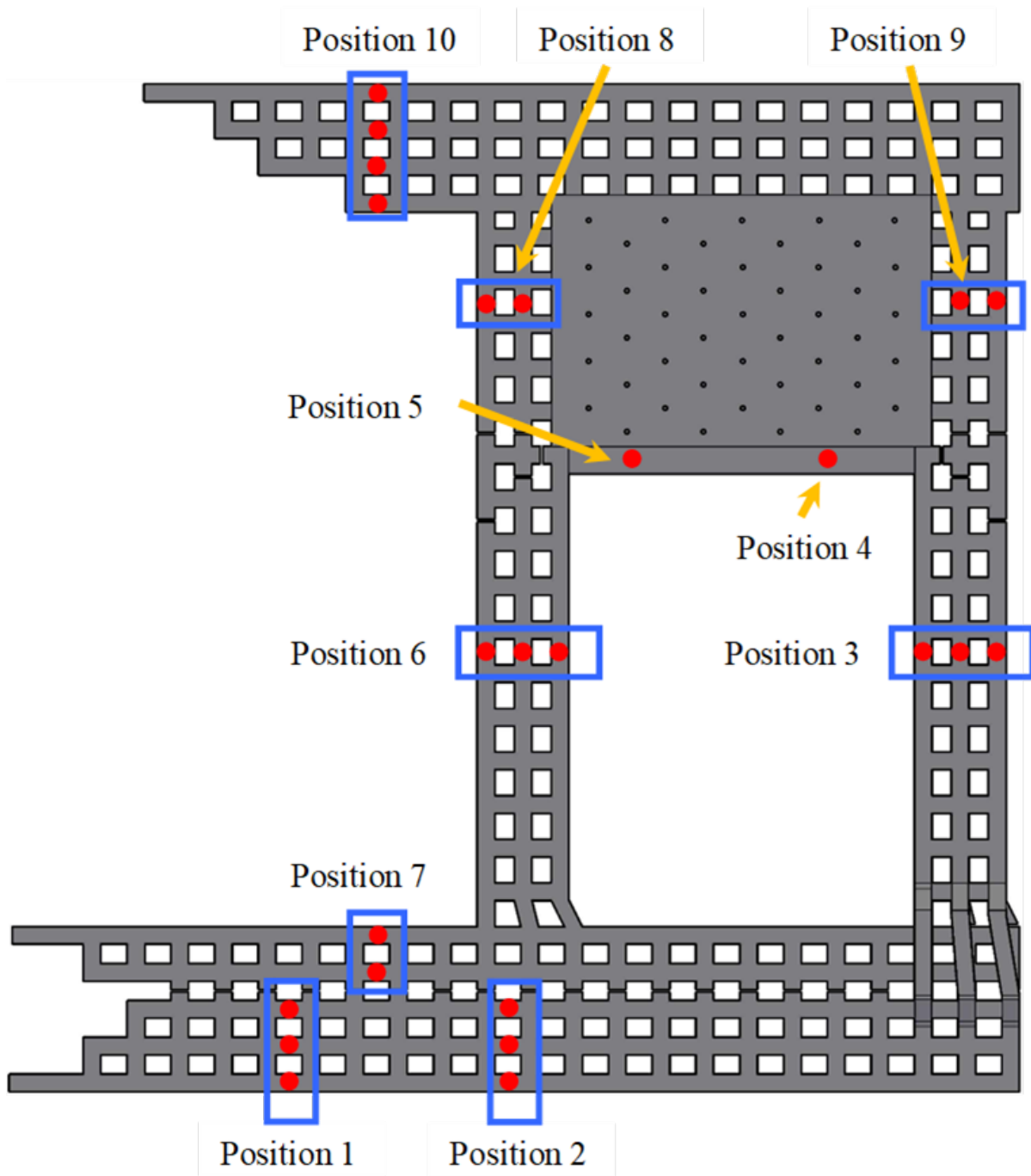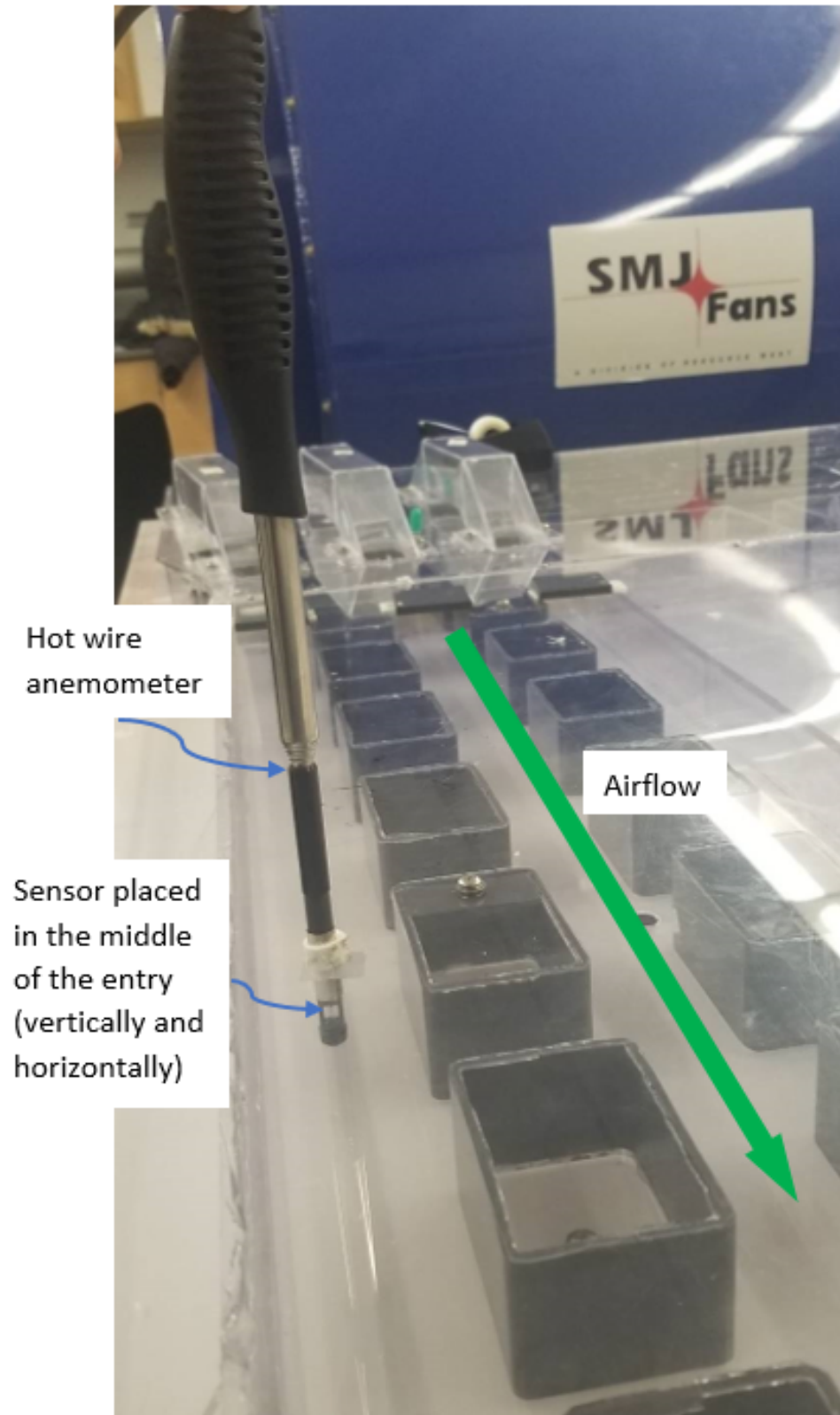
Figure 5-33: Velocity measurement locations.

Figure 5-34: Hot wire anemometer set up from position 3 in Figure 5-33.

5.3.2 Validation of CFD model against experimental results

Velocity measurements for the U-tube ventilation scheme were compared to the CFD modeled velocities. Velocity at seven locations across each entry were compared with the CFD modeled results. Since pressure drops in the scaled model were too low to measure with the current instrumentation, inlet pressure magnitudes in the model were assumed. Subsequently, a trial-and-error method was used to align the velocities in the CFD simulation with the measured scale-model measured velocities. Boundary conditions until the CFD values well agreed with the PSU scaled model measurements. Boundary conditions for the CFD model were adjusted to include wall roughness, total or static pressures, volumetric inflow rates, and outflow rates (for the bleeder). A reasonable estimate of 10% error is was assumed acceptable; however, regions of high turbulence could result higher in higher errors. After a several trials, the U-tube ventilation system was validated with errors limited to <10%.

After validation of the CFD model, the bleeder fan was activated to exhaust at the same flow rate as the main fans. This provided a final independent evaluation between the scale-model and simulation to ensure that the system was fully validated. A porous region was opened to simulate the gob and then added to the CFD model to investigate gas transport behavior in the gob and its influence on the overall ventilation system.

A variety of porosity models are available in Cradle CFD package. The "particle model" was selected for this study due to its similarity to model conditions. Three variables define this system: porosity, particle diameter, and shape factor. Since glass beads where used in the scaled model, a shape factor of 1 (perfect sphere) and a particle diameter of 10mm were used. Gob porosity was unknown, but prior work used 0.1 and 0.15[90] – selected as a baseline for this study. Figure 5-35 shows the porous zones used throughout the gob with input parameters defined in Table 5-5. The zonal distribution of gob porosity is similar to that for real mine conditions, as illustrated in Figure 5-1 with a fully compacted zone in the center and the perimeter less densely compacted.

The main goal of the comparative simulations including gob and bleeder impacts was to determine the capability of the CFD model in representing gob and bleeder flows for a complex geometry. The scaled model was run with the addition of 3 velocity measurement locations in the bleeder (Figure 5-33). The headgate stoppings were kept completely closed with tailgate stoppings fully removed (opened). The measured velocities were then compared to the CFD modeled velocities. The CFD model was then calibrated against the scale-model measured results. Again, an estimated error of <10% was the threshold target.
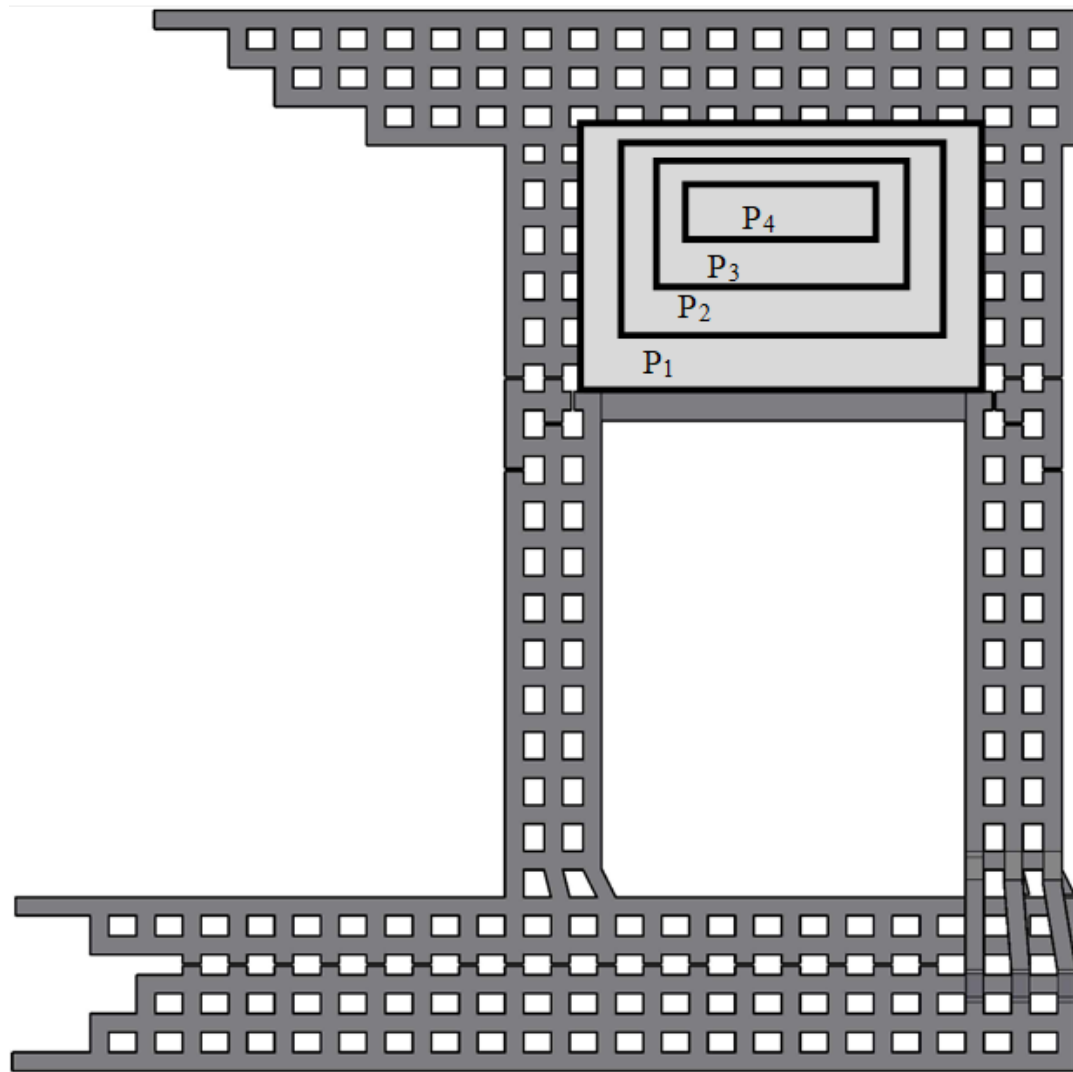
71

Figure 5-35: Gob porosity regions in the numerical simulation.

Figure 5-36 shows the initial model geometry with the final boundary conditions marked for the validated CFD model. This concluded the validation for the CFD model. The completed objectives for the scale-model and CFD modeling included:

1) Design, fabricate and assemble the physical model.
2) Confirm sealing and preliminary validation of the model (<10% error).
3) Complete CFD meshing for current and future simulations.
4) Confirm capability to recover high fidelity velocity measurements from a U-Tube scheme
5) Confirm capability to predict CFD velocities within <5%-10% error.
6) Confirm capability to predict CFD velocities bleeder and gob velocities within <5%-10% error.

Table 5-5: Gob porosities used for different porosity zones

Gob regions	P1	P2	P3	P4
Gob porosity	0.15	0.13	0.12	0.1
Shape factor	1	1	1	1
Particle diameter (m)	0.01	0.01	0.01	0.01

Bleeder Outlet: static pressure defined 0 Pa

Return Outlet: static pressure defined 0 Pa

Main Inlet: total pressure defined 350 Pa

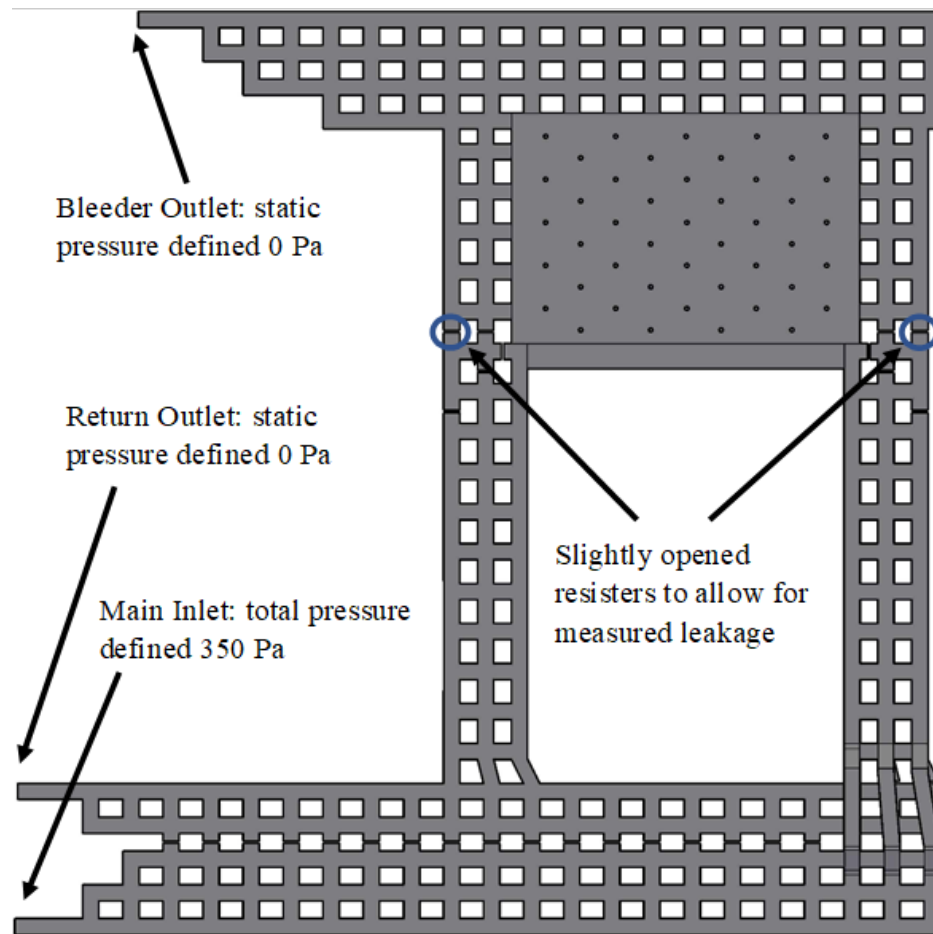Slightly opened resisters to allow for measured leakage

Figure 5-36: Model geometry and boundary conditions.

A total main-fan pressure of 350 pa was needed to create an intake airflow of 1.2 m³/min with the return and bleeder fan pressures set to be 0 Pa for the CFD model. Furthermore, the original assumed wall roughness of 0.0045 m was modified to 0.0043 m to match measured and simulated airflows. Table 5-6 shows the measured and simulated airflows at six locations, noted as red circles in Figure 5-37.
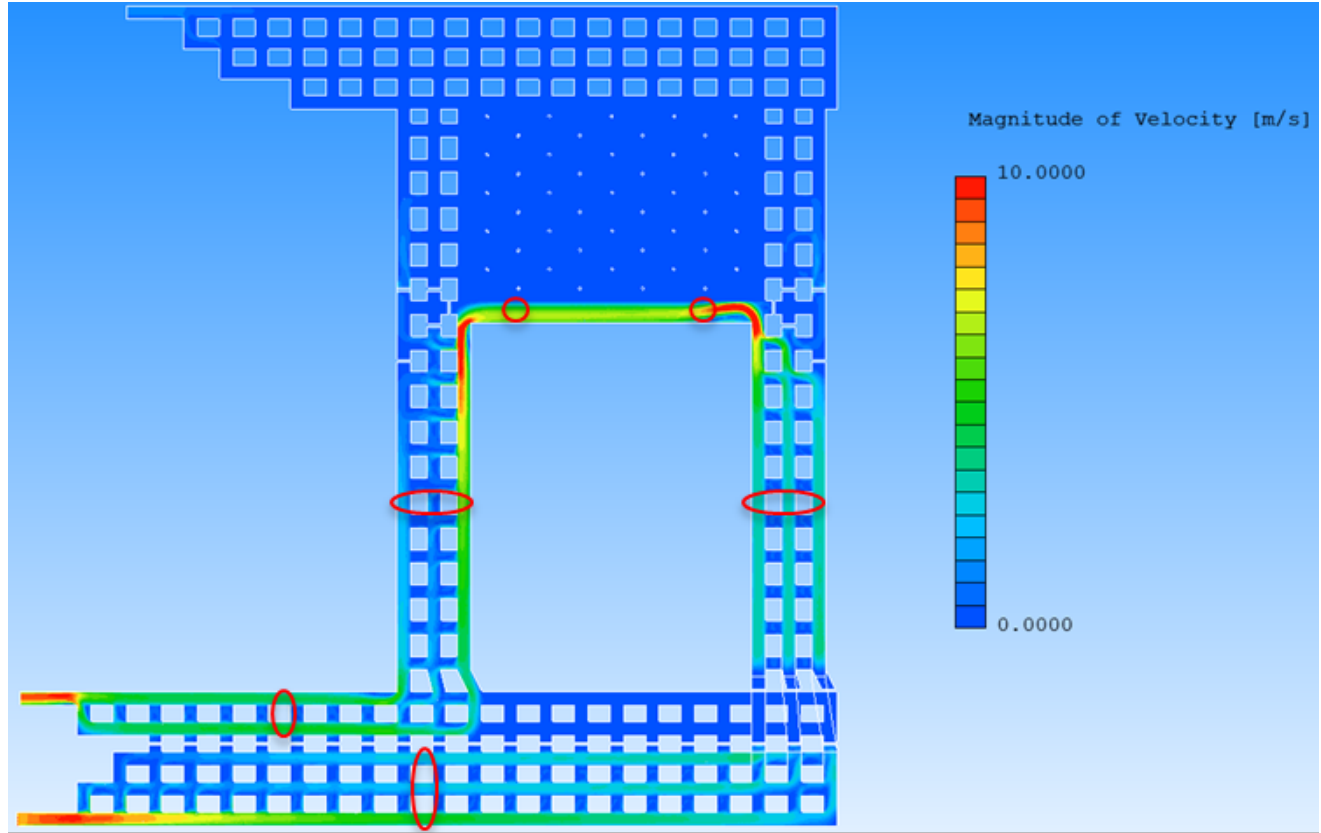

Figure 5-37: Velocity profile in U-tube ventilation scheme

Table 5-6: Results from U-Tube CFD simulation compared to the physical scaled model measurements

	Measured Airflow (Q, m³/min)					
	Intake	**Headgate**	**Face 1**	**Face 2**	**Tailgate**	**Return**
Measured Scaled Model	1.20	1.16	1.15	1.15	1.10	1.10
CFD	1.21	1.19	1.31	1.24	1.03	1.06
Relative Error	0.50%	2.4%	13.5%	7.5%	-6.5%	-4.0%

All velocity measurements taken in the model and CFD simulation were from a single measurement point (middle of the entry). Although, multi-point traverses provide a superior characterization of airflow, the size of the scaled model and complexity of the CFD simulation dictated that recovery at only a single point was feasible.

5.3.3 Gob and ventilation system interaction due to roof falls

The validated CFD model was used to study the complex interactions between the gob, bleeder and ventilation system for a simulated roof fall that interrupted the ventilation system. Although field example is available to confirm this response, the CFD model can nevertheless serve as a powerful tool to demonstrate its capability in predicting the complex ventilation response.
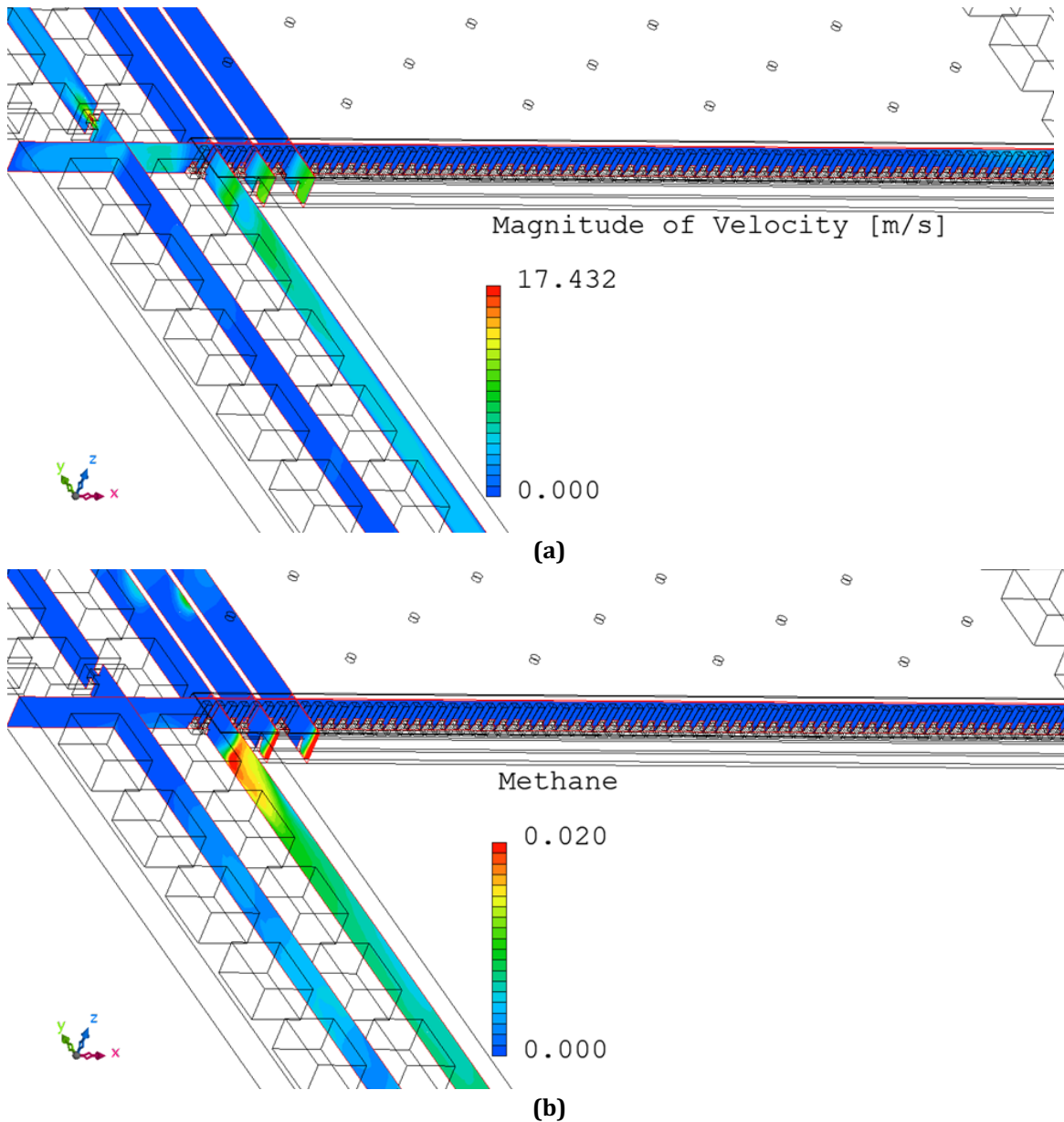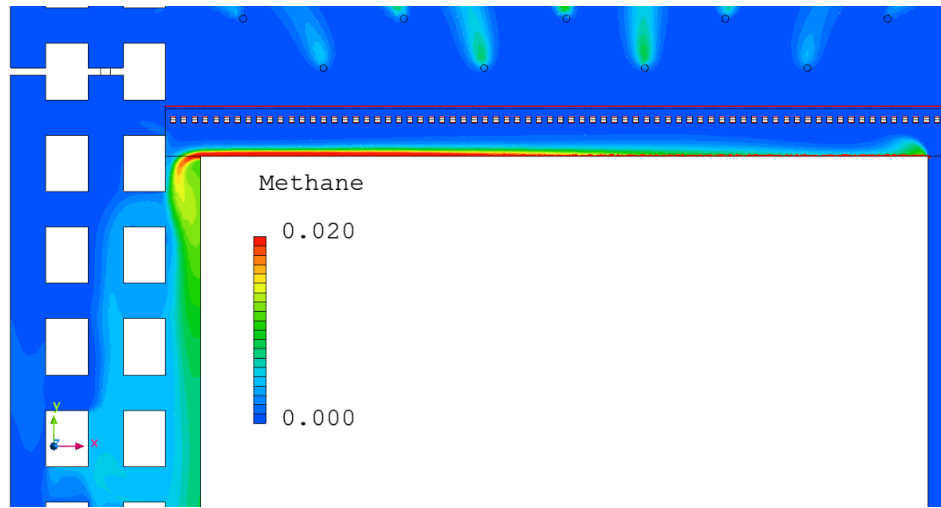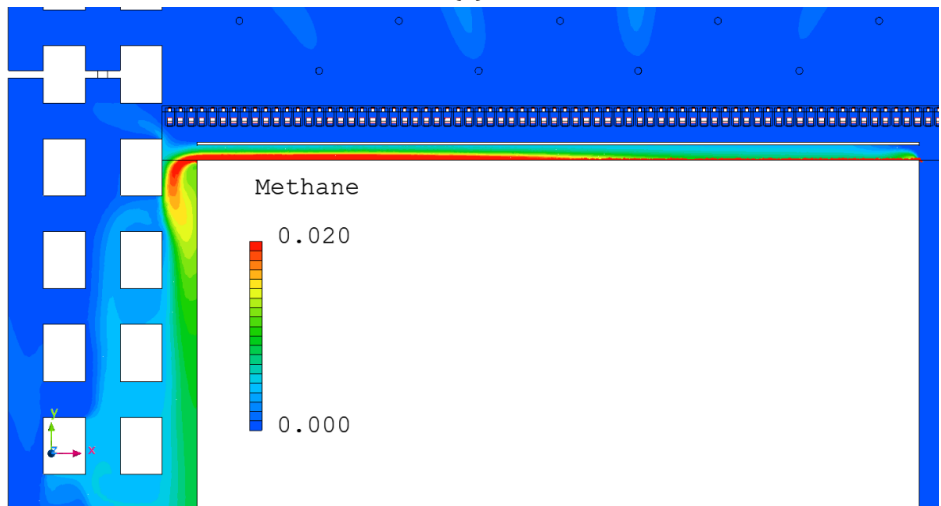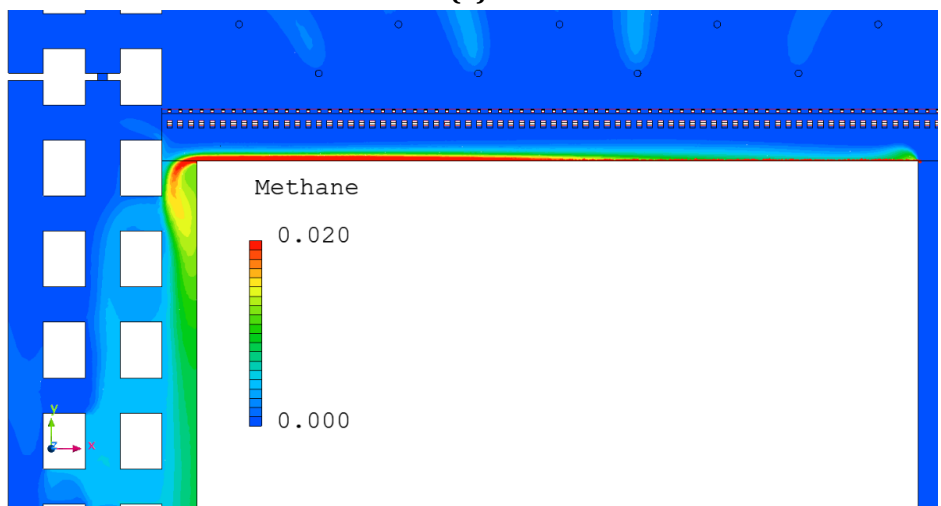

(a)

(b)

Figure 5-38: Baseline velocity and methane concentrations around tailgate corner: (a) Baseline velocity distributions; (b) Methane concentration distributions.

(a)

(b)

(c)

Figure 5-39: Baseline methane concentrations: (a) top 25%; (b) middle 50%; (c) bottom 75% of mining height.

Four roof fall scenarios were simulated in total, at three unique locations with the fourth combining all three locations, simultaneously. The baseline ventilation air velocity and methane concentration distributions at the face and tailgate corner are as shown in Figures 5-38. We examined vertical methane layering by sampling at three different elevations, from floor to roof. Figure 5-39 shows methane concentration distributions at quarter-, half- and threequarter-heights across the opening (25%, 50% and 75%). Methane layering is apparent with the upper portion of the mine opening exhibiting relatively higher buoyant gas concentrations, as shown in Figure 5-39.

For **Case #1**, the roof fall occurs in the entry closest to the panel as shown in Figures 5-40 and 5-41. As the baseline case, with most of the airflow and methane passing through this entryway, substantial differences in airflow patterns would be expected. Unexpectedly, significant changes in airflow patterns were not observed. However, methane concentration distributions were significantly different from the baseline case. This suggested that the roof fall reduced the intensity of the turbulence staunching methane dispersal. An elevated gas concentration was observed around the roof fall region. While the initial plume (before the roof fall) seems to have a much lower gas concentration relative to that after the roof fall. Also, this entry retains this elevated methane concentration much longer than the baseline simulation case. Comparing Figures 5-39 and 5-41, Figure 5-41 shows a lack of dispersion of the high methane concentration into the other entries - retaining a high concentration over a significant length of the entry. This excess mass will eventually distribute amongst the other entries but at a much later time compared to the baseline. This behavior may be attributed to the low air velocity near the roof fall region. Another concern is the recirculation that occurs in the middle entry. Two to three cross cuts outby the face, a recirculation airflow is apparent (Figure 5-41). A small mass of methane exits the third entry (containing the roof fall) and travels along the middle entry towards the tailgate bleeder. Over time this recirculation may result in a significant and hazardous methane buildup at the tailgate.
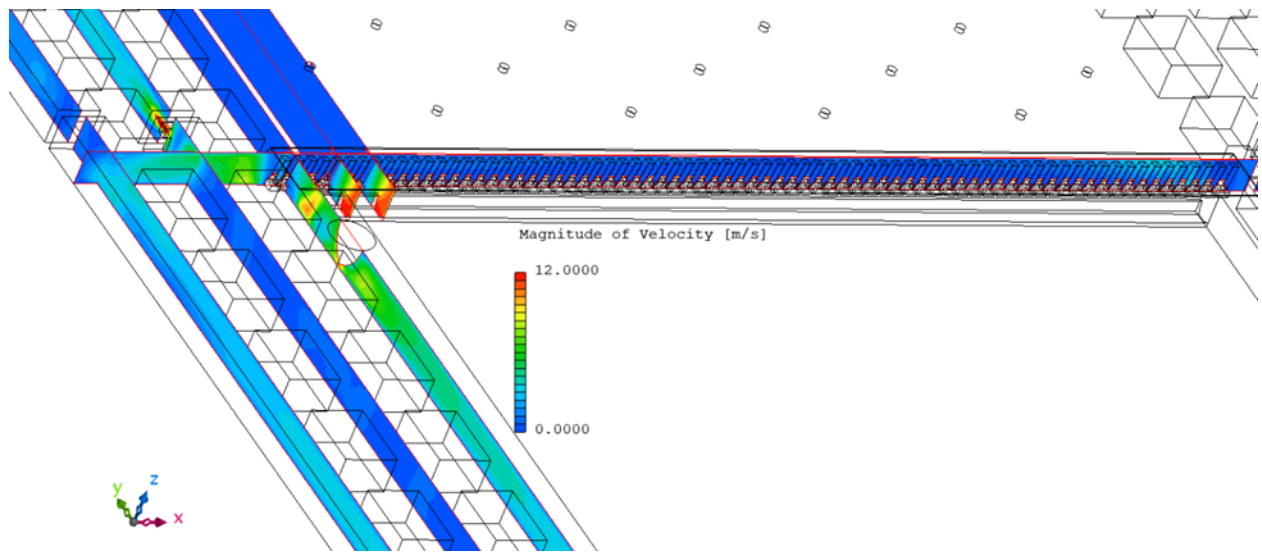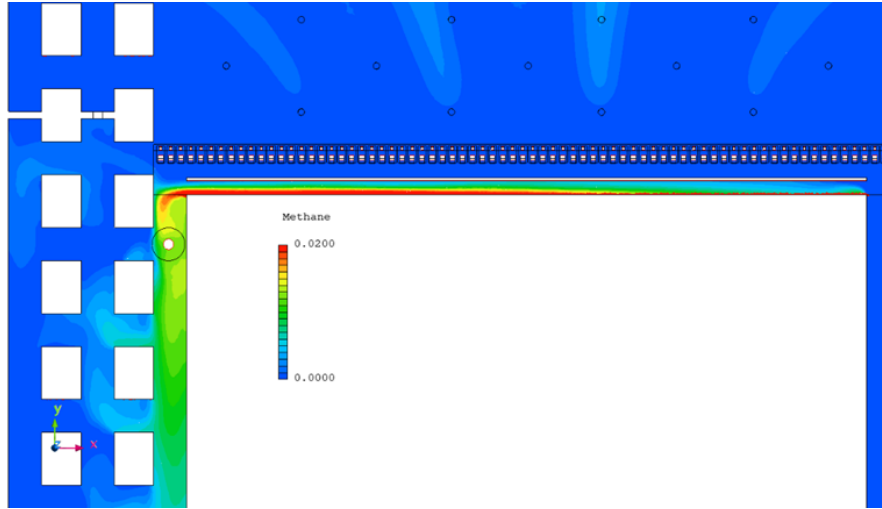
(a)
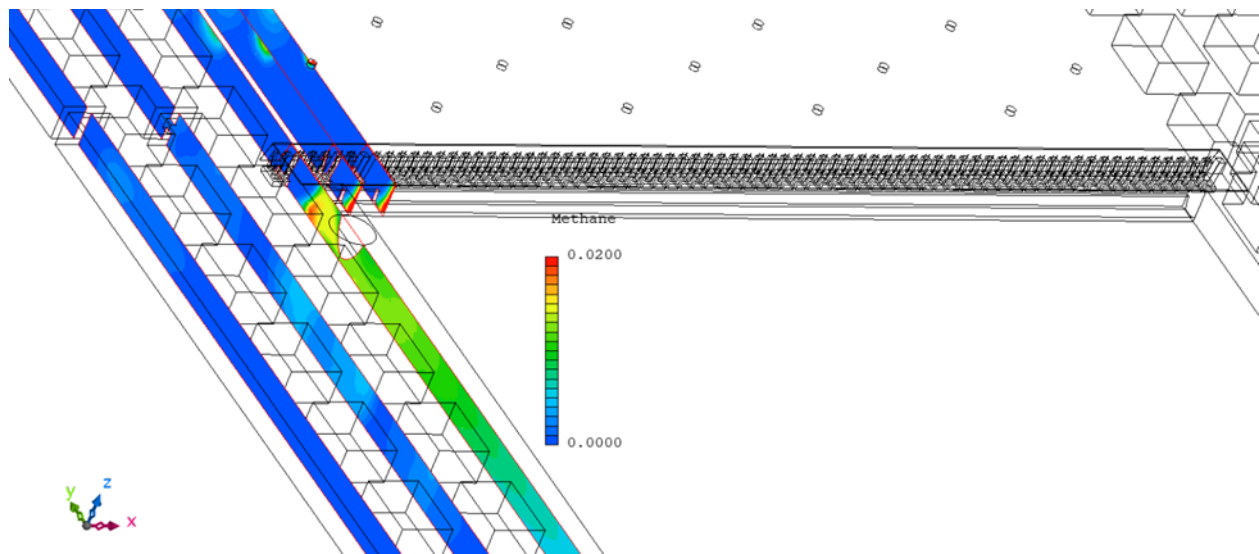
(b)

Figure 5-40: Velocity and methane concentrations around tailgate corner for RF1: (a) Velocity; (b) Methane concentration.

(a)

(b)

(c)

*Figure 5-40:*Methane concentrations: (a) top 25%; (b) middle 50%; and (c) bottom 75% of mining height for RF1.

For **Case #2**, the roof fall is applied in two cross cuts outby the tailgate regulator, as shown in Figures 5-42 and 5-43. Comparing Figure 5-39 and 5-43, the blockage causes minimal change in methane concentration in the third entry. However, the roof fall in this position significantly impacts the airflow distribution between all entries. This is indicated by null airflow mixing between the three entries as shown in Figure 5-43.
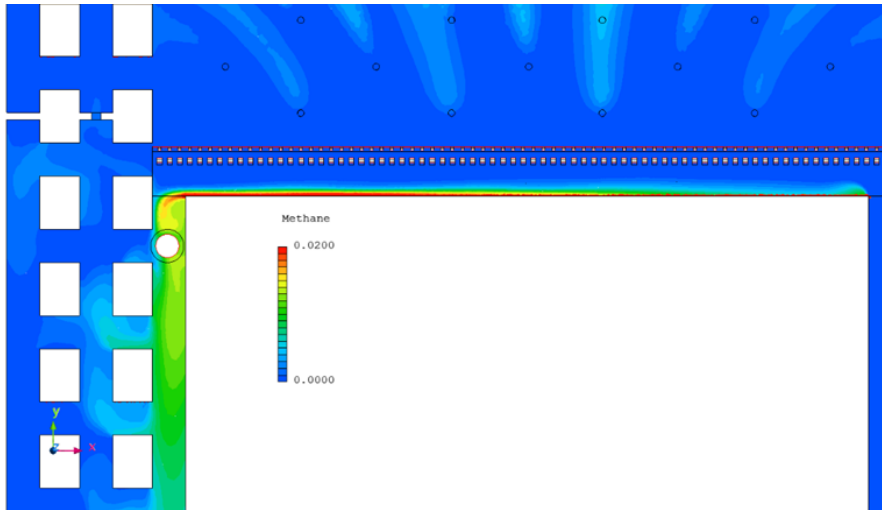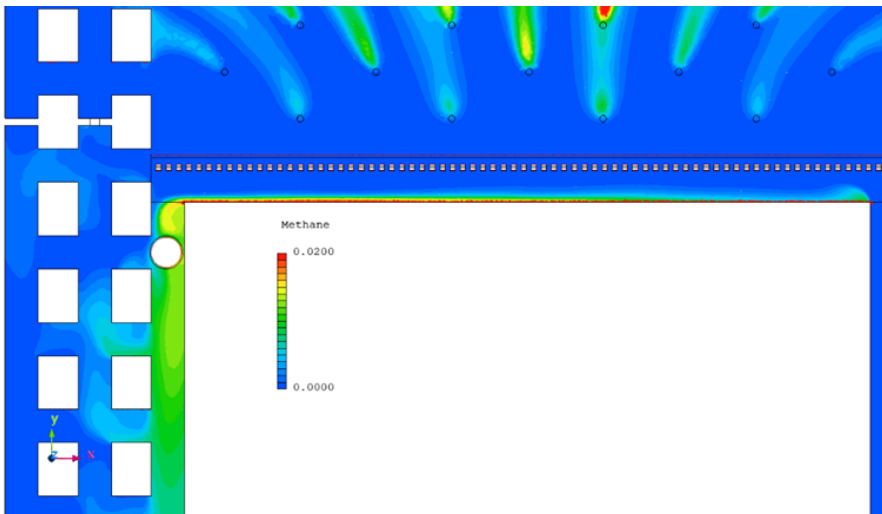

(a)

(b)

Figure 5-41: Velocity and methane concentrations around tailgate corner for RF2: (a) velocity; (b) methane concentration.

Figure 5-42: Methane concentrations: (a) top 25%; (b) middle 50% and (c) bottom 75% of mining height for RF2.

For **Case #3**, the roof fall is in the first crosscut outby the tailgate regulator. Surprisingly, a roof fall in this location does little to hinder airflow through the tailgate regulator. This is apparent from the velocity comparison in Figures 5-38 and 5-44. One other substantial insight is that

some methane build-up occurs in the crosscut ahead of the roof failure. This is expected however, but from the bottom panel of Figure 5-45, the buildup in the crosscut never exceeds 2% methane. However, with time, this methane accumulation could become hazardous.
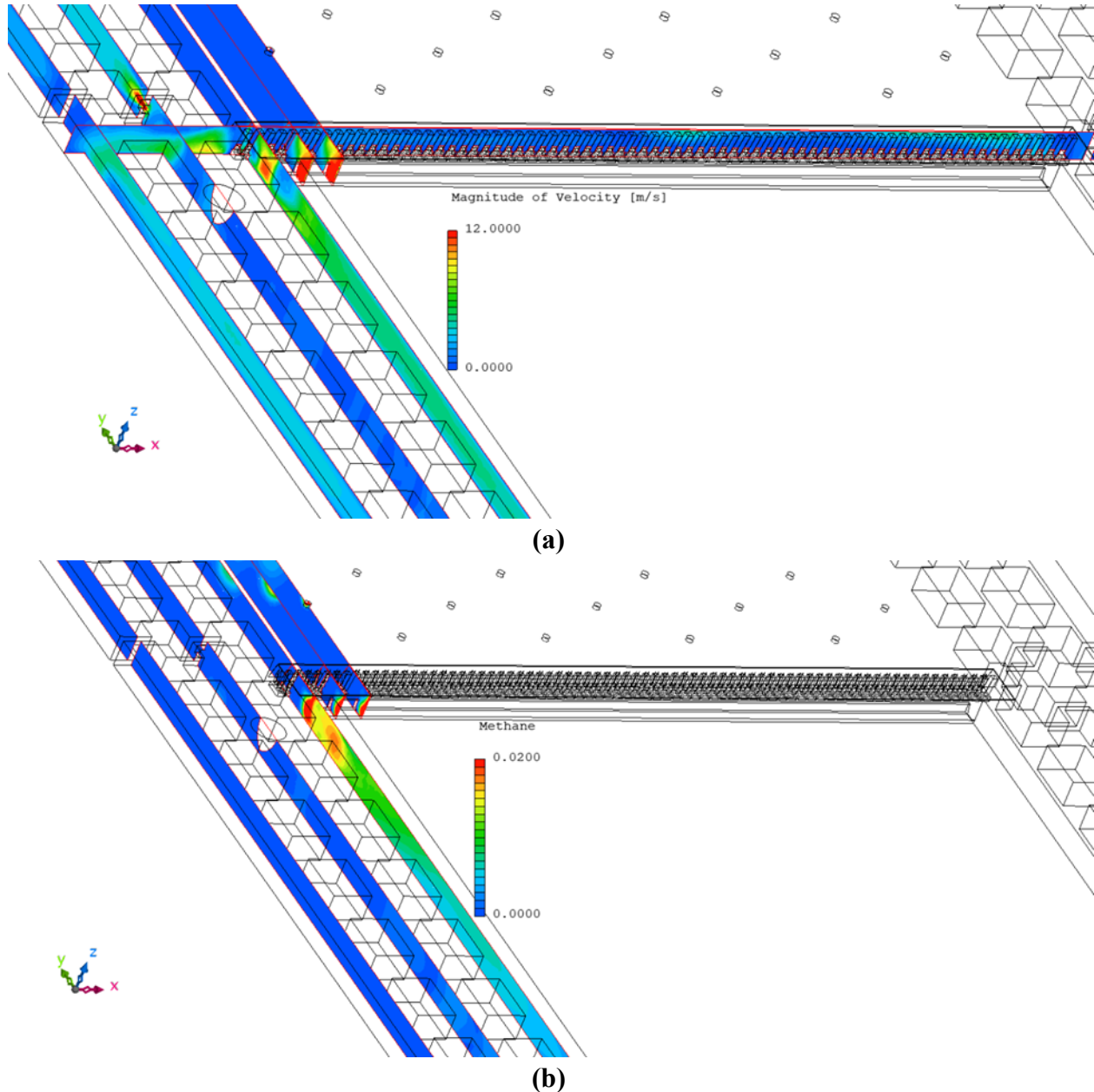

(a)

(b)

*Figure 5-43:*Velocity and methane concentrations around tailgate corner for RF3: (a) velocity; (b) methane concentration.
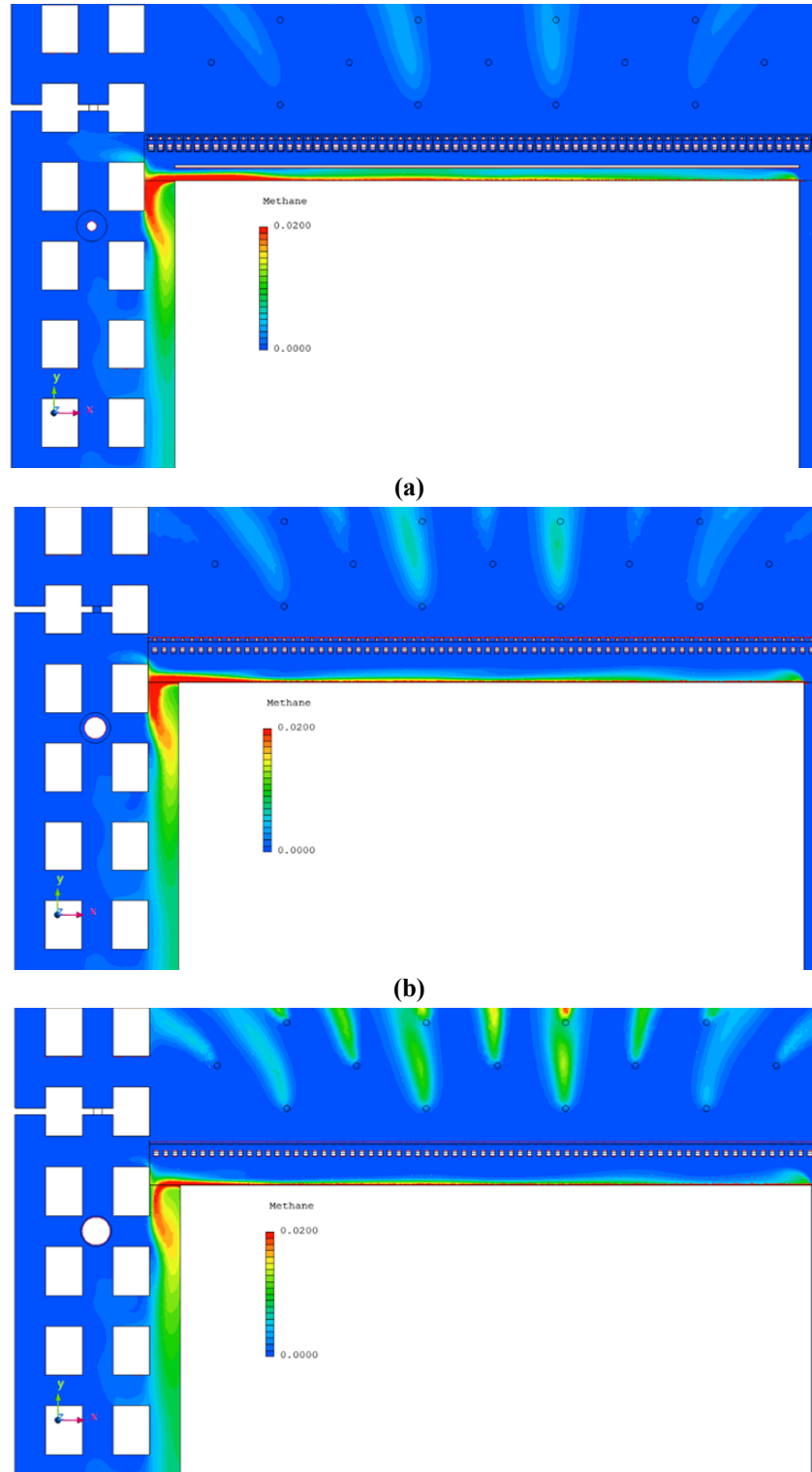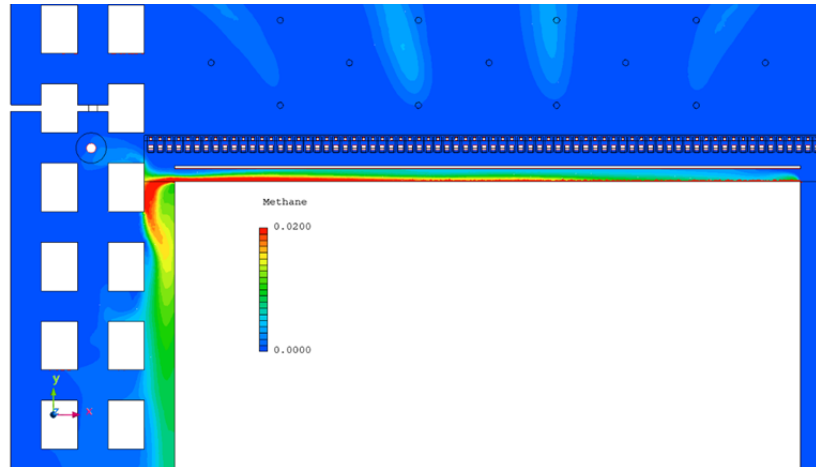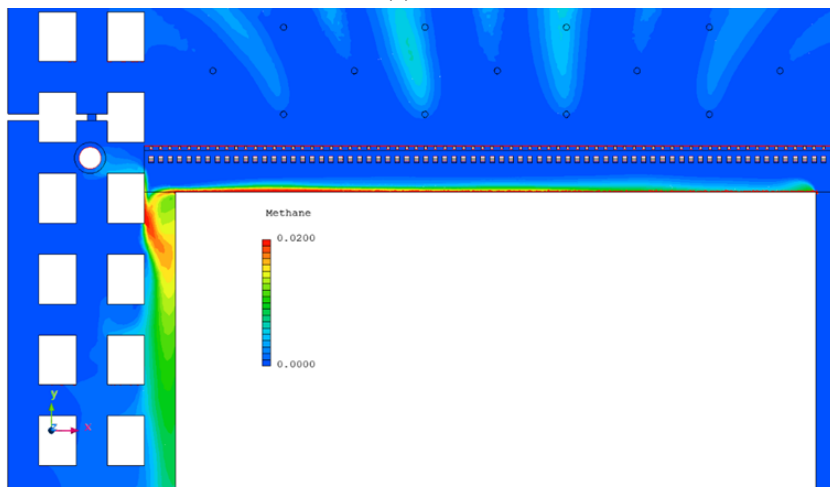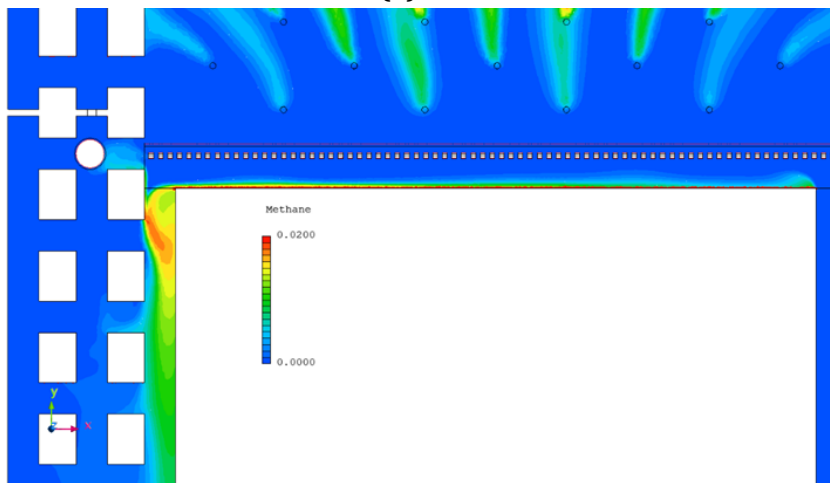
Figure 5-44: Methane concentrations: (a) top 25%; (b) middle 50% and (c) bottom 75% of mining height for RF3.

Finally, for **Case #4**, all three prior roof falls are assumed active/present. Influence on the ventilation system is shown in Figures 5-46 and 5-47. Methane build up and recirculation can clearly be seen in the third entry and the crosscut by the face. Compared to the baseline case,

significant areas/regions record methane concentrations >2%. This is expected, due to the significant cross-sectional blocked by the roof falls. Methane recirculation can also be seen in the top of the entryways in Figure 5-47. This scenario is the worst-case scenario among the prior three, and clearly shows low velocities and high methane concentrations throughout.
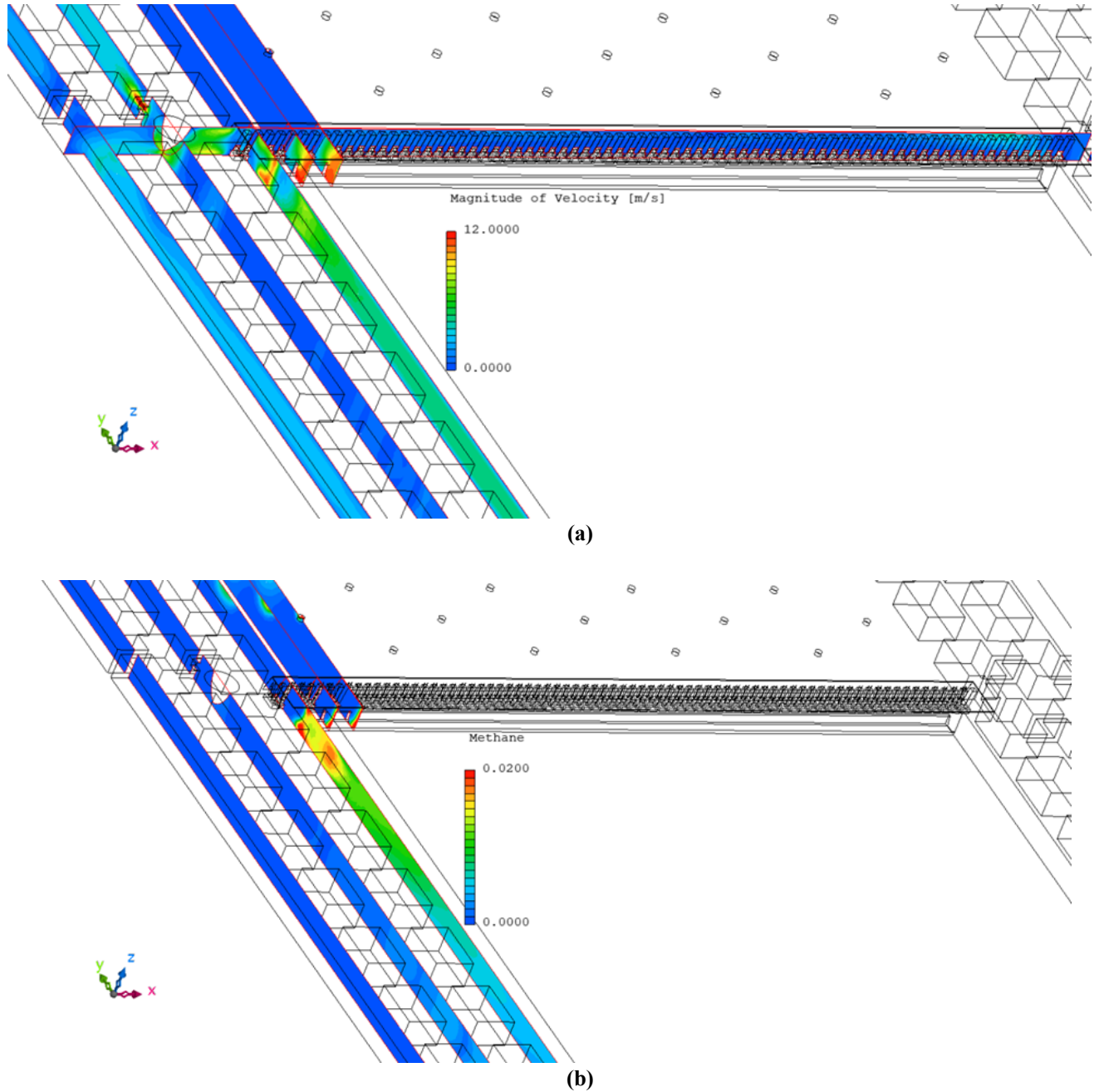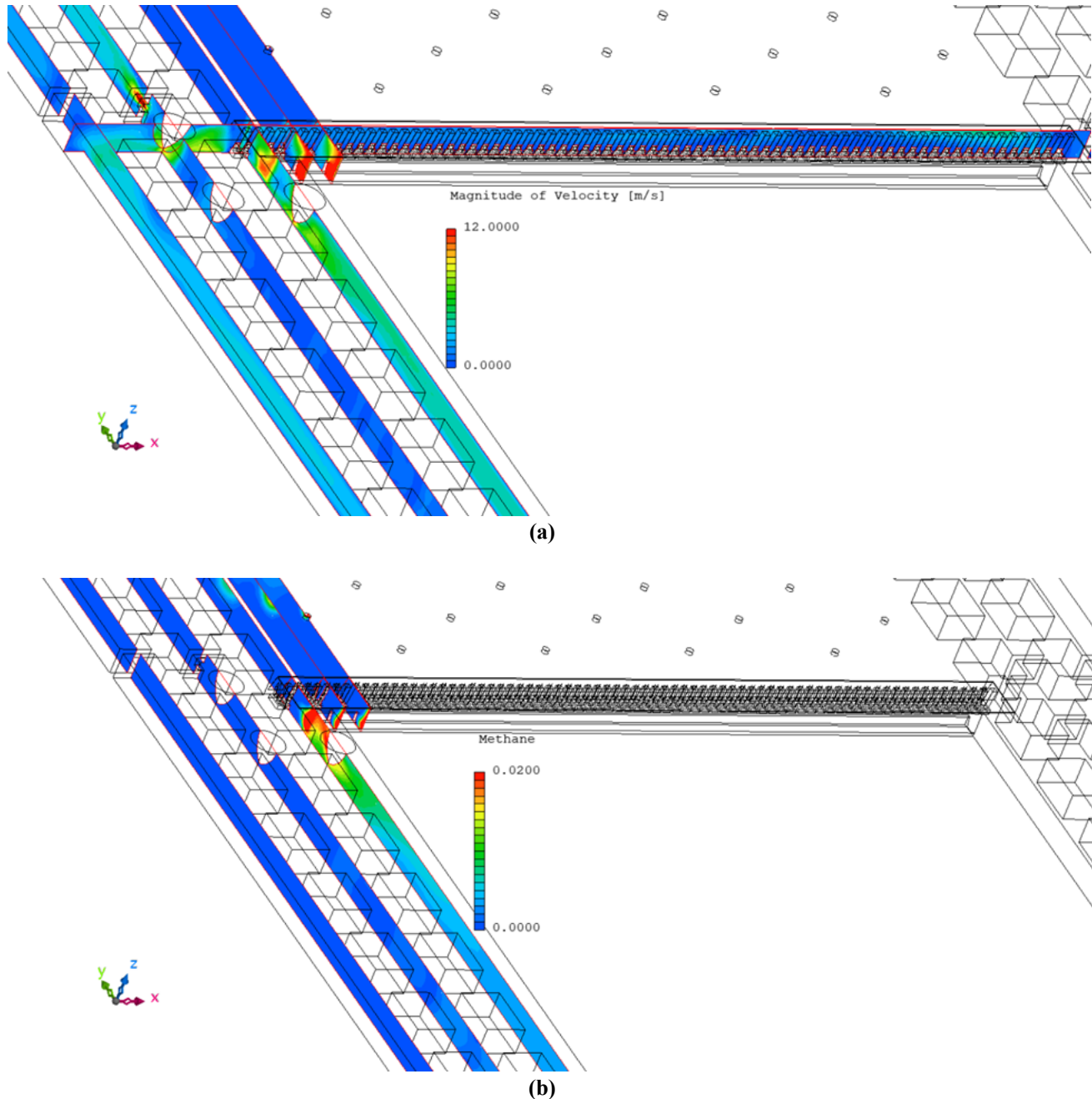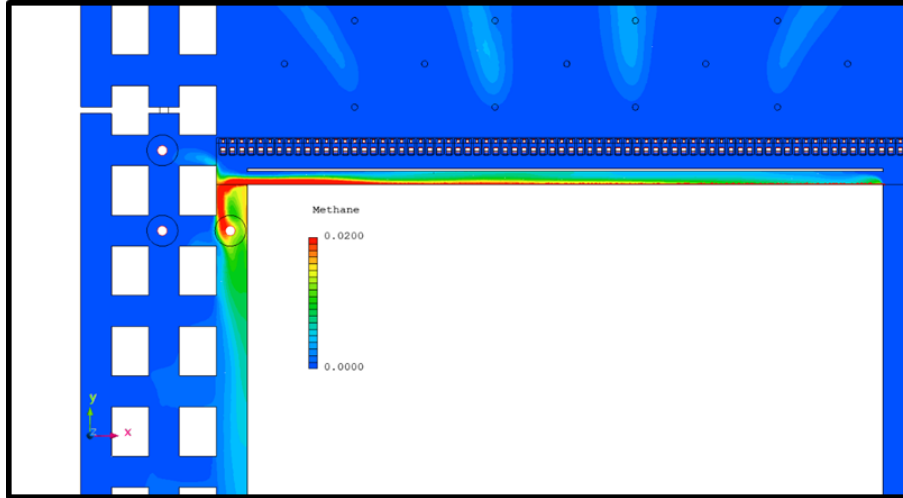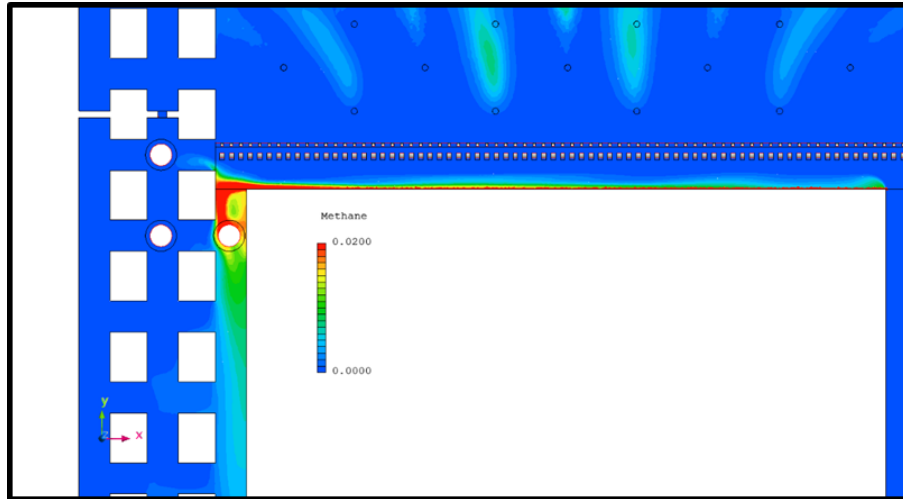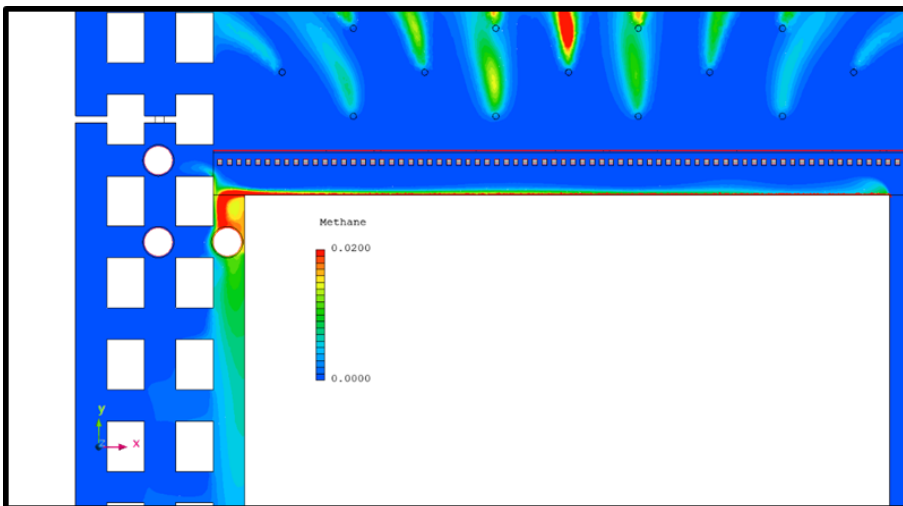

(a)

(b)

Figure 5-45: Velocity and methane concentrations around tailgate corner for all RF: (a) velocity; (b) methane concentration.

(a)

(b)

(c)

Figure 5-46: Methane concentrations: (a)top 25%; (b) middle 50% and (c) bottom 75% of mining height for all RF.

In summary, methane emissions from the gob to the ventilation system are significantly influenced by the local topology of network airways. Specifically, we use roof falls as just one proxy, capable of changing the resistance of airways near the tailgate entry, to evaluate impacts on gas emissions to the face. However, various other scenarios are of equal or potentially greater importance, including tailgate bleeder entry coverage and failure, the influence of tailgate regulator adjustment, variation in bleeder fan settings, together with many others.

6.0 Dissemination Efforts and Highlights

The research team used an integrated program of experiment, analytical modeling, numerical modeling and in-mine field measurement and validation to develop a systematic strategy to assess and predict the gas emission behavior from gob to the mine ventilation system. Based on the research outcome, we submitted two journal papers at top-rated journals - one paper has been published and the other one is currently under review. Also, one graduate student finished his M.S. thesis with support of this project. The team made a presentation annual SME conference at Denver in 2019.

The detailed information of the outcomes based on this project is listed as followings:

1. Liu A, Liu S, Wang G, Elsworth D. Predicting fugitive gas emissions from gob-to-face in longwall coal mines: Coupled analytical and numerical modeling. International Journal of Heat and Mass Transfer. 2020, 50:119392.

2. Liu A, Liu S, Wang G, Elsworth D. Continuous compaction and permeability evolution in longwall gob materials. Rock Mechanics and Rock Engineering. Under review. 2020

3. Gendrue NF, Liu S. Gas migration behavior near the longwall face and numerical simulations using PSU scaled model, 2019 annual SME conference, February 24-27, 2019, Denver, Colorado, United States.

4. Gendrue NF. Methane distribution and ventilation optimization for a scaled longwall mine with bleeder. Master thesis, Department of Energy and Mineral Engineering, The Pennsylvania State University, 2019.

In addition to the above publications, we have identified four venues for future presentations where these findings could receive widespread visibility (nationally and internationally). These venues include: (1) 2020 SME/PCMIA Annual Joint Meeting; (2) Illinois Mining Institute 2020 Annual Meeting; (3) 48th Annual West Virginia Mining Symposium; and (4) Future of Mining Australia 2020. Because these serve somewhat different audiences, there is the opportunity to further disseminate the findings to practitioners who might benefit from this work.

7.0 Conclusions and Impact Assessment

The overarching goal of this project was to develop appropriate strategies to characterize and model methane emission and transmission from the gob to the mine ventilation system and to effectively mitigate impacts of elevated methane concentrations for longwall mines. The flow behavior in the compacted gob zone was characterized and modeled using both experimental and analytical methods. This mechanistic model was then be applied to quantify and predict gas emission rates into the working face and ventilation system. A numerical study of gas emission from gob to the face was then conducted. Mine site measurements and campaign monitoring data were used to validate these models. The advanced knowledge gained through this research workflow is transformative as it provides a necessary, new and mechanism-based understanding of fluid storage and dynamics within the gob together with its transport to the working face. This study provides a systematic strategy to evaluate gas emissions at the working face and to control methane concentrations in longwall underground coal mines. Based on the obtained results, the following conclusions can be made:

7.1 Gob rock compaction behavior and permeability evolution modeling

Detachment of the undermined-roof into the gob leaves a loosely compacted perimeter that skirts the longwall panel. This permeable perimeter is "O-shaped" in plan-view and forms as a result of shear separation from the rib support. This detachment, together with the resulting rotated and reduced stresses, limit compaction, elevate permeability and exert significant control on gas flow during active longwall mining operations. We report gob compaction experiments using in-mine collected rock fragments stacked coarsening-upwards but capped in different modes – both without (Test A) and then with (Test B) a top layer of coarse material. We use a model of the observed compaction behavior to define permeability evolution, in particular, identifying a permeable ring that skirts the compacted gob. The following specific conclusions are drawn:

- Load-deformation experiments (A&B) define volumetric compaction/gas flow behaviors for scaled longwall gob material. Experiments are conducted in two modes, A and B. As applied uniaxial stress increases from 0 to ~ 1953 kPa (A) (~1592 kPa (B)) the porosity decreases from 0.64 to 0.41(~36%) for the uniform stacked material (A) but only from 0.66 to 0.51 (~23%) where the gob is topped with a layer of coarse "roof" rock simulants (B).
- The gob evolves with an initial highly compactive response where particulate readjustment dominates the response, followed by a stiffer response that is near linear between stress and strain. For the continuously coarsening-upwards gradations of both Test A and Test B, the strains of ~0.25 and ~0.17 are the thresholds to elastic responses at average stresses of ~ 0.38 MPa and ~ 0.41MPa respectively. The maximum strains for Test A and Test B are

~0.39 and ~0.30, corresponding to the maximum stresses of ~1.95 MPa and ~1.59 MPa, respectively, during the second load cycle.

- A loosely compacted "O-shaped" zone develops around the gob as a result of shear collapse and associated shear resistance at the rib support. This zone comprises a skirting ring of elevated permeability and controls gas flow both in and adjacent to the gob and significantly impacts longwall mining operations.

- A new predictive permeability model incorporates the deformation characteristics of the compacting gob and the size distribution of the component blocks, enabling the known redistribution of stresses to define permeability evolution. Based on this model, predicted permeabilities on shales (A&B) and sandstone (C&D) gob materials decrease, respectively, from 0.0031 cm^2 to 4.18×10^{-5} cm^2 (Test A), from 0.0215 cm^2 to 4.98×10^{-4} cm^2 (B), from 0.0066 cm^2 to 2.87×10^{-4} cm^2 (C), and from 0.011 cm^2 to 4.58×10^{-4} cm^2 (D) as the loading stress increases from 3.40 to 18.68 MPa.

7.2 Prediction of fugitive gas emissions from gob-to-face in longwall coal mines

Gas emissions from the gob, conditioned by the prior observations of Section 7.1, are systematically linked to the mine-wide ventilation system. Gas generation and transport from the gob represents the rate-limiting mechanisms and is idealized as desorption from a packed bed. This source region is linked to the numerical simulation of gas flow within the mine. These models are constrained by field measurements and used in predictions of methane concentration for various plausible and worst-case methane emission scenarios. The following specific conclusions are drawn:

- A pressure-gradient-driven model represents gas flow in the rock-coal blocky-aggregate representing the gob as a packed bed. The model describes the gas pressure drop for a mixed rock-coal porous aggregate, comprising viscous energy losses from tortuous flow in pore channels together with kinetic energy (inertial) losses within irregular cross-sections.

- Based on material balance, the ventilation air face pressure can significantly influence the gas emission behavior. The higher the face ventilation pressure, the less methane emission from gob to face. The face ventilation pressure is a function of barometric pressure and face operating conditions, future study should be conducted to detail how the face ventilation pressure varies with the barometric pressure.

- A field campaign of methane monitoring was conducted at the #6304 working face of the Tangkou mine in Shandong province, China. The measured methane concentration increases monotonically and almost linearly from headgate to tailgate. This finding is anticipated since the methane is largely emitted at a uniform rate along the face with this accumulation building along the longwall panel face from headgate to tailgate. The average methane emission rates are estimated as 0.0061m^3/s for the widest portion of the panel,

0.0044m^3/s at the transition width, and 0.00215m^3/s for the narrowest part of the panel, respectively. These estimates rely on and are conditioned by the linearly increasing trend observed from headgate to tailgate.

- A constitutive model is developed to evaluate gas emission from the gob that couples pressure gradient and diffusive generation and transport mechanisms. This relation was then used to study the case of longwall top-coal caving (LTCC) mining. The average gas emission rate was defined from the transient gas emission rates based on simulations – which agreed well with field observations.

- The porosity and effective permeability of the rock-coal block medium is determined by the size distributions of the rock-coal blocks in the gob and the fragmentation fractal dimension, which in turn significantly affect gas emission rates. An increment of applied stress results in a decrease in porosity, which will result in a further decrease in gas emission rate. An eleven-fold increase in stress (1.70MPa to 18.68MPa) results in a nonlinear decrease in porosity of only ~75% (from 0.368 to 0.093) but a 56-fold reduction in gas emission rate (compared to the maximum transient gas emission rate).

- A mine-wide ventilation pressure and flow quantity (p-Q) survey was conducted. The resulting survey data were used to build and constrain ventilation network modeling.

- The mine-wide ventilation system is especially sensitive to methane emission rates – a 50% increase in emission rate (from 0.00455 m^3/s to 0.00637 m^3/s) clearly impacts concentrations in the return branches. Peak methane concentration at related branches increase 39.7%, from 2.24% to 3.13% with the potential to trigger elevated methane alarms.

7.3 CFD modeling of interactions among compacted gob, bleeder, ventilation system

A suite of CFD models representing non-uniform airflows in roadways and panels were created and validated against the PSU physical scaled model. The validated model was used to simulate various scenarios to determine the influence of the ventilation to changes in the effectiveness of the methane dilution near the face and bleeder system. This was used to develop a comprehensive understanding of how the ventilation system responds to incidents that interrupt ventilation. The following specific conclusions are drawn:

- A physical scaled model ventilation system was fully developed to explore key parameters (pressure and velocity) controlling the response of ventilation in a combined longwall and bleeder system.

- A CFD model was validated against this physical scaled model. The CFD modeled results were congruent with the experimental data, demonstrating the utility of both methods in improving our understanding of interactions of the ventilation and bleeder system.

- CFD modeling is a powerful tool to rapidly assess the complexities of circulation, eddying, and sweep within the wide, irregular and open geometries of typical coupled gob, longwall and bleeder ventilation systems.

- Methane emission from the gob to the ventilation system is significantly influenced by the local arrangement of airways. The representation of roof fall blockage, as just one example of a feasible ventilation disruption, illustrates the sensitivity of the entire system to a change in resistance of airways near the tailgate entry. Different roof fall scenarios significantly influence gas dispersion and distribution in and around the tailgate region.

8.0 Recommendations for Future Work

Analytical and numerical tools have been developed to define the complex gas emission and transport behavior, both within the gob and discharged into the ventilation system. Specifically, these include (i) characterizations of gob creation, compaction, permeability evolution and gas generation validated against observations from LTCC panels, (ii) observation and characterization of gob-perimeter transport models, validated against compaction experiments utilizing LTCC scaled gob materials and (iii) analysis of a subset of ventilation-interruption scenarios and routine gas mitigation methods explored *via* scaled network and CFD models. These tools are ready for implementation.

Key remaining uncertainties relate to: (i) confirming gas generation and permeability evolution configurations and magnitudes specifically for US strata and longwall configurations, (ii) validating rate-limiting gas emission rates from the gob against US longwall configurations, and in (iii) extending these confirmations to examine routine gas mitigation strategies together with an extended array of critical ventilation interruption outcomes and hazards.

In particular, a demonstration project in a US operating mine would serve to integrate these tools and confirm the utility of current LTCC observations to US longwall operations. In addition, this demonstration project would serve as a vehicle to explore and to resolve key remaining questions.

The following research directions would extend the scope of this project and provide new understanding and technical tools for effective gas control and hazard mitigation in the US underground coal industry.

1. Define the detailed geometry of the caved gob in US coal mines considering the specific strength and stratigraphy of the roof strata and the detachment of the undermined-roof into the gob. Define the form and extent of the loosely compacted perimeter that skirts the longwall panel, and confirm predictions of permeability evolution, extent and impacts on

gas transmission from gob-to-face. Define gob material particle size distributions (PSDs), using Lidar and optical imaging and utilize discrete element models (DEM) to reconstruct heterogeneous block distributions, to be recreated at lab-scale for compaction and permeability measurement, then up-scaled to mine-scale for subsequent CFD modeling.

2. Provide independent direct confirmation of measured compaction response and missing permeability evolution for US gob materials to supplement current compaction response experiments for scaled LTCC gob materials – where permeability evolution of the caved rock has not been independently validated. This is especially crucial in the gob-center where low permeabilities are the rate limiting transport mechanism, controlling gas emission to the skirting panel ring (of high permeability gob), and where the presence of this permeable skirt both increases the length of the tributary source area and its efficiency in transporting methane to the face and bleeder. Measurements of desorption rates and permeability on PSD-scaled samples of US gobs would provide new and compelling data to bridge this crucial knowledge gap.

3. Extend the current suite of modeling tools and newly constrained understanding of compaction and permeability evolution response to explore the effectiveness of current and novel gas mitigation methods in optimizing production and minimizing hazard. These tools would be used to investigate how gob vent boreholes influence overall gas emission from gob to the face and bleeders.

4. Up-scaling CFD modeling (field scale) to define key interactions among the gob, primary ventilation system and bleeder system. The current study explores LTCC mining, specifically without the bleeder system present in US longwall mines – limiting the direct utility of field monitored results in inferring how the bleeder system influences overall gas emission near the face. CFD modeling would specifically enable the impact of a bleeder system to be evaluated.

9.0 References

1. Fan L, Liu S. A conceptual model to characterize and model compaction behavior and permeability evolution of broken rock mass in coal mine gobs. *Int J Coal Geol*. 2017;172:60-70.
2. Coal Age. U.S. Longwall Operations: How Slow Can We Go? *Coal Age*. 2017:26-32.
3. Du X, Peng S, Lawall CE. Coal Pillar Loading Mechanisms and Progress in Pillar Design. In: *27th International Conference on Ground Control in Mining*; 1998:254-261.
4. Ren T, Wang Z, Liang Y, Zhang J. Numerical investigation of CO_2 fringe behaviour on a longwall face and its control. *Int J Coal Geol*. 2018;186(December 2017):80-96.
5. Zhang C, Tu S, Zhang L. Analysis of Broken Coal Permeability Evolution Under Cyclic Loading and Unloading Conditions by the Model Based on the Hertz Contact Deformation

Principle. *Transp Porous Media*. 2017;119(3):739-754.

6. Karacan CÖL. Stochastic modeling of gob gas venthole production performances in active and completed longwall panels of coal mines. *Int J Coal Geol*. 2010;84(2):125-140.

7. Esterhuizen, G.S., Karacan CO. A Methodology for Determining Gob Permeability Distributions and its Application to Reservoir Modeling of Coal Mine Longwalls. *SME Annu Meet Exhib Denver, Color*. 2007:6.

8. Karacan CO. Prediction of porosity and permeability of caved zone in longwall gobs. *Transp Porous Media*. 2010;82:413-439.

9. Schatzel, S., Karacan, C., Krog, R., Esterhuizen, G., Goodman G. Guidelines for the Prediction and Control of Methane Emissions on Longwalls. 2008.

10. Karacan CÖ. A new method to calculate permeability of gob for air leakage calculations and for improvements in methane control. *Proc 13th US/North Am Mine Vent Symp*. 2010.

11. Whittles DN, Lowndes IS, Kingman SW, Yates C, Jobling S. Influence of geotechnical factors on gas flow experienced in a UK longwall coal mine panel. *Int J Rock Mech Min Sci*. 2006;43(3):369-387.

12. Zhang C, Tu S, Zhang L, Bai Q, Yuan Y, Wang F. A methodology for determining the evolution law of gob permeability and its distributions in longwall coal mines. *J Geophys Eng*. 2016;13(2):181-193.

13. McAteer, J. Davitt. Beall, K., Beck, James A. McGinley, Patrick C. Monforton, Celeste. Roberts, Deborah. Spence, Beth Weise, S. Upper Big Branch - Report to the Governor's Independent Investigation Panel, Office. 2010.

14. Page, N.., Watkins, T.R., Caudill, S.D., Cripps, D.R., Godsey, J.F., Maggard, C.J., Moore, A.D., Morley, T.A., Phillipson, S.E., Sherer, H.E., Steffey, D.A., Stephan, C.R., Stoltz, R.T., Vance JW. Report of Investigation - Fatal Underground Mine Explosion. 2010.

15. Alehossein H, Poulsen BA. Stress analysis of longwall top coal caving. *Int J Rock Mech Min Sci*. 2010;47(1):30-41.

16. SS P. *Coal Mine Ground Control. 3rd Ed*. United States: Society for Mining, Metallurgy, and Exploration; 2008.

17. Karacan CÖ. International Journal of Coal Geology Forecasting gob gas venthole production performances using intelligent computing methods for optimum methane control in longwall coal mines. *Int J Coal Geol*. 2009;79(4):131-144.

18. Karacan CÖ. International Journal of Coal Geology Reconciling longwall gob gas reservoirs and venthole production performances using multiple rate drawdown well test analysis. *Int J Coal Geol*. 2009;80(3-4):181-195.

19. Karacan CÖ. Prediction of porosity and permeability of caved zone in longwall gobs. *Transp Porous Media*. 2010;82(2):413-439.

20. Karacan CÖ, Esterhuizen GS, Schatzel SJ, Diamond WP. Reservoir simulation-based modeling for characterizing longwall methane emissions and gob gas venthole production. *Int J Coal Geol*. 2007;71(2-3):225-245.

21. Zhang C, Zhang L. Permeability Characteristics of Broken Coal and Rock Under Cyclic Loading and Unloading. *Nat Resour Res*. 2019;28(3):1055-1069.

22. Zhu W, Li S, Niu L, Liu K, Xu T. Experimental and Numerical Study on Stress Relaxation of Sandstones Disturbed by Dynamic Loading. *Rock Mech Rock Eng*. 2016;49(10):3963-3982.

23. Wang J, Elsworth D, Wu Y, Liu J, Zhu W, Liu Y. The Influence of Fracturing Fluids on Fracturing Processes: A Comparison Between Water, Oil and SC-CO2. *Rock Mech Rock Eng*. 2018;51(1):299-313.

24. Forster I, Enever J. Hydrogeological response of overburden strata to underground mining. *Off Energy Rep 1, p 104*. 1992.

25. Adhikary DP, Guo H. Modelling of Longwall Mining-Induced Strata Permeability Change. *Rock Mech Rock Eng*. 2014;48(1):345-359.

26. Arya LM, Paris JF. (1981) Physicoempirical Model to Predict the Soil Moisture Characteristic form Particle-Size Distribution and Bulk Density Data, A. 1981.

27. Wu J, Yu B, Yun M. A resistance model for flow through porous media. *Transp Porous Media*. 2008;71(3):331-343.

28. Sirivithayapakorn S, Keller A. Transport of colloids in saturated porous media: A pore-scale observation of the size exclusion effect and colloid acceleration. *Water Resour Res*. 2003;39(4).

29. Auset M, Keller AA. Pore-scale processes that control dispersion of colloids in saturated porous media. *Water Resour Res*. 2004;40(3).

30. Mortensen NA, Okkels F, Bruus H. Reexamination of Hagen-Poiseuille flow: Shape dependence of the hydraulic resistance in microchannels. *Phys Rev E - Stat Nonlinear, Soft Matter Phys*. 2005;71(5).

31. Rieu M, Sposito G. (1991) Fractal Fragmentation, Soil Porosity, and Soil Water Properties: I. Theory. 1991:1231-1238.

32. Zhao J, Yin L, Guo W. Stress–Seepage Coupling of Cataclastic Rock Masses Based on Digital Image Technologies. *Rock Mech Rock Eng*. 2018;51(8):2355-2372.

33. Esterhuizen G, Karacan C. A methodology for determining gob permeability distributions and its application to reservoir modeling of coal mine longwalls. 2007.

34. Stephenson D. Rockfill in hydraulic engineering. *Elsevier, Amsterdam*. 1979.

35. Hoek EBJ. Rock slope engineering (revised third edition). *Inst Min Metall London*. 1981.

36. Esterhuizen GS KC. Development of numerical models to investigate permeability changes and gas emission around longwall mining panel. *NIOSH Pittsburgh Res Lab Res Report,*. 2006:13.

37. Lowndes I, Reddish DJ, Ren T, Whittles DN, Hargreaves D. Improved modeling to support the prediction of gas migration and emission from active longwall panels. *Mine Vent*. January 2002:267-272.

38. Jozefowicz RR. The Post-failure Stress-permeability Behaviour of Coal Measure Rocks. phd thesis. *phd thesis Univ Nottingham*. 1997.

39. Karacan CÖ, Esterhuizen GS, Schatzel SJ, Diamond WP. Reservoir simulation-based modeling for characterizing longwall methane emissions and gob gas venthole production. 2007;71:225-245.

40. Zhang C, Tu S, Zhao Y. Compaction characteristics of the caving zone in a longwall goaf : a review. *Environ Earth Sci*. 2019;78(1):1-20.

41. Pappas, D.M., Mark C. Behavior of simulated longwall gob material. 1993.

42. Guo H, Adhikary DP, Craig MS. Simulation of mine water inflow and gas emission during longwall mining. *Rock Mech Rock Eng*. 2009;42(1):25-51.

43. Guo H, Todhunter C, Qu Q, Qin Z. Longwall horizontal gas drainage through goaf pressure control. *Int J Coal Geol*. 2015;150-151:276-286.

44. Liu A, Liu S, Wang G, Elsworth D. Predicting fugitive gas emissions from gob-to-face in longwall coal mines: Coupled analytical and numerical modeling. *Int J Heat Mass Transf*. 2020;150:119392.

45. Burke SP, Plummer WB. Gas Flow through Packed Columns1. 1928;20(11):1196-1200.

46. Yu B. Fractal Analysis of Permeabilities. 2004;50(1).
47. Mandelbrot BB. The Fractal Geometry of Nature, Freeman, New York,. 1982:23-117.
48. Liu S, Harpalani S. Determination of the effective stress law for deformation in coalbed methane reservoirs. *Rock Mech Rock Eng*. 2014;47(5):1809-1820.
49. Liu S, Harpalani S. Compressibility of sorptive porous media: Part 1. Background ana theory. *Am Assoc Pet Geol Bull*. 2014;98(9):1761-1772.
50. Kai W, Ang L, Aitao Z. International Journal of Mining Science and Technology Theoretical analysis of influencing factors on resistance in the process of gas migration in coal seams. *Int J Min Sci Technol*. 2017;27(2):315-319.
51. SS P. *Coal Mine Ground Control. 3rd Ed*. Englewood, United States: Society for Mining, Metallurgy, and Exploration; 2008.
52. Wang Jiachen. *The Theory and Technique on the Thick Coal Seam Mining*. Beijing: Metallurgical Industry Press; 2009.
53. Alehossein H, Poulsen BA. Stress analysis of longwall top coal caving. *Int J Rock Mech Min Sci*. 2010;47(1):30-41.
54. GC S. *Coal Mining in France*. Colliery Guardian; 1961.
55. Wang J, Yang S, Li Y, Wei L, Liu H. Caving mechanisms of loose top-coal in longwall top-coal caving mining method. *Int J Rock Mech Min Sci*. 2014;71:160-170.
56. Wold, M.B., Pala J. Aspects of support and strata performance on longwall no.1 at Ellalong Colliery. In: CSIRO division of geomechnics report no. 62; 1986.
57. Poulsen BA. Evaluation of software code UDEC for modelling top coal caving in an Australian environment. In: CSIRO exploration and mining report 1115F; 2003.
58. Xie GX, Chang JC, Yang K. Investigations into stress shell characteristics of surrounding rock in fully mechanized top-coal caving face. *Int J Rock Mech Min Sci*. 2009;46(1):172-181.
59. Xie H, Chen Z, Wang J. Three-dimensional numerical analysis of deformation and failure during top coal caving. *Int J Rock Mech Min Sci*. 1999;36(5):651-658.
60. Yasitli NE, Unver B. 3D numerical modeling of longwall mining with top-coal caving. *Int J Rock Mech Min Sci*. 2005;42(2):219-235.
61. Krog RB, Schatzel SJ, Garcia F, Marshall JK. Predicting methane emissions from longer longwall faces by analysis of emission contributors. *Proc 11th US/North Am Mine Vent Symp - 11th US/North Am Mine Vent Symp 2006*. 2006:383-392.
62. McAteer, J.D., Beall, K., Beck, J.A., McGinley, P.C., Monforton, C., Roberts, D.C., Spence, B., Weise S. No Title.
63. Gillies ADS. *Coal Mine Face Area Ventilation, Ventilation of Coal Mines, Proceedings of the Symposium*. Australasian Inst of Mining & Metallurgy, Illawarra Branch, Wollongong; 1983.
64. Parra MT, Villafruela JM, Castro F, Méndez C. Numerical and experimental analysis of different ventilation systems in deep mines. *Build Environ*. 2006;41(2):87-93.
65. Cheng J, Yang S. Data mining applications in evaluating mine ventilation system. *Saf Sci*. 2012;50(4):918-922.
66. El-Nagdy KA. Stability of multiple fans in mine ventilation networks. *Int J Min Sci Technol*. 2013;23(4):569-571.
67. Kazakov BP, Shalimov A V., Semin MA. Stability of natural ventilation mode after main fan stoppage. *Int J Heat Mass Transf*. 2015;86:288-293. doi:10.1016/j.ijheatmasstransfer.2015.03.004
68. Wang K, Wu Z, Zhou A, Jiang Y, Feng S. Experimental study of high concentrations of coal

mine methane behavior in downward ventilated tilted roadways. *J Wind Eng Ind Aerodyn*. 2016;158(January):69-80.

69. Karacan CÖ, Esterhuizen GS, Schatzel SJ, Diamond WP. Reservoir simulation-based modeling for characterizing longwall methane emissions and gob gas venthole production. *Int J Coal Geol*. 2007;71(2-3):225-245.

70. Brunner DJ. Ventilation models for longwall leakage simulation. In: Reno,NV: 2nd US Mine Ventilation Symposium; 1985:23-25.

71. Esterhuizen GS, Karacan CO. Development of numerical models to investigate permeability changes and gas emission around longwall mining panel. *Am Rock Mech Assoc - 40th US Rock Mech Symp ALASKA ROCKS 2005 Rock Mech Energy, Miner Infrastruct Dev North Reg*. 2005.

72. Zhang C, Tu S, Zhang L, Bai Q, Yuan Y, Wang F. A methodology for determining the evolution law of gob permeability and its distributions in longwall coal mines. *J Geophys Eng*. 2016;13(2):181-193.

73. Jozefowicz RR. The post-failure stress-permeability behaviour of coal measure rocks. 1997.

74. Esterhuizen GS, Karacan CÖ. A Methodology for Determining Gob Permeability Distributions and its Application to Reservoir Modeling of Coal Mine Longwalls. *SME Annu Meet Exhib*. 2007;(1980):6.

75. Ergun S, Orning AA. Fluid Flow through Randomly Packed Columns and Fluidized Beds. *Ind Eng Chem*. 1949;41(6):1179-1184.

76. Vafai K, Tien CL. Boundary and inertia effects on flow and heat transfer in porous media. *Int J Heat Mass Transf*. 1981;24(2):195-203.

77. Demirel Y, Kahraman R. Thermodynamic analysis of convective heat transfer in an annular packed bed. *Int J Heat Fluid Flow*. 2000;21(4):442-448.

78. Khaled ARA, Vafai K. The role of porous media in modeling flow and heat transfer in biological tissues. *Int J Heat Mass Transf*. 2003;46(26):4989-5003.

79. Hicks RE. Pressure Drop in Packed Beds of Spheres. *Ind Eng Chem Fundam*. 1970;9(3):500-502.

80. Niven RK. Physical insight into the Ergun and Wen and Yu equations for fluid flow in packed and fluidised beds. *Chem Eng Sci*. 2002;57(3):527-534.

81. Ergun S. *Fluid Flow through Packed Columns*. Chem. Eng. Prog.; 1952.

82. Zhang Y. *Fluid Mechanics, Chap (3, 6)*. Higher Education Press; 1999.

83. Saghafi A, Faiz M, Roberts D. CO2 storage and gas diffusivity properties of coals from Sydney Basin, Australia. *Int J Coal Geol*. 2007;70(1-3 SPEC. ISS.):240-254.

84. Liu J, Chen Z, Elsworth D, Miao X, Mao X. Evaluation of stress-controlled coal swelling processes. *Int J Coal Geol*. 2010;83(4):446-455.

85. Shi JQ, Durucan S, Fujioka M. A reservoir simulation study of CO2injection and N2flooding at the Ishikari coalfield CO2storage pilot project, Japan. *Int J Greenh Gas Control*. 2008;2(1):47-57.

86. Chen D, Pan Z, Liu J, Connell LD. An improved relative permeability model for coal reservoirs. *Int J Coal Geol*. 2013;109-110:45-57.

87. B. Abbasi , Y.P. Chugh HG. An analysis of the possible fault displacements associated with a retreating longwall face in Illinois. *48th US Rock Me- chanics/Geomechanics Symp 1-4 June, Minneapolis, Minnesota*. 2014.

88. PM. How Permeability Depends on Stress and Pore Pressure in Coalbeds: A New Model.

89. Liu S, Harpalani S. Permeability prediction of coalbed methane reservoirs during primary

depletion. *Int J Coal Geol*. 2013;113:1-10. 0

90.   Cheng J, Li S, Zhang F, Zhao C, Yang S, Ghosh A. CFD modelling of ventilation optimization for improving mine safety in longwall working faces. *J Loss Prev Process Ind*. 2016;40:285-297.

91.   Bird, R.B., Stewart, W.E., Lightfoot EN. *Transport Phenomena, Chap 6.* Wiley, New York; 1960.

92.   Langmuir I. The constitution and fundamental properties of solids and liquids. II. Liquids. *J Am Chem Soc*. 1917;39(9):1848-1906.

10.0 Appendices

Appendix A:

According to Bird et al. (1960), the capillary diameter d can be represented by hydraulic diameter d_h (m) [91]. d_h can be defined as:

$$d_h = 4\frac{A}{C} \tag{A-1}$$

where, A is the cross-sectional area of the fluid flow (m²); C is the wetted perimeter of the cross-section (m). Moreover, Eq. (A-1) can be further expressed as:

$$d_h = 4\frac{A\tau L}{C\tau L} = 4\frac{A\tau L}{V_p}\frac{V_p}{C\tau L} = 4\frac{\phi}{S_v} \tag{A-2}$$

where, V_p is the volume of the porous medium (m³); ϕ is the porosity (dimensionless) and S_v is the specific surface area (m⁻¹), where the specific surface area is defined as the total surface area of the porous medium per unit bulk volume.

For the gob packing materials, according to the conceptual geometry of Figures 5-16 (a) and (b), the surface area of the transporting capillaries can be estimated as:

$$S_v = \frac{n4\pi D^2(1-\phi)}{n\frac{4}{3}\pi D^3} = \frac{3(1-\phi)}{D} \tag{A-3}$$

where, n is the numbers of rock-coal blocks (dimensionless) and D is the uniform radius of the rock-coal blocks (m).

From cross-sectional area A_1 to A_2, as shown in Figure 5-16(d), the area gradually expands. Here the cross-sectional areas A_1 and A_2 are the products of the void widths and void extension length in the negative x-direction. The corresponding coefficient induced by an increment of cross-sectional area can be expressed as [27,82]:

$$\xi_1 = (1 - \frac{A_1}{A_2})^2 \tag{A-4}$$

From cross-sectional area A_2 to A_3, as shown in Figure 4-16(d), the cross-sectional area gradually decreases. The definitions of cross-sectional areas A_2 and A_3 are the same as previous. The corresponding coefficient induced by the cross-sectional area decreasing can be expressed as [27,82]:

$$\xi_2 = 0.5(1 - \frac{A_3}{A_2}) \tag{A-5}$$

Based on the representative elementary volume (REV) - the dashed equilateral triangle in Figure 5-16(d) - the relationship between the size of the rock-coal block and porosity can be expressed as:

$$(1 - \phi)A_{REV} = \frac{1}{2}\pi D^2 \tag{A-6}$$

where, A_{REV} is the cross-sectional area (m²) of the REV. This may also be represented by $A_{REV} = \frac{\sqrt{3}}{4}(a + 2D)^2$ based on geometric relationships, where a is the void width (m), where inserting into Eq. (A-6) yields:

$$\alpha = \frac{a}{D} = 3^{-\frac{1}{4}}\sqrt{\frac{2\pi}{1-\phi}} - 2 \tag{A-7}$$

where, α is the ratio of void width to the radius of the rock-coal block (dimensionless).

In terms of the geometric relationship in Figure 4-16, the diameter of the cross-section A_2 can be expressed as:

$$b = \frac{\sqrt{3}}{2}a + (\sqrt{3} - 1)D \tag{A-8}$$

Substituting Eq. (A-7) and Eq. (A-8) into Eqs. (A-4) and (A-5) yields:

$$\xi_1 = (1 - \frac{a}{b})^2 = (1 - \frac{1}{\frac{\sqrt{3}}{2}+(\sqrt{3}-1)\frac{1}{\alpha}})^2 \tag{A-9}$$

$$\xi_2 = 0.5(1 - \frac{a}{b}) = 0.5(1 - \frac{1}{\frac{\sqrt{3}}{2}+(\sqrt{3}-1)\frac{1}{\alpha}}) \tag{A-10}$$

Appendix B:

The total gas content m in gob materials comprises states of free-phase gas and adsorbed gas [83,84]. The gas content is defined as:

$$m = \rho_g\phi + (1 - \phi)\rho_{ga}\rho_c V_g \tag{B-1}$$

where, ρ_{ga} is the gas density under standard conditions (kg/m³); ρ_c is the coal density (kg/m³); V_g is the average remaining gas content in the granular matrix at an equilibrium state (V_{gd}) with the gas pressure p recovered from the Langmuir equation [92]:

$$V_{gd} = \frac{V_L p}{p+p_L} \tag{B-2}$$

The methane density may be represented by the ideal gas law as:

$$\rho_g = \frac{pM}{RT} \tag{B-3}$$

where, M is the molecular weight of methane (kg/mol); R is the universal gas content (J/(mol·K)); and T is temperature (K).

11.0 Acknowledgement/Disclaimer